# A STUDY OF FRONTAL-SCALE AIR-SEA INTERACTION IN MIDLATITUDE WESTERN BOUNDARY CURRENT REGIMES

A Dissertation

by

XIAOHUI MA

Submitted to the Office of Graduate and Professional Studies of
Texas A&M University
in partial fulfillment of the requirements for the degree of

DOCTOR OF PHILOSOPHY

| | |
|---|---|
| Chair of Committee, | Ping Chang |
| Committee Members, | Xiaopei Lin |
| | R. Saravanan |
| | Robert D. Hetland |
| Head of Department, | Debbie Thomas |

August 2014

Major Subject: Oceanography

ABSTRACT

Frontal-scale air-sea interactions during boreal winter season in midlatitude western boundary current (WBC) regimes, including the Kuroshio Extension Region (KER) and Gulf Stream Region (GSR), are investigated using both observational (reanalysis) data and regional climate model simulations. The focus of the study is on the KER in the North Pacific.

Extreme flux events associated with cold air outbreaks (CAOs) in boreal winter in the KER of the Northwestern Pacific and the GSR of the Northwestern Atlantic are analyzed and compared based on different reanalysis datasets. A close relationship between extreme flux events over the KER/GSR and the Pacific Decadal Oscillation (PDO)/East Atlantic Pattern (EAP) is found with more frequent occurrence of extreme flux events during a positive PDO/EAP phase. Furthermore, the PDO/EAP may be explained as the rectified effects of the synoptic winter storms accompanied with the extreme flux events. A lag-composite analysis shows that event-day storms tend to have a preferred southeastward propagation path, potentially contributing to the southward shift of the storm track over the eastern North Pacific/Atlantic basin during positive PDO/EAP phase.

Using an atmosphere-only model (Weather Research Forecasting, WRF) at 27 km, two ensembles of simulations were conducted for boreal winter season in the North Pacific to study the possible local and remote influence of meso-scale oceanic eddies in the KER on the atmosphere. Filtering out meso-scale oceanic eddies results in a deep

tropospheric response along and downstream of the KER, including a significant decrease (increase) in winter season mean rainfall along the KER (west coast of US), a reduction of storm growth rate in the KER, and a southward shift of the jet stream and North Pacific storm track in the eastern North Pacific. A mechanism invoking moist baroclinic instability is proposed to link meso-scale oceanic eddies in the KER to large-scale atmospheric circulations and weather patterns in the North Pacific.

Using a high-resolution (9 km) coupled regional climate model (CRCM), three sets of experiment were performed to investigate potential feedbacks of ocean-eddy induced atmospheric response to the ocean. Filtering out meso-scale oceanic eddies during coupling causes a surface warming and a weak Kuroshio strength.

ACKNOWLEDGEMENTS

I would like to express my deepest appreciation to my advisor, Dr. Ping Chang, for his expert guidance, patience and encouragement throughout the course of my Ph.D. study. Without his persistent and illuminating instructions, this dissertation would not have been possible. His broad knowledge, perceptive insight into scientific research and responsible scientific attitude not only benefit my study here but also set up an excellent example for my future research.

I would also like to thank my committee members, Dr. Xiaopei Lin, Dr. R. Saravanan and Dr. Robert Hetland for their patience and encouragement in my research. Dr. Lin is always nice to give help and his scientific intellectual has been inspirational. Dr. Saravanan has provided instruction in conducting statistical analysis as well as plenty of helpful discussion. His provoking suggestions for my research are highly appreciated. I have also greatly benefitted from Dr. Hetland's classes, where I have gained fundamental understanding of ocean dynamics and turbulence.

I would like to thank my colleagues during my Ph.D study over the past few years. A special thank goes to Raffaele Montuoro who developed the coupled model. Without his efficient work, I would not have completed the numerical simulations used in this dissertation. I also want to thank Christina M. Patricola who gave me detailed and patient instructions on running the WRF model and helped review my dissertation. My grateful thanks is also extended to Mingkui Li, Xiaolin Yu and Zhao Xu for their technical support. Mingkui Li walked me through the coupled model and Xiaolin Yu

taught me how to run the ROMS model at the beginning of my study, which has benefited my following work. Zhao Xu gave me many good suggestions during my graduate study and helped to improve my coding skills. Thanks also go to Jenshan Hsieh and Zhao Jin who gave me good advice in atmosphere baroclinity and mathematics. I also want to thank Jaison Kurian who provided me the new vertical coordinate for ROMS model.

I would like to extend my thanks to other colleagues in my research group, my friends and the faculty in the Department of Oceanography for their aids during my graduate study. I want to thank Kelly Cole who helped to revise the words and phrases in this dissertation.

I am grateful to China Scholarship Council for their financial support. I am also grateful to the Texas A&M Supercomputing Facility and the Texas Advanced Computing Center (TACC) at The University of Texas at Austin, which provided the computing resources used in this dissertation.

Finally, I would like to express my heatfelt gratitude to my parents for their solid support and unconditional love, and particular thanks to my boyfriend, Shenghui Zhou, for his understanding and continuous encouragement, which gives me strength and confidence to complete my study.

# NOMENCLATURE

| | |
|---|---|
| 20CRV2 | NOAA 20th Century Reanalysis Version 2 |
| ACC | Antarctic Circumpolar Current |
| AEY | Active Eddy Years |
| AGCM(s) | Atmosphere General Circulation Model(s) |
| CAO(s) | Cold Air Outbreak(s) |
| CCMP | Cross-Calibrated Multi-Platform |
| CLIVAR | Climate Variability and Predictability |
| COREII | Coordinated Ocean-ice Reference Experiments II |
| CPL-MEFS | Coupled Meso-scale Eddy Filtered Simulation |
| CRCM | Coupled Regional Climate Model |
| CTRL | Control |
| EAP | East Atlantic Pattern |
| ECMWF | European Centre for Medium-Range Weather Forecasts |
| EOF | Empirical Orthorgonal Function |
| GCM(s) | General Circulation Model(s) |
| GFDL | Geophysical Fluid Dynamics Laboratory |
| GHGs | Greenhouse Gases |
| GIN | Greenland-Iceland-Norwegian |
| GS(R) | Gulf Stream (Region) |
| IEY | Inactive Eddy Years |

| | |
|---|---|
| IPCC | Intergovernmental Panel on Climate Change |
| KE(R) | Kuroshio Extension (Region) |
| KF | Kain-Fritsch |
| KPP | K-profile Parameterization |
| LHF | Latent Heat Flux |
| MEFS | Mesoscale-Eddy-Filtered Simulation |
| MLD | Mixed Layer Depth |
| MW-IR | Mircrowave InfraRed Optimal Interpolated |
| NAO | North Atlantic Oscillation |
| NCEP2 | NCEP-DOE Reanalysis 2 |
| NCEP-CFSR | National Centers for Environmental Prediction-Climate Forecast System Reanalysis |
| NCEP-NCAR | National Centers for Environmental Prediction and National Center for Atmospheric Research |
| NDJFM | Nov-Dec-Jan-Feb-Mar |
| NPO | North Pacific Oscillation |
| OAflux | Objectively Analyzed air-sea Fluxes |
| OGCM(s) | Ocean General Circulation Model(s) |
| ONDJFM | Oct-Nov-Dec-Jan-Feb-Mar |
| PBL(H) | Planetary Boundary Layer (Height) |
| PC(s) | Principle Component(s) |
| PDF | Probability Density Function |

| | |
|---|---|
| PDO | Pacific Decadal Oscillation |
| PNA | Pacific North American |
| PV | Potential Vorticity |
| Qv | Water Vapor Mixing Ratio |
| ROMS | Regional Ocean Modeling Systems |
| RSS | Remote Sensing System |
| SHF | Sensible Heat Flux |
| SLP | Sea Level Pressure |
| SODA | Simple Ocean Data Assimilation |
| SSH | Sea Surface Height |
| SST | Sea Surface Temperature |
| STMW | Subtropical Mode Water |
| SVD | Singular Value Decomposition |
| THF | Turbulent Heat Fluxes |
| TRMM | Tropical Rainfall Measuring Mission |
| U300 | U Wind at 300 hpa |
| U850 | U Wind at 850 hpa |
| UNCPL-MEFS | Uncoupled Meso-scale Eddy Filtered Simulation |
| USWC | U. S. West Coast |
| WBC(s) | Western Boundary Current(s) |
| WRF | Weather Research Forecasting |

TABLE OF CONTENTS

Page

LIST OF FIGURES

Page

# CHAPTER I

# INTRODUCTION

## 1.1 Background

### *1.1.1 Introduction of Frontal-Scale Air-Sea Interactions in Western Boundary Current Regimes*

The Kuroshio Extension Region (KER) in the Northwestern Pacific and Gulf Stream Region (GSR) in the Northwestern Atlantic are regions where the most intense extratropical air-sea interaction takes place, which may play an important role in extratropical climate variability (Fankignoul 1985; Hoskins and Hodges 2002; Joyce et al. 2009; Kelly et al. 2010; Kwon et al. 2010). The Kuroshio and Gulf Stream, known as the strongest western boundary currents in midlatitudes, carry vast amount of heat and moisture from the tropics to extratropics, forming strong sea surface temperature (SST) fronts along their paths. When they encounter the cold and dry continental airmass brought by the strong midlatitude westerlies and storms, intense sensible and latent heat fluxes are released from the oceans to the atmosphere in these regions (Kelly and Dong 2004; Kelly et al. 2010). Understanding of the strong frontal-scale air-sea interaction in the western boundary current (WBC) regions is crucial to the understanding and predication of climate variability in the midlatitudes (Kushinir et al. 2002).

Earlier studies on extratropical air-sea interactions focused on local oceanic response to surface atmospheric forcing at short-time scales (Nanimas 1959, 1972; Davis 1976; Fankignoul 1985; Seager et al. 2000). It has been commonly recognized that SST

anomalies can be generated thermodynamically by surface turbulent heat flux (THF) anomalies due to changes in air temperature, humidity and wind speed, or dynamically by surface Ekman currents induced by wind stress curl anomalies. A remote forcing effect of large-scale atmosphere circulation on long-time scale SST variations was first proposed by Bjerknes (1964) and later confirmed by many follow-up studies (Deser and Blackmon 1993; Latif and Barnett 1994; Zhang et al. 1997; Miller and Schneider 2000; Seager et al. 2001). SST anomalies in the WBC regions can be related to the remote change in basin-scale wind stress curls through modification of subtropical gyre circulations or long Rossby wave propagations (Qiu and Chen 2005).

A more important aspect of understanding extratropical air-sea interactions is how the ocean feeds back onto the atmosphere. It has been demonstrated that the atmosphere does respond to midlatitude SST anomalies (Kushnir et al. 2002). However, how strong the response is compared to atmospheric internal variability and whether the response can constitute an active coupling between the atmosphere and ocean are still under debate. Some studies suggest that SST may play an active role in determining air-sea coupling in midlatitudes (Latif and Barnett 1994; Miller and Schneider 2000; Nakamura et al. 2004, 2008; Taguchi et al. 2009, 2013). Others viewed that the influence of SST on the atmosphere is weak compared to atmospheric internal variability (Saravanan 1998; Saravanan et al. 2000) and the coupling between the two mediums is passive (Barsugli and Battisti 1998). Two mechanisms governing atmospheric response to midlatitude SST anomalies were summarized in a review paper by Kushinir et al. (2002). The first is a linear mechanism, in which atmospheric surface THF forces a change in SST and then

experiences a reduced thermal-damping effect due to the SST adjustment (Barsugli and Battisti 1998). The second one is a nonlinear eddy-mediated mechanism, in which SST anomalies across a WBC front affect low-level baroclinicity that in turn modulates storm track activity by altering the efficiency of energy conversion from the mean flow (Nakamura et al., 2004). However, the nonlinear eddy-mediated mechanism does not take into consideration of moisture effects.

Many of recent studies based on observations and Atmosphere General Circulation Models (AGCMs) in WBC regions tend to support the second mechanism and stress the importance of midlatitude storm tracks in affecting extratropical air-sea interactions (Nakamura et al. 2008; Taguchi et al. 2009; Booth et al. 2010; Shaman et al. 2010). A deep and unstable planetary boundary layer (PBL) develops over warm SST, which enhances the vertical momentum transfer and air-sea heat flux exchange, creating favorable conditions for storm track development (Booth et al. 2010). Using an atmosphere-only model forced by a prescribed SST with a sharp meridional gradient versus by a smoothed SST with weak gradient in the KER, Taguchi et al. (2009) showed a reduced storm track activity corresponding to the smoothed SST forcing due to the decreased meridional gradient of THF and moisture across the oceanic front. A recent study by Shaman et al. (2010) suggested that extreme wintertime THF produced by episodic cold air outbreaks is crucial to air-sea interactions along the GSR. All these recent studies suggest a tangible relationship between midlatitude storm tracks and oceanic fronts in WBC regions.

*1.1.2 Midlatitude Storm Track Dynamics*

The important role that midlatitude storm tracks play in air-sea interactions in WBC regions motivates a necessity to better understand midlatitude storm track dynamics. Storm tracks are usually defined by band-pass filtered variance statistics where synoptic-scale atmospheric variability is strongest (Chang 2009). From observations, it is clear that northern hemisphere storm tracks form along the Kurohiso and Gulf Stream extensions (Chang et al. 2002), suggesting a potential influence of underlying oceanic fronts. Individual synoptic storms are often intensified when they pass over the WBC regions with enhanced heat and moisture supply from the warm ocean (Nakumura et al. 2004, 2008; Kelly et al. 2010). The genesis of midlatitude storm tracks is governed by baroclinic instability of the atmosphere (Charney 1947; Eady 1949; Hoskins et al. 1985). The sharp temperature gradient in the WBC regimes leads to a strong vertical wind shear governed by the thermal wind relation and an unstable boundary layer, allowing wave transients to extract energy from the mean flow and sustaining storm growth. More discussions about the baroclinic instability theory will be given in Chapter III. The sharp SST gradient across the fronts in the WBC regions enhances the near surface baroclinicity, favoring the development of storm tracks (Nakamura et al. 2004). Brayshaw et al. (2008) showed that an intensified midlatitude SST gradient can give rise to a stronger and a poleward shift of midlatitude storm tracks in an idealized AGCM simulation. Suppresion of SST gradient in frontal regions can lead to an equatorward shift of the entire low-level atmospheric circulation system, including the surface westerlies, jet streams and subtropical high-pressure belt (Sampe et al. 2010). These

studies point to the importance of oceanic fronts in WBC regions in anchoring midlatitude storm tracks.

Midlatitude storm tracks transport heat poleward, so that they tend to reduce the sharp meridional temperature gradient across the oceanic fronts and near-surface baroclinicity (Hoskins and Hodges 2002; Nakamura et al. 2008). In order to sustain the continuous development of synoptic storms, the baroclinic instability must be restored. A self-maintenance mechanism of storm track was proposed by Hoskins and Valdes (1990), who argued that the intensified latent heat release accompanying midlatitude storms increases the surface baroclinic instability and is able to fuel further development of cyclones. Enhanced storm activity will cause enhanced surface westerlies through eddy-mean flow interactions, which in turn drive strong WBCs, maintains the sharp SST gradient, and anchors storm tracks along the fronts. Another "oceanic baroclinic adjustment" mechanism later hypothesized by Nakamura et al. (2008) suggested that warm ocean water over the southern side of WBCs produces upward heat flux and heats the overlying atmosphere while on the northern side, the atmosphere is cooled through downward heat flux. The air temperature gradient can then be restored within 2-3 days, which is necessary for the recurrent of storm development. These previous studies indicate that in the frontal regions, not only the sharp SST fronts and intensive moisture supply are important for the genesis of storm tracks, but also the warm WBCs play a crucial role in maintaining the sharp SST gradient and restoring the baroclinic instability, contributing to the anchoring of midlatitude storm tracks.

*1.1.3 Relationship Between Storm Track and Large-scale Atmosphere Circulation*

Another key question in understanding extratropcial air-sea interactions is to determine the extent to which oceanic fronts can have an influence on large-scale atmospheric circulation. It has been shown that midlatitude storm tracks intensify when they pass over the underlying oceanic fronts. Changes in storm tracks in the WBC regions will lead to changes of mean flow and storm tracks further downstream, linking the frontal-scale air-sea interaction in the WBC regions to basin scale atmospheric variability.

The leading mode of North Pacific and North Atlantic climate variability are the Pacific Decadal Oscillation (PDO) and the North Atlantic Oscillation (NAO), respectively (Mantua et al. 1997; Hurrell 1997). Similarly as discussed above, the decadal climate variability in the atmosphere can lead to local SST change through changes of surface THF and wind stress curl (e.g., Davis 1978) or remote SST anomalies in the WBC regions through westward propagation of Rossby waves (e.g., Latif and Barnett 1994). In particular, a meridional shift of WBCs, i.e. the Kuroshio Extension (KE) and Gulf Stream (GS), can be induced by displacement of basin scale ocean gyre circulation associated with atmospheric decadal climate variability (Joyce et al. 2000; Seager et al. 2001; Nakamura and Kazmin 2003). The Kuroshio path alternates between unstable (large meander) and stable (small meander) state and is explained as a delayed oceanic response to PDO forcing in the eastern North Pacific basin (Qiu and Chen 2005).

Understanding whether the decadal SST anomalies can extend their impact beyond the PBL so as to affect the large-scale atmospheric circulation is crucial to determine the predictability of long term climate variability in the North Pacific and North Atlantic (Kushnir et al. 2002; Frankignoul and Sennechael 2007). The linkage between SST anomalies in the WBC regions and large-scale air-sea interaction can be built through midlatitude storm tracks. SST anomalies in the WBC regions may cause changes in atmospheric temperature, precipitation, and THF, which may further modify low-level baroclinic instability, which generates changes in storm activity and affects modes of large-scale climate variability (Rodwell et al. 1999). Shifts of the KE and GS at interannual and decadal time scales may produce a meridional shift in local storm track position or even a non-local downstream response (Joyce et al. 2009). Frankignoul et al. (2011) reported a large-scale atmospheric circulation response that resembles the North Pacific Oscillation (NPO) pattern to a meridional shift of the KE. If these findings are robust, they suggest that the influence of SST changes along WBC fronts on winter storms may not be limited to surface boundary layer, but extend to the troposphere, which may contribute to large-scale decadal climate variability.

Extensive research has been carried out to explore the relationship between midlatitude storm tracks and low frequency modes of climate variability in both the North Pacific and Atlantic (Zhang et al. 1997; Thompson and Wallace 1998; Pinto et al. 2011). Changes in storm intensity and storm track position were reported during a particular PDO/NAO phase or during other modes of climate variability in the North Pacific and Atlantic (Nakamura et al. 1997; Chang and Fu 2002; Lee et al. 2012). The

relationship between storm track variability and low frequency modes of climate variability is also attributed to a rectified effect of synoptic scale storms (Feldstein 2003; Benedict 2004; Rivere and Orlanski 2007). In this dynamic framework, the evolution of the Pacific North American (PNA) in the North Pacific and the NAO in the North Atlantic are viewed primarily as a stochastic synoptic process with a time-scale about one week (Feldstein 2000). This view was further supported by Vallis et al. (2004) who argued that the NAO and annular mode in the Atlantic sector can be reproduced when a simple dynamic model is stirred by baroclinic eddies. The stochastic stirring can lead to changes of zonal flow through eddy momentum flux convergence. Recent studies further relate large-scale modes of climate variability to synoptic wave breaking and suggest that positive phase of NAO is dominated by anti-cyclonic wave breaking and vice versa (Benedict et al. 2004; Riviere and Orlanski 2007). These previous studies stress the importance of synoptic storms in determining large-scale low frequency modes of climate variability in the extratropics.

*1.1.4 Future Changes in Storm Track Under Global Warming*

Stuides have shown that midlatitude storm tracks can play an important role in frontal-scale air-sea interactions and in transporting eddy momentum and heat, affecting low-frequency modes of climate variability. How storm tracks will response to future climate change under global warming is a subject that has received recent attention (Yin 2005; Woollings et al. 2012). Climate model simulations of future climate forced by greenhouse gases (GHGs) indicate that the statistics of synoptic storms will be modified with fewer and more intensified cyclones occurring under global warming (McCabe et

al. 2001; Lambert 1995). A poleward and upward shift of storm tracks is expected due to changes in upper tropospheric baroclinic instability in response to global warming, which is accompanied by a large-scale atmospheric circulation response, including a poleward shift of surface wind stress curl, the low pressure center in high latitude as well as increased rainfall in the midlatitudes (Yin 2005). The change in upper level baroclinic instability in boreal winter in the midlatitudes is mainly associated with increased temperature gradient caused by enhanced warming in the tropics (Geng and Sugi 2003; Yin 2005; O'Gorman et al. 2010). An increased tropopause height and poleward shifted jet streams are demonstrated to be consistent with the intensified and poleward shifted storm tracks (Lorenz and DeWeaver 2007). A recent study by Riviere (2011) gave a plausible dynamical explanation of the poleward shift of the midlatitude jet streams. The enhanced upper-level baroclinic instability under global warming tends to favor longer wavelength, unstable synoptic storms that break anti-cyclonically and push the jet stream poleward through increased eddy momentum flux convergence. Although these recent studies point to a close relationship between changes in storm tracks and midlatitude jet streams under global warming, more research is needed to understand the underlying dynamics and causality between synoptic eddies and mean flow changes.

**1.2 Motivations and Objectives**

Advancing our understanding of tropical air-sea interactions with successful application to climate prediction inspires our interest in exploring extratropical air-sea interactions (Kushinir et al. 2002). Our present understanding of extratropical air-sea interaction in western boundary current (WBC) systems still remains limited and

advancing this understanding has proven to be challenging for several reasons. First, as sharp thermal fronts form along narrow WBC regions, high-resolution models are required to resolve the frontal structure (Bryan et al. 2010; Kelly et al. 2010; Kwon et al. 2010). Additionally, WBC systems are highly nonlinear and contain strong meso-scale ocean eddy activities, which makes the interaction between the ocean and atmosphere highly complex (Chelton et al. 2004; Small et al. 2008). This dissertation aims to improve our understanding of frontal-scale air-sea interactions in WBC regions by combining observational analyses with high-resolution regional climate model simulations. The KER and GSR share many similarities in how frontal-scale air-sea interactions are shaped, and the main focus of this dissertation will be on the KER in the North Pacific. As previous studies indicate, midlatitude storm tracks have a significant influence on frontal-scale air-sea interactions in WBC regimes. Since storm tracks are most intense during winter season, most analyses and modeling experiments will be conducted in boreal winter season.

As discussed above, frontal-scale air-sea interactions in the WBC regions may be vital in large-scale low frequency modes of climate variability in the extratropics (Latif and Barnett 1994; Rodwell et al. 1999; Feldstein 2000, 2003). However, whether the decadal climate variability is governed by low frequency oceanic forcing or mostly determined by stochastic synoptic-scale storm variability through rectification is still under debate. To advance our understanding on this problem, in Chapter II, we explore extreme flux events occurring over the KER and GSR in association with Cold Air

Outbreaks (CAOs) and their relationship with storm tracks and modes of climate variability in North Pacific and Atlantic by analyzing reanalysis data.

Understanding how the atmosphere responds to SST anomalies in the WBC regions is crucial to the understanding of the frontal-scale air-sea interaction in these regions (Kushnir et al. 2002). The sharp SST gradient across the fronts favors the development of storm tracks by increasing baroclinic instability (Nakamura et al. 2004, 2008; Brayshaw et al. 2008; Taguchi et al. 2009). Recent studies based on high-resolution satellite observations reveal potential influence of meso-scale oceanic eddies in WBC regions on the atmosphere (Chetlon et al. 2004; Small et al. 2008). In chapter III, using a high-resolution atmosphere-only model, we will investigate how meso-scale oceanic eddies in the KER affect the midlatitude storm track and large-scale atmosphere circulation in the North Pacific.

Another important aspect of midlatitude frontal-scale air-sea interactions is the feedback of ocean-eddy driven atmospheric response onto the ocean. Meso-scale oceanic eddies may affect atmospheric boundary, diabatic heating and storm tracks. These changes in the atmosphere will in turn modify underlying SST by altering the THF and surface winds at both the large-scales and frontal-scales (e.g., Frankignoul 1985; Chelton et al. 2004). Fully coupled models are required to represent the two-way air-sea interaction in the WBC regions. In Chapter IV, a high-resolution coupled regional climate model that resolves both meso-scale oceanic eddies and synoptic-scale storms will be applied to the North Pacific, focusing on the atmospheric feedback onto the

ocean, so that a holistic understanding of frontal-scale air interactions in the KER can be gained. Conclusions and future work are discussed in Chapter V.

# CHAPTER II

# WINTER EXTREME FLUX EVENTS IN THE WESTERN BOUNDARY CURRENT REGIMES AND RELATIONSHIP WITH MODES OF CLIMATE VARIABILITY

## 2.1 Introduction

Modes of climate variability in the North Pacific and North Atlantic have been well documented and widely discussed in a large body of literatures (e.g., Hurrell 1997; Mantua et al. 1997; Nakamura et al. 1997; Hurrell et al. 2003; Minobe et al. 2004). The most dominant patterns of North Pacific and Atlantic climate variability are the Pacific Decadal Oscillation (PDO) and the North Atlantic Oscillation (NAO), while the importance of other patterns, such as the North Pacific Oscillation (NPO) and the East Atlantic Pattern (EAP), has also been recognized (Rogers 1981, Barnston and Livezey 1987, Linkin and Nigam 2008). These extratropical modes of variability are manifested in changes in large-scale atmospheric pressure, temperature and precipitation patterns (Cayan and Peterson 1989; Trenberth and Hurrell 1994; Rogers 1997; Marshall et al. 2001; Miller et al. 2004; Hurrell and Deser 2009). They have also been linked to changes in storm track activities and atmospheric blocking activities in the North Pacific and Atlantic sectors (e.g., Nakamura 1996; Woollings et al. 2008; Chang 2009; Tauguchi et al. 2012; Maidens et al. 2013). The large-scale atmosphere circulation changes associated with these modes can not only affect local ocean conditions via changes in surface heat fluxes and Ekman advection (Davis 1978; Barnett 1981; Alexander 1992a, b), but also produce remote changes in SST along the western boundary currents through

westward propagation of wind-induced long Rossby waves (Latif and Barnett 1994; Miller and Schneider 2000; Seager et al. 2001; Qiu and Chen 2005). Understanding of these extratropical modes of climate variability has important implications for the understanding of climate predictability in the North Pacific and North Atlantic, which is a key objective of the international Climate Variability and Predictability (CLIVAR) program.

Dynamical mechanisms governing decadal variability of midlatitude climate system is still not fully understood. Earlier studies suggest that decadal and longer time-scale SST variability can simply arise from a red noise ocean mixed-layer response to white noise atmospheric forcing (Hasselmann 1976; Frankignoul and Hasselmann 1977). Ample evidence has been presented that midlatitude SST anomalies are generated by anomalous surface heat flux and Ekman convergence/divergence related to anomalous wind conditions (Namias 1959, 1972; Bjerknes 1964; Davis 1976; Frankignoul 1985). Observational analyses show that SST anomalies typically lags surface heat flux anomalies by 1-3 months (Cayan 1992; Deser and Timlin 1997; Frankignoul et al. 1998), supporting the atmosphere-forcing-ocean paradigm.

The extent to which midlatitude SST anomalies can feedback onto the atmosphere has been intensely debated in the literature and still remains controversial. Latif and Barnett (1994,1996) proposed, based on simulations of a coupled GCM, that the Aleution Low system in the North Pacific is responsive to large-scale SST anomalies induced by changes in the subtropical gyre ocean circulation and the resultant change in surface heat fluxes act to amplify the SST anomalies, forming an active ocean-

atmosphere coupling mechanism. The active ocean-atmosphere coupling together with a delayed negative feedback due to oceanic adjustment to changes in wind stress curl through westward propagating long Rossby waves gives rise to a decadal oscillation which is responsible for the PDO. A subsequent modeling study by Robertson (1996) using a different coupled GCM supports this active ocean-atmosphere coupling paradigm. Zorita and Frankignoul (1997) examined a similar mechanism in the North Atlantic in a coupled ocean–atmosphere general circulation model. Reviews of the active ocean-atmosphere coupling mechanism can be found in Latif (1998) and Miller and Schneider (2000).

Other studies challenging this paradigm argue that the atmospheric response to midlatitude SST anomalies is very weak compared to variability generated by its internal dynamics. For example, Saravanan (1998) estimated, based on simulations of an AGCM, that the SST-forced geopotential height variability at 500 mb in the North Pacific and Atlantic is less than 15% of that induced by atmospheric internal dynamics. The weak atmospheric response to midlatitude SST may hamper the possibility of active atmosphere-ocean coupling. A review of studies on atmospheric response to midlatitude SST anomalies can be found in Kushnir et al. (2002). According to Kushinir et al. (2002), the weak SST-forced atmospheric variability can be achieved through two mechanisms: 1) a linear mechanism where thermodynamic feedbacks between surface heat fluxes and ocean mixed layer temperature act to reduce thermal damping, enhancing low-frequency variability of the atmosphere and 2) a nonlinear mechanism where an eddy mediated process links SST forcing to storm track activity. The former can be

considered as a passive coupling between the atmosphere and ocean and can be understood as an extension of Hasselmann climate model (Hasselmann 1976) in the framework of a coupled atmospheric energy balance model and a slab ocean mixed layer model, as elegantly demonstrated by Barsugli and Battisti (1998). The latter involves complex interactions between atmospheric storm tracks and SST fronts along intense ocean western boundary currents (WBCs) (Nakamura et al. 2004, 2008), which are less understood.

Most of recent studies on midlatitude atmosphere-ocean interactions focus on the latter mechanism. Special attention has been paid to the KER in the North Pacific and the GSR in the North Atlantic. These strong WBCs are known to carry vast amount of oceanic heat poleward from the tropics and release it to the atmosphere through THF, destabilizing the atmosphere and favoring the development of storm tracks (Nakamura et al. 2004, 2008; Nakamura and Yamane 2009, 2010; Kwon et al. 2010; Kelly et al. 2011). Nakamura (2004) argued that the sharp SST gradients along the Kuroshio and Gulf Stream front play a fundamental role in anchoring the North Pacific and North Atlantic storm tracks through their influence on the low-level baroclinicity of the atmosphere. In a suite of AGCM simulations, Taguchi et al. (2009) demonstrated that a smoothed SST gradient in the KER leads to a weak storm activity. Evidence of atmosphere-ocean coupling along the Kuroshio and Gulf Stream has also been presented using high-resolution satellite data (e.g., Chelton et al. 2001, 2004; Sampe and Xie 2007). By spatially filtering satellite measured wind speed and SST, a remarkable positive correlation between the small-scale wind speed and the underlying oceanic meso-scale

eddies in eddy-rich regions, such as the KER and GSR, has been revealed (Maloney and Chelton 2006; Chelton et al. 2010; O'Neil et al. 2012), suggesting an influence of SST on the overlying atmosphere in these eddy-rich regions. Small et al. (2008) reviewed the existing observational evidence of atmosphere-ocean coupling along with model simulations of atmosphere-ocean interactions in the KER and GSR. A recent high-resolution coupled GCM study by Bryan et al. (2010) show that resolving meso-scale oceanic eddies is critically important to realistically simulate the observed atmosphere-ocean coupling in the eddy-rich regions. A more recent coupled model study of atmospheric response to decadal SST anomalies in the North Pacific by Taguchi et al. (2012) further suggests that the PDO may also be influenced by SST anomalies along the subarctic frontal zone. Collectively, these recent studies point to the potentially important role of meso-and frontal-scale atmosphere-ocean interactions along the Kuroshio and Gulf Stream in large-scale climate variability in the North Pacific and Atlantic. Yet, dynamic linkages between them are still poorly understood.

A key process in meso-and frontal-scale atmosphere-ocean interactions along the Kuroshio and Gulf Stream is surface latent and sensible heat fluxes; together they determine total turbulent heat exchanges between the atmosphere and ocean. It is well known that synoptic storm systems can be vital in regulating surface latent and sensible heat fluxes in these regions (Hoskins and Valdes 1990; Tauguchi et al 2009; Kwon and Joyce 2013). Shaman et al. (2010; hereafter referred as SH10) recently showed, based on 60 years of NCEP-NCAR (National Centers for Environmental Prediction and National Center for Atmospheric Research) reanalysis data, that in the GSR a major proportion of

wintertime surface THF is attributed to a relative small number of high flux events associated with extreme synoptic storms. An earlier study of a 17-year daily surface heat flux record from an AGCM simulation revealed that in winter season surface heat flux variability on timescales less than 30 days can explain more than half of the total intra-seasonal heat flux variance in both the North Pacific and Atlantic Ocean (Alexander and Scott, 1997). Alexander and Scott (1997) further showed that within the 30-day frequency band, the 3-10 day synoptic variability associated with mid-latitude storm track activity makes the most important contribution to the intra-seasonal heat flux variance and the synoptic band THF variability appears to coincide with the low-level atmospheric circulation, suggesting a linkage between storm activity and large-scale atmospheric circulation variability. Walsh et al. (2001) showed that enhanced Cold Air Outbreak (CAO) activity in the North Atlantic appears to be associated with negative phases of the NAO.

Motivated by these previous studies, we attempt to advance our understanding of meso-and frontal-scale atmosphere-ocean interactions in the KER and GSR and their role in climate variability by focusing on two aspects. First, we will extend the extreme flux event analysis presented by SH10 to the KER and compared the results in the KER to those of SH10 in the GSR. Given that both these regions are considered to be the most intensive air-sea interaction regions in the extratropics (Kelly et al. 2010), it is of great interest to contrast differences and similarities between extreme flux events in these regions and their respective role in large-scale climate variability in the North Pacific and Atlantic sector. Second, we will investigate the relationship among variability of

extreme flux events in the KER and GSR, North Pacific and Atlantic storm tracks and modes of climate variability in North Pacific and Atlantic sector. Furthermore, we will examine the relationship between the extreme flux variability and SST variability in North Pacific and Atlantic.

The Chapter is organized as follows. Section 2 introduces the data sets, the criteria to define extreme flux events and the methodologies used to perform the analysis. Section 3 illustrates the general characteristics of extreme flux events in the KER and GSR and contrasts their similarities and differences in the two regions. Section 4 examines the relationship among KER and GSR extreme flux variability, North Pacific and Atlantic storm tracks and modes of climate variability in North Pacific and Atlantic sector. Section 5 discusses the relationship between extreme flux variability and SST variability in the KER and GSR. Finally, section 6 summarizes and discusses the major findings of the study.

**2.2 Data and Analysis Method**

The study of surface turbulence heat flux variability in the WBC regions and its relation with midlatitude storms requires high-resolution data both temporally and spatially. The datasets we used are 6 hourly NCEP-CFSR (the National Centers for Environmental Prediction-Climate Forecast System Reanalysis, 1979-2009) (Saha et al. 2010), NCEP-NCAR Reanalysis (1948-2009) (Kalnay et al. 1996), NOAA 20th Century Reanalysis Version 2 (1870-2009, hereafter referred as 20CRV2) (Compo et al. 2011), as well as the daily OAflux (Objectively Analyzed air-sea Fluxes, 1985-2009) data set (Yu et al. 2008). The NCEP-CFSR is based on a high-resolution, fully coupled

atmosphere-ocean-land-sea ice model data assimilation. The horizontal resolution for atmospheric variables is T382 grid (approximately 0.3°). There are 37 vertical pressure levels from the surface to 100pa in the atmosphere (Saha et al. 2010). The NCEP-NCAR is an assimilation data product based on an atmospheric general circulation model on a T62 atmospheric grid (approximate 2°) and 17 vertical levels (Kalnay et al. 1996). The 20CRV2 has similar horizontal resolution to NCEP-NCAR, but assimilates only the observed surface pressure (Compo et al. 2011). The data set goes back to 1870, but we only use the data from 1910 to 2009. Combing various sources of observations and calculating through bulk formula (Fairall et al. 2003), OAflux gives an optimal estimation of observationally derived surface THF (Yu et al. 2008). Throughout this study, we applied similar analyses to all these datasets to examine and compare the variability of extreme flux events in the KER and GSR, but the primary data set used in this study is the NCEP-NCAR reanalysis, because many previous studies have shown that NCEP-NCAR captures realistic storm variability and correct index of the extreme flux events through validation of the reanalysis against direct observations (Harnik and Chang 2003; Qiu et al. 2004; Bond and Cronin 2008).

We focus on the examination of boreal winter season (NDJFM) extreme flux events in the KER and GSR. The analysis domains are so chosen that they cover the largest winter mean surface latent and sensible heat fluxes, i.e., 10° latitude by 30° longitude boxes in the KER and GSR as defined in Figure 1. We note the latter is different from the so-called "CLIMODE region" described in SH10. We chose these regions, because they are aligned more closely with the most significant THF variability, and thus likely

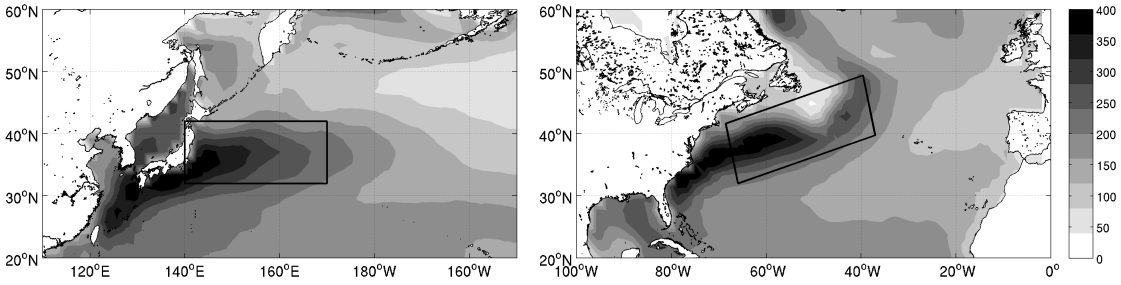


Figure 1. Climatological winter season (NDJFM) mean THF in the KER (left) and GSR (right) based on 61-year NCEP-NCAR reanalysis ($W/m^2$). Area used to define extreme flux events in the KER and GSR are out lined by the black boxes.

include all extreme flux events in the North Pacific and Atlantic. In SH10, extreme flux events are defined by area averaged daily SHF/LHF which exceeds 80 percentile value (a chosen threshold) of the entire winter SHF/LHF variability. The days when extreme flux events occur are defined as event days. Non-event days are the rest of the winter days when SHF/LHF is below the threshold. They also showed that the basic results of the study are not sensitive to the chosen threshold. Our own analysis confirms this finding and shows that the results in both the KER and GSR are not particularly sensitive to either the choice of the analysis regions or the threshold value. Therefore, following SH10, we chose 80 percentile as a threshold (hereafter referred as HF80) to define extreme flux events in the KER and GSR for all the datasets used in this study. Specifically, the number of event days in each winter season is obtained by counting all the days when the area-averaged daily THF exceeds HF80. The percentage contribution to the total THF from extreme flux events is calculated by integrating the THF on event days divided by the total THF accumulated in all winter days. The duration of each extreme flux event is defined as the number of continuous days when the THF is above

HF80. Figure 2 illustrates the selection criterion for the extreme events and compares their statistical properties in the KER and GSR, which will be further discussed in the next section.

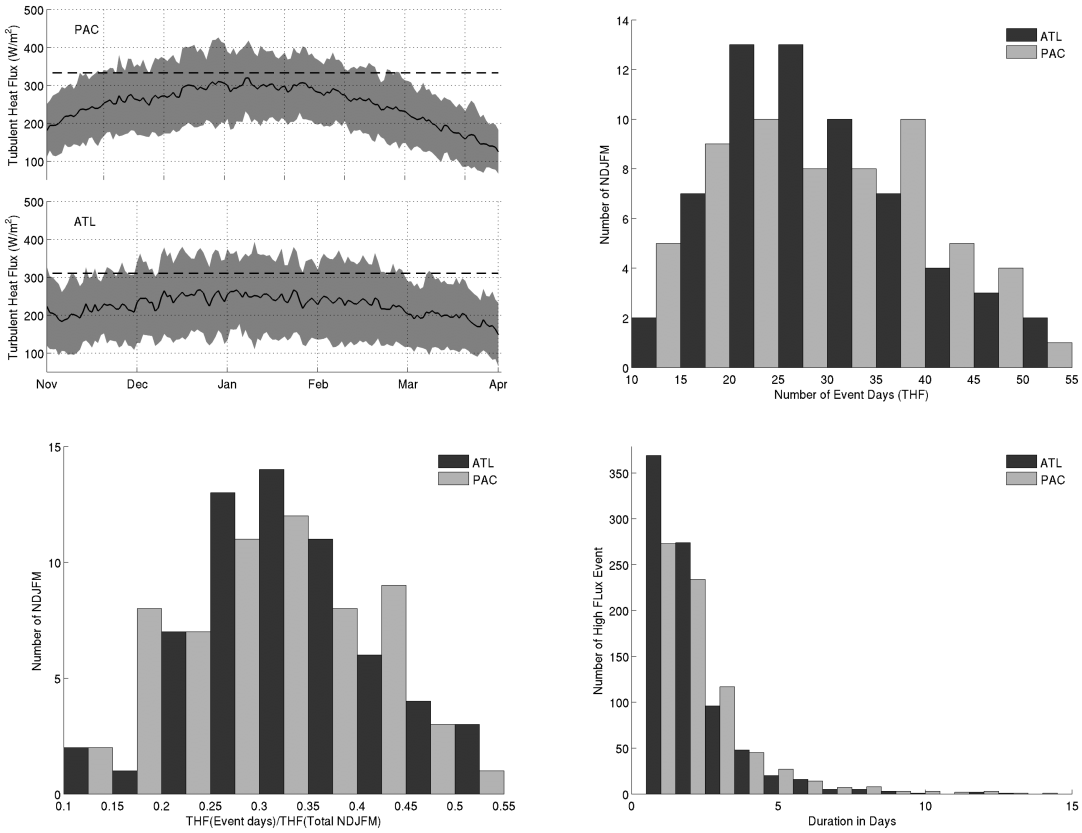


Figure 2. Upper left, 61-year winter season (NDJFM) NCEP-NCAR daily THF (black solid), the standard deviation (gray shaded) and the HF80 critical value chosen to define extreme flux events (black dashed). Top the KER, bottom the GSR. Upper right, histogram (in numbers of winters) of number of event days in each winter during 1948-2009. Bottom left, histogram (in numbers of winters) of fraction of event-day THF contribution to the total THF in each winter. Bottom right, histogram (in number of extreme flux events) of extreme flux event durations in days. In all the histogram plots, black is for the GSR in the Atlantic and gray is for the KER in the Pacific.

To identify storms responsible for the extreme flux events, we first applied a 1-8 day band-pass filter to the 6 hourly reanalysis data, so that synoptic-scale storm activities are isolated from large-scale, low frequency atmospheric variability. We then divide the band-pass filtered data into two groups according to event days and non-event days selected using the HF80 threshold. Finally, the event-day and nonevent-day data are averaged, respectively, to form a composite for each group, which will be discussed in the following section.

Finally, to explore relationships between extreme fluxes and modes of large-scale atmospheric variability, we performed empirical orthorgonal function (EOF) analysis and Singular Value Decomposition (SVD) analysis on various relevant variables. SVD analysis is effective in identifying co-varying oceanic and atmospheric patterns (Bretherton et al. 1992). Additionally, we carried out lag-regression analyses to examine relationships between SST and extreme fluxes. These analyses are based on seasonal mean anomalies and the results will be discussed in section 4 and section 5.

### 2.3. Event-Day and Nonevent-Day Fluxes and the Associated Storms

#### *2.3.1 Characteristics of Extreme Flux Events*

Figure 2 (upper left) shows the NDJFM daily climatology of THF and the associated standard deviation for the GSR and KER, respectively, based on the 61 years of NCEP-NCAR reanalysis. Similar results are obtained using other reanalysis data sets, i.e., NCEP-CFSR and 20CRV2, as well as the OAflux data set, indicating the robustness of the results. In both the KER and GSR, the THF reaches the peak value during January, suggesting that the strongest air-sea interaction takes place during this time

period. However, the THF climatology value is considerably higher in the KER (~250 $Wm^{-2}$) than in the GSR (~220 $Wm^{-2}$). The THF also displays a stronger seasonal variation in the Pacific than in the Atlantic, consistent with the stronger variability of the Kuroshio path than the Gulf Stream path (not shown). Despite of the larger THF climatological value in the KER, its standard deviation is smaller than that of the GSR, suggesting that the storm activity in the GSR has stronger variability than in KER. This may be attributed to the difference in land-ocean distribution between the KER and GSR with the latter being closer to the continent and thus experiencing stronger CAOs. Figure 2 (upper left) also show that the daily THF climatologies in both regions are below the HF80 threshold value, indicating that the HF80 is suitably chosen to define the extreme flux events.

The histograms shown in Figure 2 summarize the general characteristics of the extreme flux events. The average number of extreme flux event days for the 61 winters in NCAR-NCEP reanalysis is about 30 for each winter in both the Pacific and Atlantic, which accounts for only 20% of the entire winter (NDJFM) days while the average contribution of extreme flux events to the total THF reaches 31% for the Pacific and 33% for the Atlantic. Figure 2 b and c shows that the KER has a broader range of variability with higher median value in terms of extreme flux event occurrences and fraction of event-day THF contribution to the total THF in each winter than the GSR does. During the 61-year record, for example, there were 20 (16) winters in the KER (GSR), when the extreme flux event occurrence reached higher than 40 days in each winter and the event-day THF contributed to more than 40% of the total winter THF. It

is also clear from Figure 2 d that the majority of the extreme flux events last less than 3 days with 85% (88%) extreme flux events in the KER (GSR) having a life cycle shorter than 3 days. Average duration of the less-than 3-day extreme flux events in the KER (GSR) is about 1.75 (1.63) days. It is worth noting that almost all the extreme flux events identified in the 61-year NCAR-NCEP reanalysis have a life span of less than 8 days in both the KER and GSR, consistent with the notion that these extreme flux events are closely associated with synoptic-scale storms. This justifies the use of a 1-8 day band-pass filter before composite analysis is performed as described in the previous section. Our findings are also consistent with the results of SH10 and support the conclusion that a relative small number of extreme flux events makes a significant contribution to the total surface turbulent heat in the winter season in the western boundary current regimes and these extreme flux events are closely related to synoptic-scale atmospheric variability.

We repeated the above analyses using the other two reanalysis products and the OAflux data set and found consistent results (not shown). Therefore, we conclude that the finding of extreme flux events contributing significantly to the winter THF in both the KER and GSR regions is not sensitive to datasets and analysis periods.

*2.3.2 Synoptic Storms Associated With Extreme Flux Events*

To further test the idea that the extreme flux events are closely related to CAOs, we performed a composite analysis of atmospheric surface variables, including THF, surface air-temperature, specific humidity, sea level pressure (SLP) and surface winds. Different from the composite analysis in SH10, we first applied a 1-8 day band-pass

filter to the data to isolate synoptic-scale storms from large-scale atmospheric flows and then performed composite analyses on the filtered data as described in the previous section. In such a way, we hope to build a direct link between synoptic-scale storms to the extreme flux events.

The event-day composite of the filtered data exhibits a clear wave pattern with an intense heat loss near the KER and GSR regions and a heat gain further to the east (Figure 3, top). The strong heat loss is accompanied by a cold and dry air mass anomaly in the regions during event days (Figure 3, middle). The event-day composite of SLP and surface winds shows a dipole-like pattern centered near the KER and GSR regions with an anomalous cyclone to the east of the regions and an anti-cyclones to the west, in between which are strong northwesterlies (Figure 3, bottom). The strongest winds collocate with the largest pressure gradient due to geostrophy. Overall, the resultant patterns bear a close resemblance to the classical patterns of CAOs in the both ocean basins (Wheeler et al. 2011; Colucci and Davenport 1987).

However, there are obvious differences between the CAOs in the Pacific and Atlantic. For the Pacific CAOs, the cold and dry surface air carried by the northwesterlies originated from the northeastern part of the Eurasian continent first encounters the relatively warm ocean water in the marginal seas west of Japan before reaching the KER. The air-sea exchange over the marginal seas causes latent and sensible heat loss from the ocean to the atmosphere and reduces the strength of the Pacific CAOs over the KER (Figure 3, top left), In contrast, the Atlantic CAOs directly carry cold and dry Canadian air mass to the warm Gulf Stream, resulting a more intense

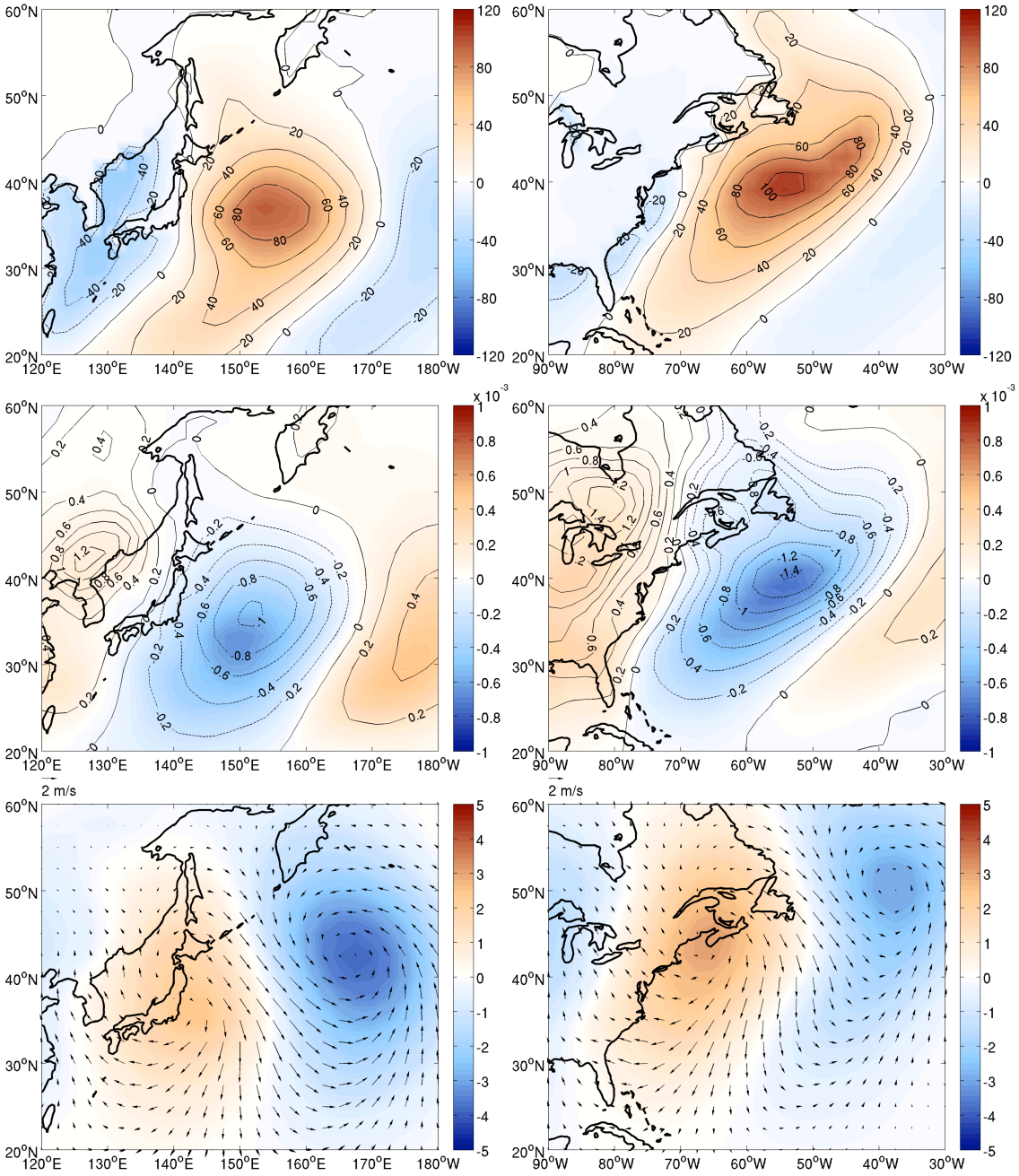


Figure 3. Event day composites derived by averaging 1-8 day band-pass filtered data based on NCEP-NCAR reanalysis. THF (color shaded and contours, W/m$^2$, upper left), 2m air temperature (contours, °C) and specific humidity (color shaded, kg/kg) (middle left), SLP (color shaded, mb) and 10m wind (vector, m/s) (bottom left) in the KER in the Pacific; right, same as left column figures but for the GSR in the Atlantic.

air-sea exchange over the GSR than in the KER (Figure 3, top right). As a result, the Atlantic CAOs have higher intensity than its Pacific counterparts, as shown in Figure 3. We refer to the CAOs as "cold storms" in the following discussion. Additionally, in the Pacific the most significant THF loss occurs along the Kuroshio Extension after the separation of the Kuroshio from Japan, whereas the THF loss in the Atlantic is tilted along a southwest-northeast direction with the maximum heat loss located further north, close to the continent. These HTF differences are closely linked to the differences in the underlying western boundary currents (Kelly et al. 2010). The Kuroshio lies roughly parallel along 35°N after it encounters the Oyashio current from the north, whereas the GS, after its separation from Cape Hatteras, flows northeastward. We note that these results from the composite analysis are not sensitive to the region where the extreme flux time series is taken.

The nonevent-day composite reveals nearly exact opposite patterns to those of the cold storms, albeit with a reduced amplitude (Figure 4). In particular, southerly winds prevail over the region of maximum THF anomaly with a low SLP anomaly to west and a high SLP anomaly to the east. Instead of transporting the cold and dry continental air over the warm currents, the southerly winds bring the warm and moist air from the subtropics to the regions, reducing the latent and sensible heat release from the warm currents. We refer to these storms as "warm storms". Therefore, during nonevent days that occupy most of the winter season, the warm storms dominate the synoptic-scale atmospheric variability over the KER and GSR.

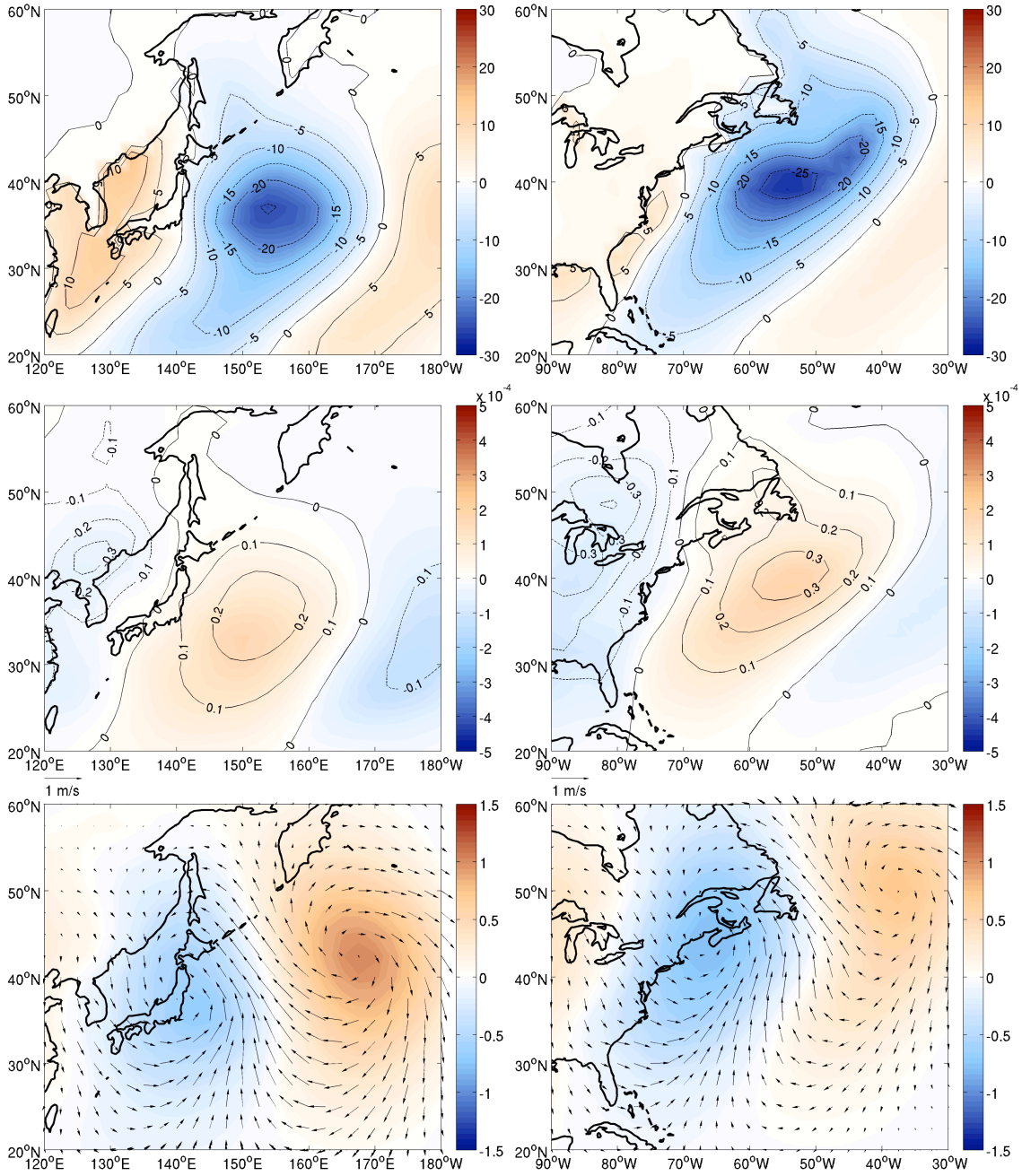


Figure 4. Same as Figure 3, but for non-event day composites.

We also performed a composite analysis following SH10, i.e., simply averaging the relevant surface variables for all the event days and nonevent days without using the

band-pass filter and then taking the difference between the two. The results reveal similar storm patterns to those shown in Figure 3 and 4, confirming that the extreme flux events are primarily caused by CAOs in these regions.

*2.3.3 Variability of Extreme Flux Events*

To determine the contribution from the extreme flux events to the total winter-mean THF variability in the KER and GSR, we divided the total THF variability into two components: one induced by extreme flux events and the other induced by non-flux events. The former, named as event-day THF, was derived by integrating sensible heat flux (SHF) and latent heat flux (LHF) during event days in each winter season, while the latter, named as nonevent-day THF, were computed by integrating SHF and LHF during non-event days. Obviously, the sum of the event-day and nonevent-day THF gives the total THF in each winter.

Figure 5 (top left and right) shows the total, nonevent-day and event-day THF over the KER and GSR derived from the three different reanalysis datasets. Overall, the three datasets show reasonable agreement in the overlapping periods. In particular, the correlation between NCEP-CFSR and NCEP-NCAR THF is above 0.9 for both the KER and GSR over the 31-year period from 1979-2009. The correlation between 20CRV2 and NCEP-NCAR over the 63-year period from 1948-2009 is about 0.7, demonstrating that the interannual and long-term time scale variability of the KER and GSR THF is well captured by all three reanalysis products. An examination of the nonevent-day and event-day THF clearly indicates that the latter contains much higher variance than the former. The standard deviation for the event-day THF is $4.0 \times 10^8$ $Jm^{-2}$ and $3.3 \times 10^8$ $Jm^{-2}$

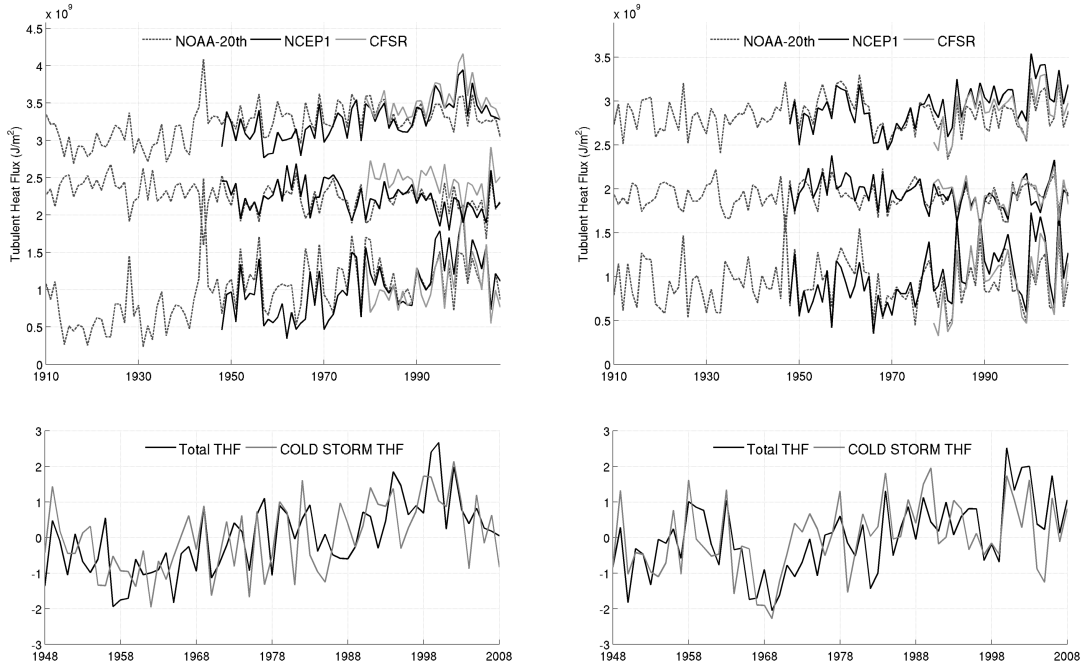


Figure 5. Upper, total winter season THF (top), non-event day THF (middle), event-day THF (bottom) in the KER (left) and GSR (right) for 20CR (dashed), NCEP-NCAR (black solid), NCEP-CFSR (gray solid) reanalysis, respectively. Lower, normalized total THF (black) and cold storm induced THF (gray) in the KER (left) and GSR (right) based on NCEP-NCAR reanalysis. The cold storm induced THF is derived by first regressing the 1-8 day bandpass filtered daily SLP onto the event day composite of SLP and then integrating THF over the days during which the regression coefficient exceeds 1.0.

for the KER and GSR, respectively, compared to $2.0 \times 10^8$ $Jm^{-2}$ and $1.7 \times 10^8$ $Jm^{-2}$ for the nonevent-day THF based on NCEP-NCAR data. Furthermore, the event-day THF is highly correlated with the total THF with a correlation value of around 0.9 for both the KER and GSR. The percentage of total THF variance explained by the event-day THF is 73%, 79%, and 83% for NCEP-CFSR, NCEP-NCAR, 20CRV2 reanalysis data, respectively, in the KER. The corresponding values for the GSR are 85%, 75%, and 70%, respectively. In contrast, the correlation between the total THF and nonevent-day THF is much lower (~0.3) for all the reanalysis data in both regions, which is

statistically insignificant at 95% confident level. These results strongly suggest that CAO-induced extreme flux events practically determine the winter season turbulent heat exchange between the atmosphere and ocean in both the KER and GSR. The conclusion is entirely consistent with the finding of SH10 based on NCEP-NCAR reanalysis, pointing to the critical role of synoptic scale storms in the climate system in the western boundary current regimes.

To further validate that it is the cold storms that are mainly responsible for interannual and longer time scale THF variability, we performed the following analysis. First we regressed the 1-8 day bandpass filtered daily SLP onto the event-day SLP composites in the KER and GSR, respectively, which exhibit "cold storm" structure (Figure 3, bottom left and right). We then examined the regression time series and divided the values into above and below 1.0. Note that since the regression time series are dimensionless, the value of 1.0 gives a regressed pattern that is identical to the composite "cold storm", assuming that the residual is negligibly small. Therefore, this value is used to identify the occurrence of CAOs in the KER and GSR. Finally, we integrated the THF for the period when the regression time series is above 1.0 in each winter. Figure 5 (bottom left and right) shows the normalized time series of the integrated THF in the KER and GSR for the 61 winters from 1948 to 2008 based on NCEP-NCAR reanalysis, overlaid by the normalized total THF time series derived by the area-averaged method shown in Figure 5 (top). As expected, the two time series are highly correlated with r=0.6 in the KER and r=0.7 in the GSR. This further verifies the

finding that the "cold storm" activity essentially determines the year-to-year variability of the THF in the KER and GSR.

It is evident from Figure 5 (top left and right) that the activity of extreme flux events in the KER and GSR has exhibited strong variability at both interannual and decadal and longer time scales. For the past 30 years (1979-2009), all three reanalysis data sets show decadal variations in the KER THF with lower THF before 1990s and higher value after 1990s, although the amplitude of the variation is much more pronounced in NCEP-NCAR and NCEP-CFSR than in 20CRV2. However, no statistically significant trend is detected in the KER THF during this time period. In contrast, the GSR THF exhibits a statistically significant upward trend with a value of $1.2 \times 10^8$ $Jm^{-2}$ per decade in NCEP-NCAR and NCEP-CFSR reanalysis and a weaker but still significant trend of $0.9 \times 10^8$ $Jm^{-2}$ per decade in 20CRV2. The upward trend in the GSR THF is verified using the observationally derived OAFlux data set (1985-2009). These decadal and longer time scale THF variabilities are likely related to changes in the Pacific and Atlantic storm tracks as shown in many previous studies (Miller et al. 1994; Chang and Fu 2002; SH10; Lee et al. 2011). For example, Chang and Fu (2002) show that the Pacific storm track appeared to be strengthened after 1990s, consistent with the observed increase in the KER THF. Chang (2007) also show that the Atlantic storm track activity has experienced an upward trend during the past decades. SH10 further argue that the trend in the GSR THF is largely attributed to an increase in Atlantic CAOs, which causes cooling over the Northeastern America and Eastern Canada and enhances heat losses in the GSR.

Extending the reanalysis record back in time reveals a statistically significant trend in both KER and GSR THF during the last 60 years (1948-2009) and the trend clearly comes from the event-day contribution to the THF as consistently shown by both NCEP-NCAR and 20CRV2 reanalysis. This finding is consistent with recent studies of long-term trend of north hemisphere storm track activities (e.g., Chang 2007), which demonstrate positive trends in storm track activities, particularly in the Atlantic sector. The secular changes in KER and GSR THF are much weaker and statistically insignificant in the early part of the last century (1910-1947) as shown in 20CRV2 reanalysis, pointing to the possibility that the trend during the last 60 years may be linked to anthropogenic climate change. However, caution should be exercised when interpreting reanalysis data in the early part of the last century because of the scarcity and inaccuracy of the observations. The sharp increase in the KER THF during the mid-1940s may be linked to data quality issues, although a full investigation on this issue is beyond the scope of this study.

In summary, the analysis of the KER and GSR THF indicate that even though the nonevent-day fluxes contribute more dominantly to the winter mean THF in these regions, the decadal and longer time scale variability of the THF is almost entirely determined by the event-day fluxes that are closely related to winter storm activities, particularly CAO activities, in the regions. Next, we investigate the relationship between event-day flux variability and modes of climate variability in the North Pacific and Atlantic.

## 2.4 Relationship between Extreme Flux Events and Modes of North Pacific and Atlantic Variability

It has been well documented that the leading modes of variability are the PDO and the North Pacific Oscillation (NPO) in the north Pacific sector (Rogers 1981; Mantua et al. 1997) and the NAO and the EAP in the north Atlantic sector (Van Loon and Rogers 1978; Barnston and Livezey 1987). These modes of variability can be described in terms of empirical orthogonal function (EOF) analysis on winter mean SLP anomalies (Newman et al. 2003; Di Lorenzo et al. 2008; Chhak et al. 2009; Hurrell and Deser 2009). The PDO and NPO are typically captured by the first and second EOF of winter mean SLP anomalies in the north Pacific sector (Newman et al. 2003; Di Lorenzo et al. 2008), while the NAO and EAP are represented by the two leading EOFs of the SLP anomalies in north Atlantic sector (Thompson and Wallace 1998; Rogers 1990). In this study, we focus on the PDO and the EAP, as we will demonstrate that these two modes of variability are closely linked to the event-day flux variability in the KER and GSR, respectively.

Figure 6 shows the PDO as the leading EOF of the north Pacific winter SLP anomaly and the EAP as the second EOF of the north Atlantic winter SLP anomaly, respectively, using the 61-year NCEP-NCAR reanalysis data. The PDO explains approximately 45% of winter SLP anomaly variance in the north Pacific between 20°N and 70°N, while the EAP explains 20% of the north Atlantic winter SLP variance in the same latitudinal band. Repeating the same analysis using the 100-year 20CRV2 reanalysis data yields very similar patterns, except that the explained variances by the

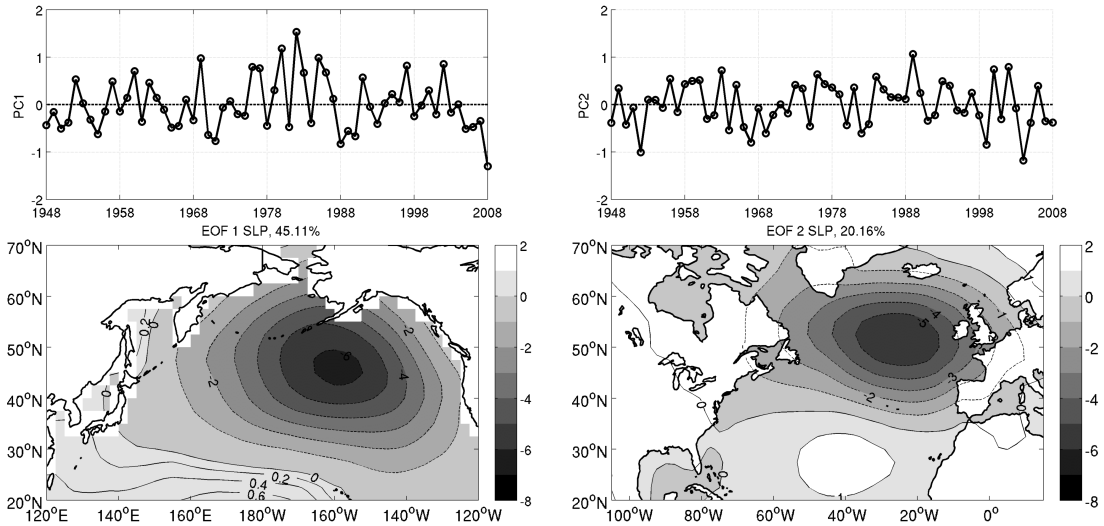


Figure 6. Left, time series (top) and spatial pattern (bottom) of first EOF derived from NDJFM SLP anomalies for NCEP-NCAR reanalysis (shaded and contours, contour intervals are 1mb) in the North Pacific. Right, time series (top) and spatial pattern (bottom) of second EOF based on NCEP-NCAR NDJFM SLP anomalies (shaded and contours) in the North Atlantic.

PDO and EAP change to 44.5% and 27.4%, respectively. The corresponding principle component (PC) time series are shown in Figure 6 (top left and right panels). We use the standardized PCs (normalized by the corresponding standard deviation) to define a PDO and EAP index, respectively. All the EOFs and PCs are based on the detrended and area-weighted winter-time (NDJFM) SLP anomalies. To study the relationship between extreme flux events in the KER (GSR) and modes of decadal variability in the North Pacific (North Atlantic), we also defined an extreme flux event index by taking the number of days in each winter when the THF exceeds HF80 value, which is basically the THF time series shown in Figure 5 (top left and right). Only the results from NCEP-NCAR are discussed below.

To investigate the relationship between event-day flux variability and modes of

climate variability in the North Pacific and Atlantic, we first perform a simple correlation analysis between the standardized extreme flux event index in the KER and the PDO index, as well as between the GSR event index and the EAP index. The results are shown in the scattered plot (Figure 7). The correlation between the KER event index and the PDO index is about 0.42, while the correlation between the GSR event index and the EAP index approaches 0.65, both of which are significant at 95% confident level based on a student's T-test. It suggests that the extreme flux event activity is linked to these modes of variability.

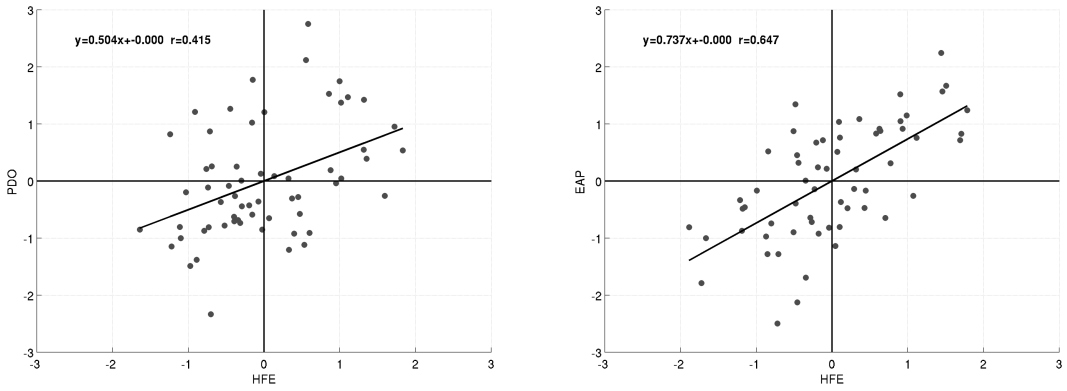


Figure 7. Left, scatter plot between standardized extreme flux event index in the KER and PDO index calculated by NCEP-NCAR winter season (NDJFM) SLP anomalies. Oblique line shows the linear regression with r=0.415 which is significant at 95% confident level. Right, same as left figure, but for scatter plot between standardized extreme flux event index in the GSR and EAP index in the Atlantic.

To further validate this finding, we performed an SVD analysis on event-day THF and winter mean SLP anomalies in the north Pacific and Atlantic, respectively. The event-day THF anomalies are defined as accumulated THF anomalies at each grid point

during the event days according to the HF80 threshold. Figure 8 (top) shows spatial patterns of the first SVD of event-day THF and SLP in the north Pacific, which explains 26.93% of the total squared covariance. The resultant SLP SVD (Figure 8, top right) depicts an intensified Aleutian Low that resembles a typical positive-phase PDO SLP pattern (Figure 6, bottom left). The corresponding time series of the first SLP SVD is nearly identical to the PDO index with a correlation coefficient between the two as high as 0.99, indicating that the first SVD reproduces very well PDO variability (Figure 8, bottom right). The first THF SVD displays, as expected, significant loading in the KER where the extreme flux events were defined (Figure 8 top left). The corresponding THF time series is highly correlated with the PDO index with a correlation coefficient of 0.63 and with the extreme THF index with a correlation coefficient of 0.76, indicating that the SVD depicts the co-variability between extreme THF events and PDO (Figure 8,b bottom right). The broad patterns of SLP and THF derived from the SVD analysis are consistent with the results shown by Miller et al. (1994) who studied the 76/77 climate shift in the Pacific basin. To quantify the percentage of total winter THF variance explained by the first THF SVD, we projected the winter THF anomaly onto the THF SVD and found that over 40% of total THF variance can be explained by the first SVD in the region where extreme flux events are defined (Figure 8, bottom left).

Figure 9 (top) shows the second leading SVD between event-day THF and winter mean SLP anomalies in the north Atlantic, which explains 22.9% of the squared covariance. The SLP SVD (Figure 9, top right) shows a nearly identical pattern to that of EAP (Figure 6, bottom right) and the corresponding SVD time series is highly correlated

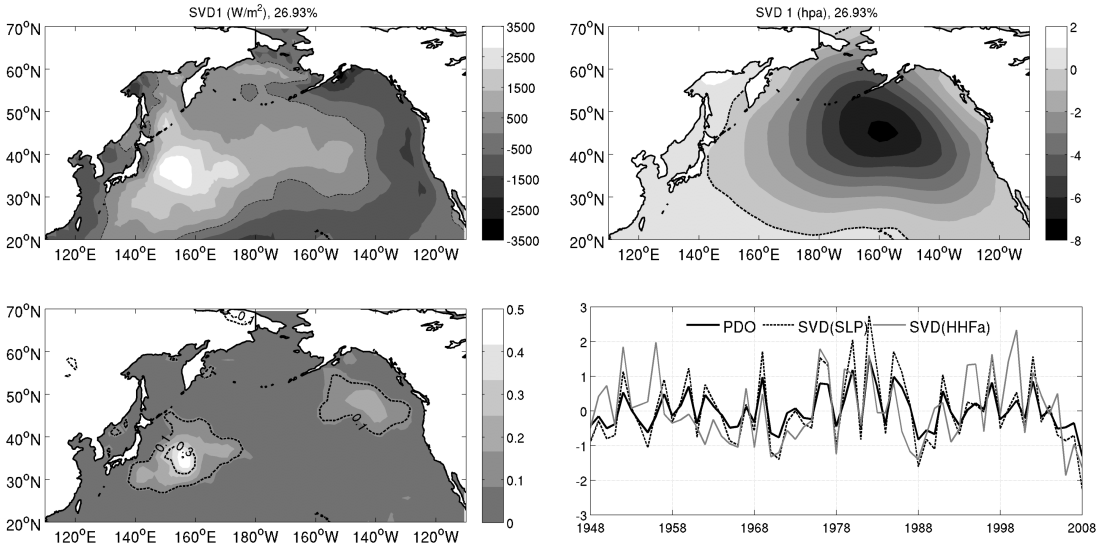


Figure 8. First SVD between event-day THF and NDJFM SLP anomalies in the North Pacific derived from NCEP-NCAR reanalysis. Spatial pattern (top) for event-day THF anomalies (left) and SLP anomalies (right), 0 value is shown by dashed lines; time series (bottom right) for event-day THF anomalies (gray solid) and SLP anomalies (dashed) overlaid with PDO index (black solid). Bottom left, contribution (percentage) to the total THF variance from the first THF SVD (shaded and contours).

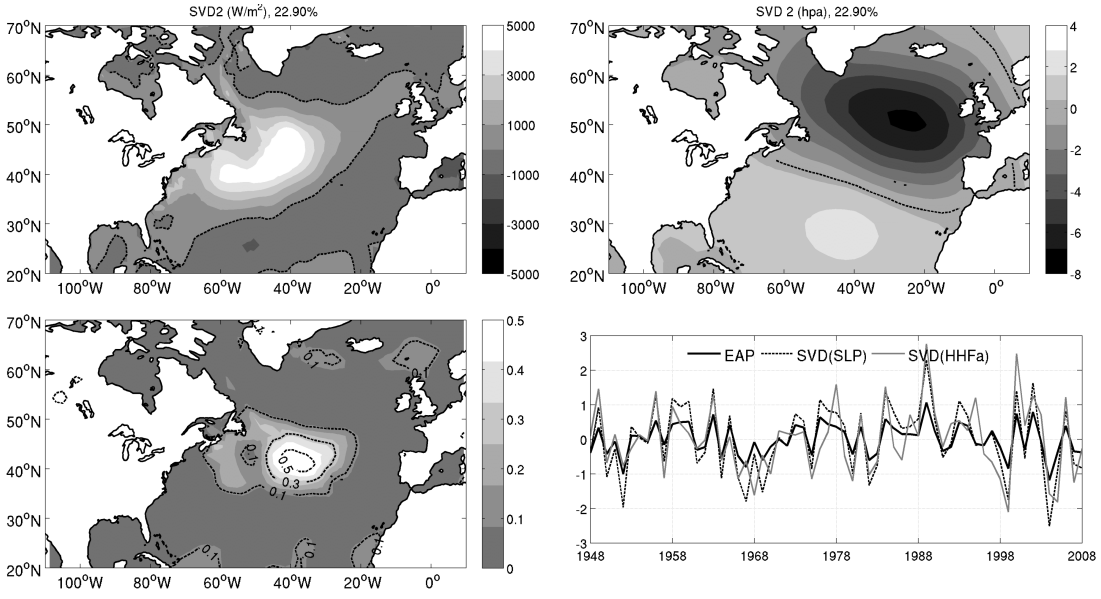


Figure 9. Same as Figure 8 but for second SVD between event-day THF and NDJFM SLP anomalies in the North Atlantic.

with the EAP index at 0.99, indicating that the SVD captures the full spectrum of EAP variability (Figure 9, bottom right). The THF SVD shows large loading in the GSR (Figure 9, top left) and the THF time series is correlated with the EAP index at 0.78 and with the Atlantic extreme flux event index at 0.82 (Figure 9, bottom right). The total variance of THF explained by the first SVD is over 50% though the maxima center is downstream of GS (Figure 9, bottom left). These results confirm the linkage between extreme flux events in the GSR and EAP variability. Therefore, PDO and EAP share commonality that their variability is connected to the occurrence of extreme flux events in the corresponding western boundary current regions.

The above analysis reveals a close relationship between extreme flux events in the KER and GSR and PDO and EAP in the North Pacific and North Atlantic, respectively. In an attempt to identify the causality, we selected all the positive PDO years based on the PDO index. Lag composite was then made using daily SLP anomalies on extreme flux event days during the positive PDO years using the HF80 threshold for each winter. Figure 10 (left) shows the evolution of the composite SLP anomalies starting from the onset of the extreme event (lag 0) to 3 days later (lag 1, 2 and 3) in the Pacific. A typical extreme flux event originated in the KER is accompanied by a weak high SLP anomaly in the west and a strong low SLP anomaly in the east, consistent with the CAO storm structure shown in Figure 3. As the storm develops, the SLP anomalies, particularly the low SLP anomaly, move eastward and gradually decay, leaving a negative SLP anomaly deposited in the eastern side of the basin, which contributes to the intensified Aleutian Low for positive PDO phase (Figure 6, bottom left). Similar evolution pattern is also

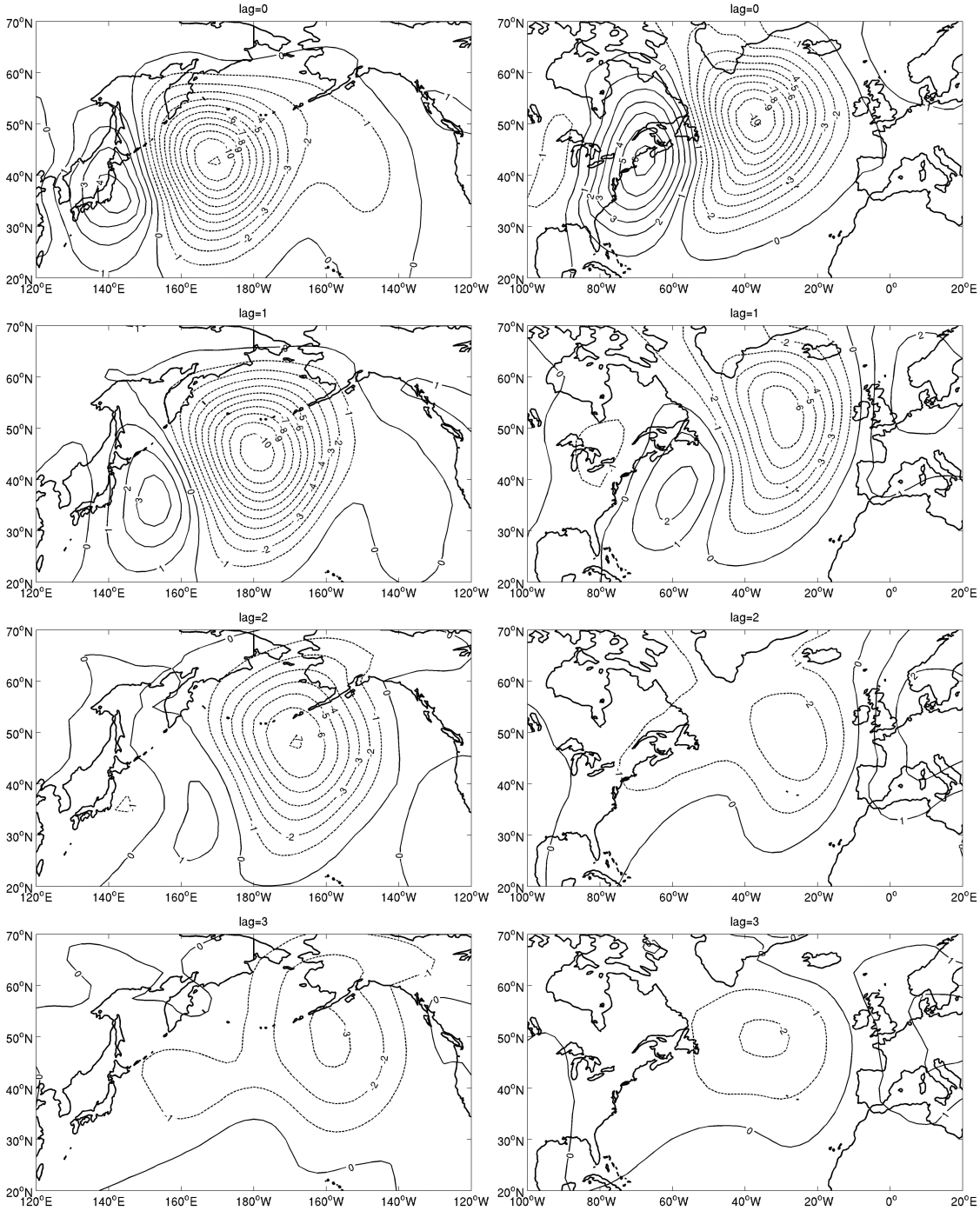


Figure 10. Lag composites of daily SLP anomalies (contours, mb) in the KER (left) and GSR (right) derived from 61 winter season(NDJFM) NCEP-NCAR reanalysis based on event-day index. The event-day index is constructed using the HF80 threshold for daily THF in each NDJFM. Lag=0 (1, 2, 3) corresponds to SLP anomalies lagging extreme flux event 0 (1, 2, 3) day.

found in the Atlantic sector (Figure 10, right). The negative SLP anomaly associated with extreme flux events in the GSR is carried downstream, leading to the low-pressure anomaly similar to that of the EAP pattern (Figure 6, bottom right). In fact, if we just sum up the SLP anomalies from lag 0 to lag 6 in the Pacific and Atlantic and divided by the entire winter days (the number of days summed up counts for 23% and 28% of the entire winter days in the North Pacific and North Atlantic, respectively), the resultant SLP anomalies bear a striking resemblance to the winter-mean SLP anomalies associated with the positive phase of the PDO and EAP (Figure 11, top and middle). On the other hand, the SLP anomalies averaged for the rest of the winter days in these years show little resemblance to the PDO and EAP SLP anomalies (Figure 11, bottom). These results suggest that the SLP anomalies during positive PDO and EAP phases can be explained as a rectified effect of the synoptic CAO storms in the north Pacific and Atlantic. This explanation is at odd with the hypothesis that large-scale SST variability is driving the modes of climate variability (e.g., Latif and Barnett 1994; Rodwell et al. 1999), but is in line with the previous studies that emphasizes the importance of synoptic scale storms in changing the low frequency mode of climate variability (e.g., Feldstein 2003; Benedict 2004; Rivere and Orlanski 2007).

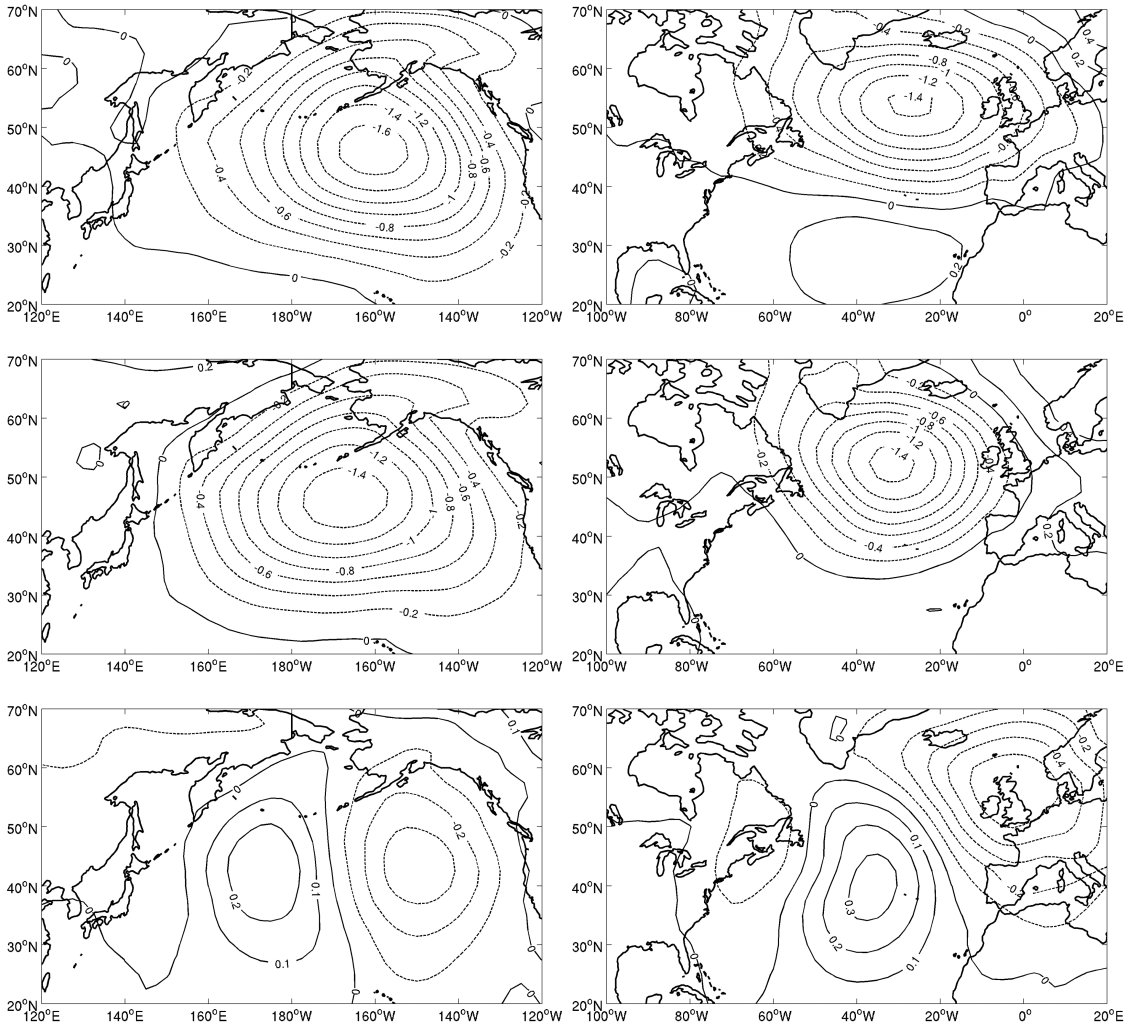


Figure 11. Top left, winter season (NDJFM) mean SLP anomalies (contours, mb) during positive phase of PDO in the North Pacific derived from NCEP-NCAR reanalysis; middle left, composites of event-day SLP anomalies during positive phase of PDO integrated from lag 0 day to lag 6 day; bottom left, composites of nonevent-day SLP anomalies during positive phase of PDO integrated in the rest of days. Right panel, same as the left panel but for SLP anomalies during positive EAP phase in the North Atlantic. The sum of event-day composite (middle) and nonevent-day composite (bottom) gives the winter season mean SLP anomalies (top).

The next question is then how extreme flux event variability in the KER and GSR relates to Pacific and Atlantic storm track variability, respectively? To examine this

question, we applied the SVD analysis to the winter season event-day THF anomaly and 1-8 day band-pass filtered 300hpa v-wind product, i.e., <v'v'>. The leading SVD and the corresponding time series for the north Pacific sector are shown in Figure 12 (left). The THF SVD again picks out the large THF signal in the KER similar to that shown in Figure 8 (top left). The co-varying storm track pattern shows a dipole-like structure with a positive loading in the southeastern North Pacific and a negative loading in the northern part of North Pacific, suggesting a southward shift of the upper level storm track. The most significant change in the upper level storm track occurs in the downstream of the KER in the southeastern North Pacific basin close to the North America continent. A similar pattern of Pacific storm track changes is obtained when the SVD analysis was applied to <v'v'> and winter mean SLP anomalies over the north Pacific sector, as shown by Figure 12 (right) in which the leading SLP SVD bears a close resemblance to the PDO pattern (Figure 6 left). The two leading SVD time series of the storm track variability are also highly correlated with each other with a correlation coefficient of 0.92. Furthermore, the SLP and THF SVD time series are correlated with the PDO index and the Pacific extreme flux event index at 0.99 and 0.78, respectively. These results point to a close relationship among the extreme flux events in the KER, the upper level storm track in the north Pacific and the PDO. A positive PDO corresponds to an enhanced activity of extreme flux events in the KER and a southward shift of the upper level Pacific storm track. Opposite tends to occur during a negative PDO phase.

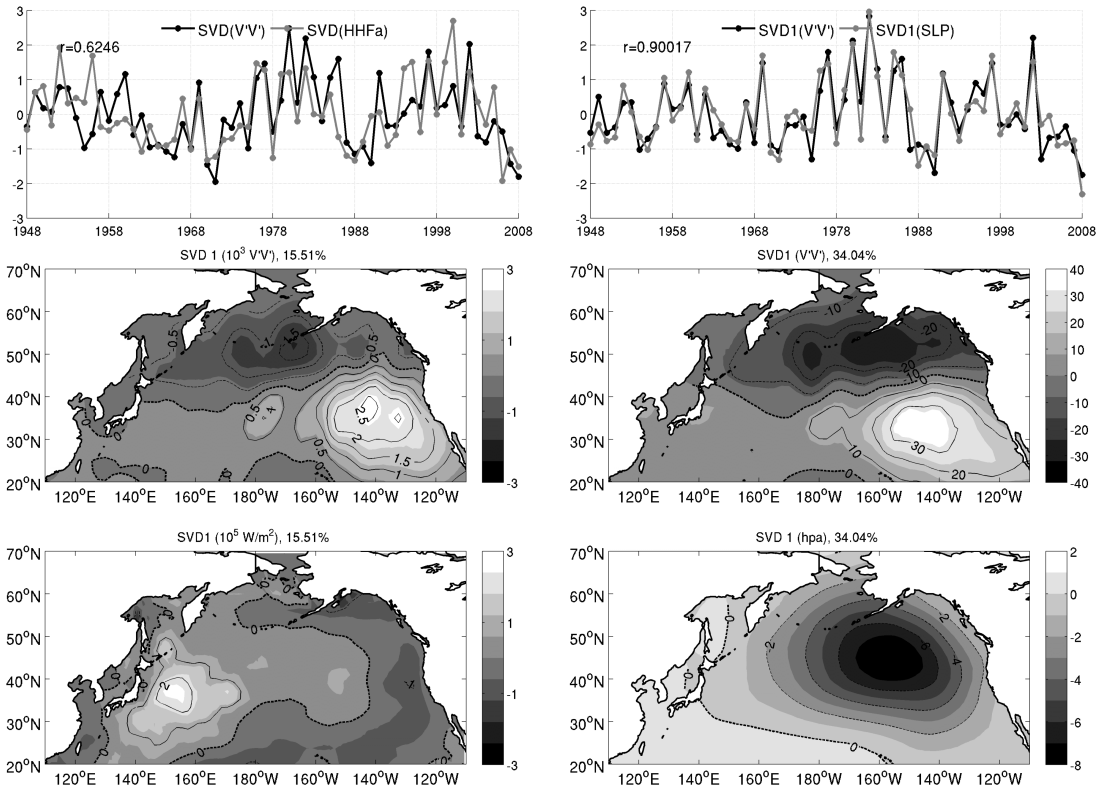


Figure 12. Left, first SVD between NDJFM event-day THF and 300hpa <V'V'> in the North Pacific derived from NCEP-NCAR reanalysis. Top, time series of event-day THF (gray) and 300hpa <V'V'> (black); middle, spatial pattern of 300hpa <V'V'> (shaded and contours); bottom, spatial pattern of event-day THF (shaded and contours). Right column, similar to left column, but for first SVD between NDJFM SLP anomalies and 300hpa <V'V'> in the North Pacific. For all the spatial patterns, positive values are plotted in solid contours and negative values in dashed contours.

Similar SVD analyses were performed for the north Atlantic sector. Figure 13 shows the second leading SVDs between <v'v'> and event-day THF anomalies and between <v'v'> and winter-mean SLP anomalies over the north Atlantic sector. In comparison with the Pacific counterparts, the explained squared covariance by these second SVDs is lower and in the range of 15%-20%. The two resultant SVDs for the

upper storm track show similar structure, consisting of an enhanced storm activity over the eastern North Atlantic basin and reduced storm activity in the GSR and Greenland-Iceland-Norwegian (GIN) seas region, in correspondence to an enhanced extreme flux events in the GSR and a positive phase of the EAP (Hatzaki et al. 2010). The two SVD time series of storm track are highly correlated at 0.96, suggesting that they represent the

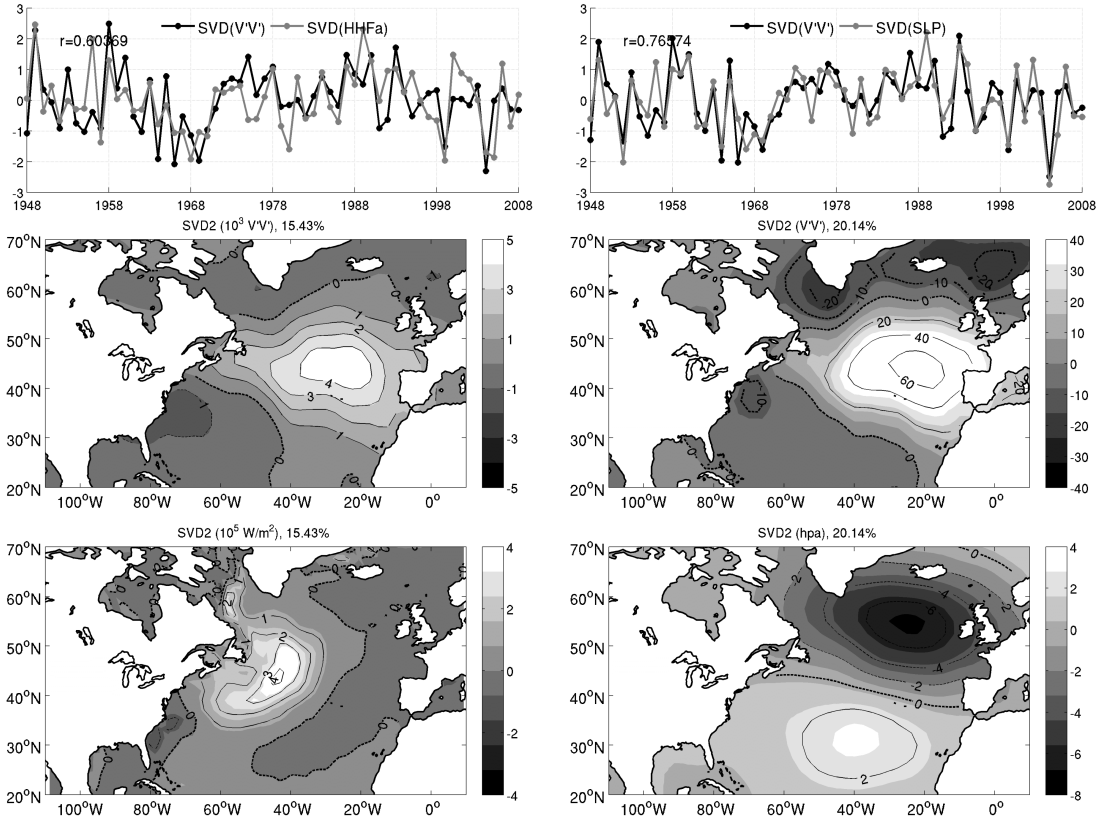


Figure 13. Left, same as Figure 12 (left) but for second SVD between NDJFM event-day THF and 300hpa <V'V'> in the North Atlantic. Right, same as Figure 12 (right) but for second SVD between NDJFM SLP anomalies and 300hpa <V'V'> in the North Atlantic.

same physical phenomenon. The EAP has been linked to Euro-Atlantic blockings (Hakkinen et al. 2011; Scherrer et al. 2006), and thus the resultant storm track change is also likely related to Euro-Atlantic blocking activities (Woollings et al. 2008; Dong et al. 2013). Given that the THF and SLP SVD time series are significantly correlated with the GSR extreme flux event index and the EAP index at 0.73 and 0.94, respectively, the resultant two SVD pairs suggest that the extreme flux event activity in the GSR, the Atlantic storm track and the EAP variability are closely related.

To probe deeper into the relationship between synoptic storm activities in the KER and GSR and north Pacific and Atlantic storm tracks, we performed the following composite analysis. First, winter season storms were divided into two groups: event-day storms and nonevent-day storms according to the HF80 criterion, and then lag composite of 1-8 day bandpass filtered 300hpa geopotential height field was made for the two groups of storm events using the respective THF time series in the KER and GSR from 4 days before to 4 days after the maximum THF. Figure 14 compares the evolution of the two groups of storms in the north Pacific sector from lag -1 (lead 1) day to lag 2 day. Originating from the Northeastern Eurasian continent, both groups of storms gradually grow and reach their peak around lag 0/1 day when passing through the KER. There is a clear asymmetry in storm strength about lag 0 day with larger storm amplitude at lag 1 day than at lag -1 day, suggesting that the storms gain strength as they pass through the KER. Interestingly, the nonevent-day storms appear to grow at a larger rate than the event-day storms. This growth-rate difference between the two groups of the storm could be related to the suppression effect on baroclinic growth near the KER by the East Asian

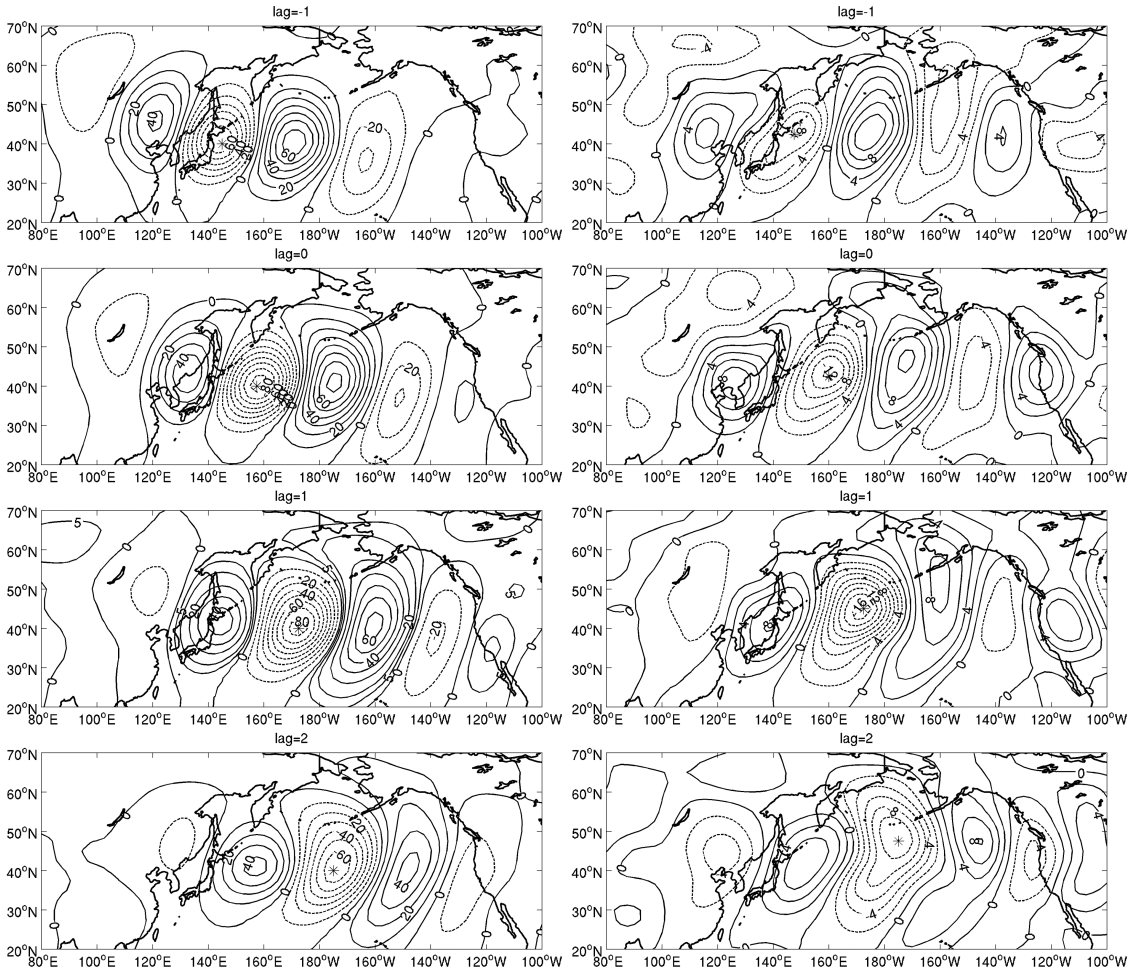


Figure 14. Lag composite of 1-8 day band-pass filtered 300hpa geopotential height for event-day storms (left) and nonevent-day storms (right) derived from 61 winter season (NDJFM) NCEP-NCAR reanalysis (contour intervals are 10m for event-day composites and 2m for nonevent-day composites). Event-day storms and nonevent-day storms are again picked out by HF80 threshold.

Winter Monsoon, as argued by Nakamura et al (2002). Another major difference between the two groups of storms occurs as they propagate downstream: the event-day storm composites (left panels of Figure 14) prefer a southeastward path, while the nonevent-day storm composites (right panels of Figure 14) prefer a northeastward path. Since the event-day (nonevent-day) storms are associated with stronger (weaker) THF

near the KER, which correspond to a southward (northward) shift of the Pacific storm track as shown by the SVD analysis (Figure 10), the southeastward (northeastward) path of the event-day (nonevent-day) storms is consistent with the storm track change during a positive (negative) PDO phase, suggesting that the shift of the storm track may be attributed to different downstream development between event-day and nonevent-day storms.

Figure 15 illustrates similar storm composites for the north Atlantic sector. It again shows that the event-day (nonevent-day) storms prefer a southeastward (northeastward) downstream propagation path, consistent with the increase (decrease) in storm track activity in the eastern north Atlantic and decrease (increase) in storm track activity in the GIN sea region. Different from the storm growth in the KER, both the event-day and nonevent-day storms have been well developed at lag -1 day and reach their peaks at lag 0 day as they passing the GSR and then gradually decay.

The south shift of storm tracks in the eastern Pacific and Atlantic basin during extreme flux events may be related to Pacific blocking and Atlantic Euro-Altantic blocking activities. As suggested by Croci-Maspoli et al. (2007) the occurrence of Atlantic and Pacific blocking activities are closely related with NAO and Pacific North American (PNA) patterns accompanied by a southward shift of midlatitude storm tracks and the shift of storm tracks may be caused by a displacement of the jet stream (Woollings et al. 2008, 2010). A full investigation of the relationship between the extreme flux events and blocking activities is beyond the scope of this study.

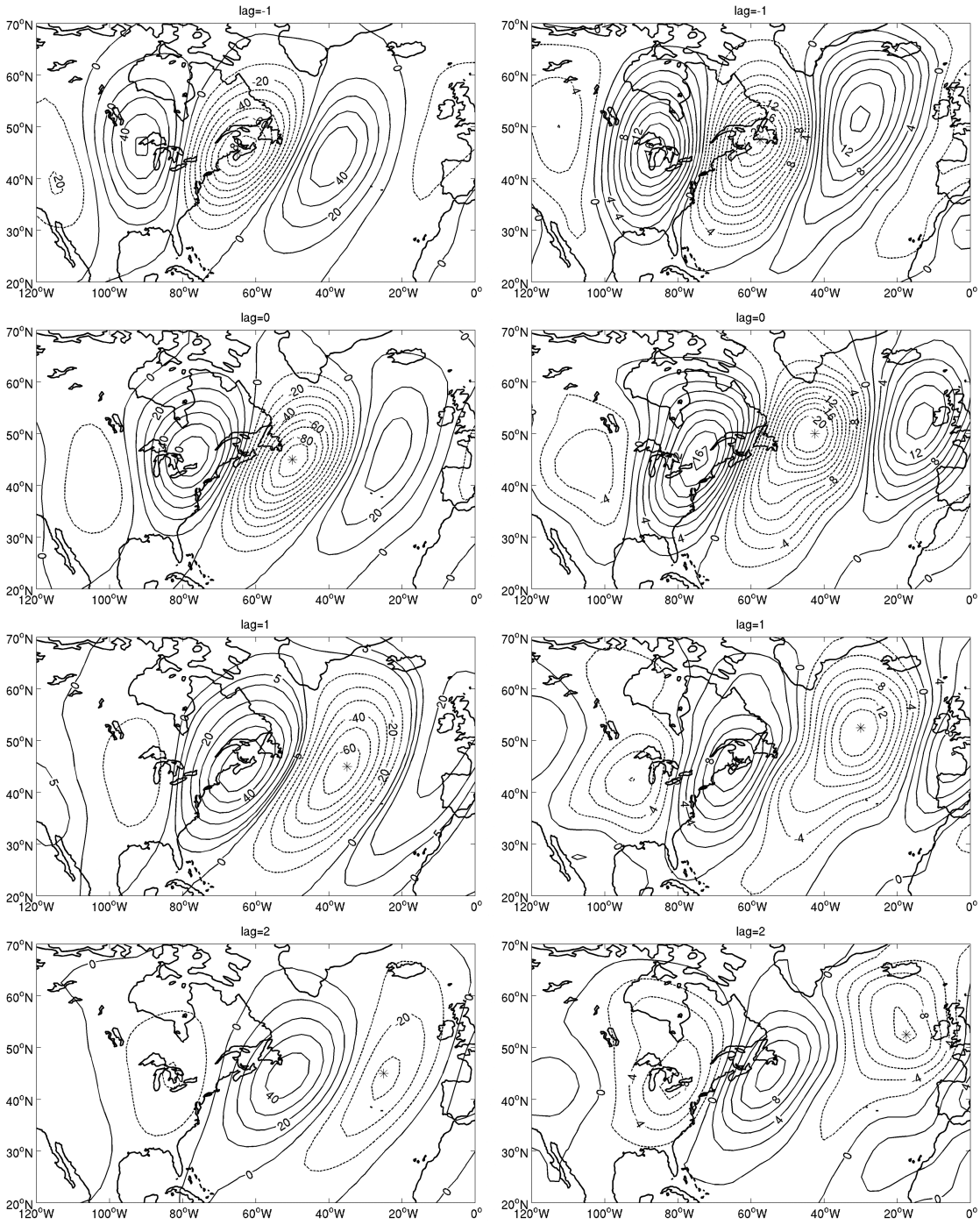


Figure 15. Same as Figure 14 but for storm composites in the North Atlantic.

In summary, the above analyses suggest a cohesive interrelationship among extreme flux events induced by CAOs in the western boundary current regimes, storm track activity and basin-scale modes of climate variability in both the north Pacific and Atlantic. Since the extreme flux events play a vital role in determining local air-sea exchange in the KER and GSR as shown in the previous section, it is natural to ask to whether the variability of the extreme flux events is affected by SST variability along the Kuroshio and the Gulf Stream. The subject of the following section is to investigate this question.

**2.5 Relationship between Extreme Flux Events and SST**

We performed lag-regression analyses between the extreme flux event index and SST anomalies in the north Pacific and Atlantic. The lag between the flux and SST is defined by the shift (in months) between the months used to define seasonal-mean SST anomalies and those, i.e., NDJFM, used to define the extreme flux event index. For example, lag 1-month means that SST anomalies were averaged over DJFMA, lag 2-month means that they were averaged over JFMAM and etc. Figure 16 (left) shows regressed seasonal mean SST anomalies onto the extreme flux event index at lag -3 and lag 3 months over the north Pacific. When the SST leads the extreme flux event index by three month, i.e., lag -3 months, there are statistically significant positive regression values forming along the Kuroshio. The positive SST regressions along the Kuroshio persist from lag -3 month to -1 month (not shown), suggesting that the SST anomalies along the Kuroshio may help fuel the development of extreme flux events in the region. Moving downstream of the Kuroshio, a broad area of statistically significant negative

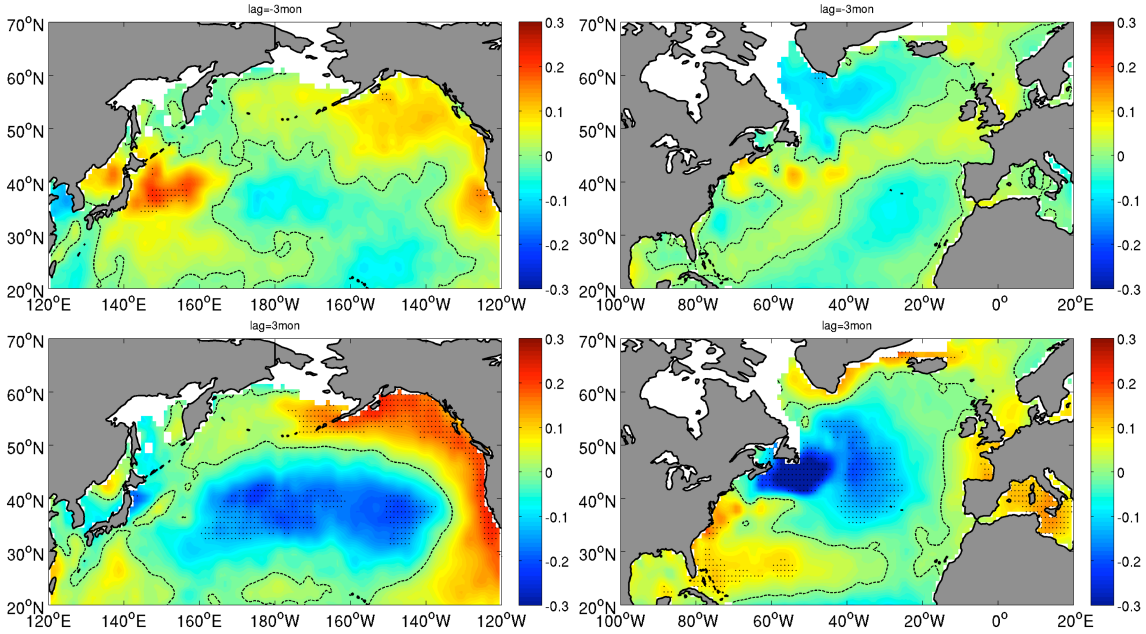


Figure 16. Seasonal mean SST (°C) anomalies regressed onto standardized extreme flux event index in the KER (left) in the North Pacific and GSR (right) in the North Atlantic when SST anomalies lead (top)/ lag (bottom) extreme flux events 3 months. 0 values are highlighted by dashed contours. Regression values significant at 95% confidence level are shaded by black dots.

regression values exists in the central and eastern north Pacific, suggesting a possible negative feedback between the downstream SST and extreme flux event variability. When the SST lags the extreme flux event index by three months, i.e., lag 3 month, the significant positive regressions along the Kuroshio fade away, while the negative regressions downstream increase, suggesting the downstream development of the extreme flux events tends to cool the SST in the central and eastern north Pacific. 3-month is a typical time-scale for ocean mixed layer to respond to changes in the atmospheric surface fluxes. Therefore, these results are consistent with the notion that the sharp SST front along the Kuroshio Extension may interact positively with the

development of synoptic atmospheric systems in the region during the boreal winter, while the SST variability in the central and eastern north Pacific is largely forced by the atmosphere.

Figure 16 (right) shows similar regression maps for the north Atlantic sector. In contrast to the Pacific sector, no statistically significant positive SST regressions are found along the GSR when SST lead extreme flux events by 3 month (lag -3 month) or other months, suggesting that there is relative weak influence of local SST on the extreme flux events in the GSR. However, significant negative SST anomalies in the GSR and positive SST anomalies south of GSR are found when the SST lags extreme flux events by 3 month. This points to an oceanic response to large-scale atmospheric forcing through change of surface wind and turbulent heat fluxes, as noted by previous studies (e.g., Deser and Blackmon 1993).

In summary, although there is a robust large-scale negative SST response downstream of the KER (GSR) in the central (northern) North Pacific (Atlantic) basins, the oceanic influence on the extreme flux events in these WBC regions is generally weak and not clearly identified. A positive fueling effect from the underlying SST is revealed by lag-regression analyses in the KER, while such positive influence is not statistically significant in the GSR. A recent paper by O'Reilly and Czaja (2014) stressed the importance of the sharp SST gradients in affecting the atmospheric storm tracks. It is possible that the extreme flux events in the KER/GSR may relate to variation of underlying SST gradient. However, the lack of a long observed record of high-resolution SST makes it difficult to identify a clear relationship between the extreme flux events

and SST gradient at long time-scales. Further studies are needed to further investigate this problem.

**2.6. Summary**

Based on NCEP-CFSR, NCEP-NCAR, 20CRV2 reanalysis and OAflux datasets, extreme flux events associated with CAOs in boreal winter in the KER and GSR are analyzed and compared in terms of their statistics, spatial structure, interannual-to-decadal and long-term variability. The relationship between extreme flux events in the KER/GSR and modes of climate variability in the North Pacific/Atlantic is also investigated, as well as the associated storm track response. Finally, a potential influence from the underlying ocean on the extreme flux events is discussed.

Extreme flux events associated with synoptic scale atmosphere storms dominate the total surface turbulent heat exchange between the atmosphere and ocean during boreal winter in both the KER and GSR. The statistical characteristics of the extreme flux events reveal that the average accumulated number of the extreme flux event days, which typically (>85%) last fewer than 3 days, occupies only 20% of the winter period, but the events contribute significantly to the total THF during the entire winter season, explaining more than 80% of the total variance of THF in the regions. The short duration of the extreme flux events suggests that they are associated with synoptic-scale atmospheric variability.

Composite analysis reveals that the extreme flux events are closely related with the winter season CAOs. Event days are characterized by “cold storms” with a pair of anti-cyclone and cyclone on each side of the maximum air-sea heat flux exchange due to the

strong northerlies riding over the sharpest pressure gradient, bringing cold, dry air from the Eurasian/North American continent over the warm oceans. Non-event days are characterized by "warm storms" with opposite anomalous pattern. The extreme flux events in the Pacific differ those in the Atlantic in terms of magnitude, location and orientation. The latter tends to have stronger intensity and shorter duration than the former.

Analyses of the temporal variations of the extreme flux events show significant upward trends during the past 60 years (1948-2008) in both Pacific and Atlantic and two marked decadal shifts occurred around 1970s and 1990s. The linear trend and the decadal shifts are also present in the variability of the mid-latitude storm tracks. SVD analyses show that the extreme flux events in the KER/GSR are closely related to the PDO/EAP in the North Pacific/Atlantic, respectively. Lag composite analyses suggest that both the PDO and EAP are linked to the evolution of CAOs. When extreme flux events occur in the KER/GSR, the associated storms form in the upstream of the PDO and EAP and then propagate eastward, eventually evolving into patterns similar to SLP anomalies associated with the PDO and EAP. Indeed, the anomalous SLP patterns during the positive phase of the PDO and EAP can be practically reconstructed using only the SLP anomalies at the late stage of the CAO storms reveals, suggesting that the PDO and EAP may be largely attributed to the rectified effects of the synoptic winter storms accompanied with the extreme flux events. This explanation is consistent with the modeling results represented by Feldstein (2003), Benedict (2004) and Rivere and Orlanski (2007). Composites of upper troposphere geopotential height anomalies

indicate that the storms associated with the extreme flux events tend to propagate southeastward compared to nonevent-day storms, consistent with the negative SLP anomalies corresponding to positive PDO/EAP phase. Since the southward shift of storm tracks has also been suggested to be related with Pacific and Atlantic-Euro blocking activities (e.g., Croci-Maspoli et al., 2007), it is possible that extreme flux events in the KER/GSR, blockings activities and PDO/EAP in the North Pacific/Atlantic may be interrelated. Future studies are needed to investigate this potential linkage.

Finally, lag regression analyses of SST anomalies and extreme flux event index show some evidence of a positive SST influence on the occurrence of extreme flux events in the KER, but not in the GSE. Instead, the analyses present an unequivocal evidence for atmosphere-forcing-ocean in the central basin of the North Pacific and Atlantic when the extreme flux events lead SST. However, the lack of a strong evidence of a positive SST influence on extreme heat flux variability in the KER and GSR does not mean an absence of strong atmosphere-ocean interactions in the regions. It is possible that interactions between turbulent heat fluxes and SST take place at frontal-and meso-scales (e.g., Chelton et al. 2004) that are not well represented by the data sets and analysis techniques used in this study. Future studies are needed to explore this possibility.

Based on the results presented in this study, we hypothesize that extreme winter storm activities in the KER and GSR are crucial in understanding the PDO in the north Pacific and the EAP in the north Atlantic. To a large extent, the PDO and EAP can be explained as a rectified effect of the extreme storm variability in the KER and GSR and

the north Pacific and Atlantic storm track variability can also be directly linked to the extreme storm variability in the KER and GSR. As such, it is through the extreme heat flux variability in the KER and GSR that SST effects on the PDO and EAP are exerted. Future studies need to focus on frontal- and meso-scale air-sea interactions along the Kuroshio and Gulf Stream Extension.

# CHAPTER III

# EFFECTS OF MESO-SCALE OCEANIC EDDIES ON NORTH PACIFIC STORM TRACK

## 3.1 Introduction

It has been recognized for decades that for large-scale air-sea interactions in the midlatitudes, the atmosphere is forcing the ocean. Negative correlations between SST and surface wind are commonly found in the observations when ocean gyres respond to basin-scale changes in wind stress curl (Mantua et al. 1997; Okumura et al. 2001). The negative correlation has been interpreted as an atmosphere one-way forcing: the oceans respond passively to turbulent heat flux changes induced by surface wind anomalies (Xie 2004; Chelton et al. 2010). In particular, high surface wind speed tends to cool the ocean due to enhanced sensible and latent heat flux release from the ocean to the atmosphere (Alexander et al. 2002). Besides, the resultant enhancement in the entrainment into the oceanic mixed layer also has a cooling effect on the ocean surface (Alexander et al. 2002; Small et al 2008).

Recent high-resolution satellite observations reveal coherent variations of meo-scale and frontal-scale (10-1000km) SST and surface wind in major oceanic frontal zones, such as the Kuroshio, Gulf Stream and Antarctic Circumpolar Current (ACC) fronts (Chelton et al. 2004; Xie 2004). By spatial filtering satellite SST and surface wind stress/speed, a positive correlation has been revealed between meso-scale SST and surface wind, indicating that the ocean may be forcing the atmosphere (O'Neill et al.

2005; Chelton and Xie 2010). Furthermore, the occurrence of extreme high wind was found to collocate with warm SST (Sampe and Xie 2007). Physical mechanisms of the meso-scale air-sea interaction were reviewed by Small et al. (2008). Changes of meso-scale oceanic eddies have found to have an impact on atmospheric turbulent heat fluxes, wind stress, surface stability and planetary boundary layer height (PBLH) (Sweet et al. 1981; Wai and Stage 1989; Kwon et al. 1998; Park et al. 2006). Warm oceanic eddies tend to increase surface air-sea temperature difference and moisture supply, cause changes in sensible and latent heat fluxes as well as enhanced vertical mixing and destabilize the boundary layer. Thus, a deeper PBLH is often observed along the warm side of oceanic fronts (Sweet et al. 1981; Kwon et al. 1998). The unstable and deeper PBL over the warm SST enhances the momentum transfer from the upper level to the surface, and thus increases the surface wind speed (Wallace et al. 1989; Chelton et al. 2004; Booth et al. 2010). Another explanation of the coherence between high SST and high wind speed is the pressure gradient adjustment mechanism (Lindzen and Nigam 1987; Wai and Stage 1989; Cronin et al. 2003). A secondary circulation across the fronts develops due to the low/high pressure anomalies induced by underlying warm/cold SST anomalies, leading to in phase change between surface wind anomalies and SST (Warner 1990; Small et al. 2003).

Besides the response within the atmospheric planetary boundary layer (PBL), a more important question is whether there is a deep response in the troposphere to meso-scale oceanic eddies. In frontal regions, the acceleration of wind over the warm SST and deceleration of wind over cold SST can lead to wind convergence/divergence (Chelton

et al. 2004). The convergence and divergence of the winds may induce vertical motion and further affect the upper level of the atmosphere (Xie 2004). A recent paper by Frenger et al. (2013) showed that the oceanic eddies can have an impact on precipitation in upper troposphere. Warm oceanic eddies are accompanied by increased moisture supply, enhanced turbulent mixing and unstable atmospheric boundary layer, in favor of intensified local convection and positive rainfall anomalies. Several other papers also indicated a high rainfall band along the KE and GS (Minobe et al. 2008; Xu et al. 2011), suggesting a potential deep troposphere response to oceanic fronts. Since meso-scale oceanic eddies are rich in frontal regions, it is possible that the deep response is related to meso-scale oceanic eddies as well.

In the WBC regions, frontal-and meso-scale atmosphere-ocean interactions are highly complex partially because of frequently passing-through midlatitude storm systems in the regions (Nonaka and Xie 2003; White and Annis 2003). The genesis of midlatitude storm tracks is determined by baroclinic instability. An abundance of work exists on the genesis and development of midlatitude storm tracks. Classic theory on midlatitude frontal genesis is formulated on the basis of baroclinic instability theory in an adiabatic atmosphere with strong temperature gradients (Charney 1947; Eady 1949; Phillips 1954; Lindzen and Farrell 1980; Hoskins et al. 1985). According to the thermal wind relation, a sharp temperature gradient gives rise to a strong vertical wind shear, which in turn becomes unstable, allowing eddies to grow exponentially by extracting energy from the mean available potential energy of the background mean flow. Interpreting from a potential vorticity (PV) framework (Petterssen and Smebye 1971;

Hoskins et al. 1985), a positive feedback between upper level PV anomalies and low level baroclinic instability is crucial to cyclogenesis along storm tracks. Positive PV anomalies associated with cyclones in the upper level can lead to positive surface PV anomalies in the presence of surface warm temperature anomalies. The surface temperature anomalies can in turn feedback positively onto the upper level cyclones, and thus causing the disturbance to grow.

Hoskins et al. (1985) also briefly discussed the potential effect of diabatic heating by latent heat flux release in the PV framework and pointed out that the latent heat release may act as another important source of positive feedbacks between PV. Since then a large body of work has been devoted to understanding of the role of diabatic effect in cyclogenesis. The so-called moist baroclinic stability theory has been developed to stress the importance of diabatic heating and its influence on cyclogenesis (Emanuel et al. 1987; Snyder and Lindzen 1991; Davis et al. 1993; Balasubramanian and Yau 1994; Mahoney and Lackmann 2007). A review paper on how latent heat release can influence extratropical cyclogenesis is provided by Ahmadi-Givi (2002). Unlike the adiabatic and frictionless situation, PV is not conserved in diabatic heating case. The presence of diabatic heating tends to destabilize the air column, increase the vertical mixing and introduce PV anomalies into the system (Ahmadi-Givi 2002; Lapeyre and Held 2004). Compared to the adiabatic case, the PV anomalies generated by diabatic heating further amplify the surface cyclones and allow for a more rapid growth of synoptic storms (Emanuel et al. 1987; Montgomery and Farrell 1991; Balasubramanian and Yau 1994). In the case of a weak diabatic heating, the baroclinc instability can still

dominate and diabatic effects enhance the positive feedback between upper and lower PVs, modifying the growth rate and structure of the baroclinically unstable waves (Davis and Emanuel 1991; Davis et al. 1993,1996; Fehlmann and Davis 1999). However, in the case of strong diabatic heating, the classical baroclinic instability theory becomes less relevant, especially when surface temperature gradients are weak as studied by Craig and Cho (1988) and Parker and Thorpe (1995).

According to baroclinic instability theories, the growth rate of storm tracks can be modified by the underlying SST gradient related with oceanic fronts and the supply of moisture. Using a high-resolution atmospheric model, Xie et al. (2002) found that storm growth rate was reduced in simulations forced with smoothed SST. They attributed the reduction of storm growth to a combined effect of weaker SST gradient and latent heat flux release. Another study by Lambert et al. (2012) found a significant increase in storm growth rate at the initial stage of idealized two-layer atmosphere model simulations with the introduction of latent heat release in comparison to "dry" simulations. They further noted that in the later stage of the simulations after the storms were fully developed, a poleward shift of the jet stream was found in the moisture case due to the wave breaking. A recent study by Willison et al. (2013) revealed enhanced cyclogenesis in a 20 km WRF model that resolves mesoscale latent heat release and precipitation process compared with a 120 km WRF. These studies are consistent with the moist baroclinic instability theory, indicating an amplification effect of diabatic heating on the growth of baroclinic instability. However, to what extent that the diabatic heating and storm genesis may be influenced by meso-scale oceanic eddies has not been explored.

The previous studies indicate that meso-scale oceanic eddies may influence both atmospheric boundary and deep atmospheric responses. A potential influence of oceanic eddies on the storm genesis in the WBC regions may be achieved via moist baroclinic instability. The altered storm genesis may further modify the mean flow, generating a remote influence on weather patterns downstream. In this chapter, we will explore the possible effect of oceanic eddies on the midlatitude atmosphere by conducting an ensemble of high-resolution regional atmospheric model (Weather Research Forecasting, WRF) simulations. Some of the scientific questions that we intend to address in this chapter include: (1) Can meso-scale oceanic eddies exert a measureable influence on the atmosphere? (2) Can storm characteristics along the Kuroshio Extension region be modified by meso-scale oceanic eddies? (3) Will there be a downstream response of the storm track in the eastern Pacific basin? If so, how will it be related to mean flow changes?

This chapter is organized as follows. Section 2 gives an introduction of the datasets and WRF model used in this study, as well as a brief description of model setup and experiment design. Section 3 validates WRF simulations against observations. Local atmospheric response to meso-scale oceanic eddies, including local precipitation, surface heat fluxes, PBLH and storm growth characteristics, is discussed in Section 4. Remote responses, including storm track and mean flow changes in the eastern Pacific basin, are discussed in Section 5. Finally, a summary of major findings is given in Section 6.

## 3.2 Observation Data, Model Configuration and Experiment Design

### *3.2.1 Observation Data*

Mircrowave InfraRed Optimal Interpolated (MW-IR, 2002-present) daily SST provided by Remote Sensing System (RSS) with a horizontal resolution of 0.09° (about 9km) is used as the low boundary forcing in WRF simulations. The high-resolution SST is necessary to resolve meso-scale oceanic eddies in the KE region. The initial and lateral boundary conditions for WRF simulations are interpolated from 6 hourly NCEP2 reanalysis data (NCEP-DOE Reanalysis 2, 1979-present, Kanamitsu et al. 2002). The NCEP2 data has 17 vertical pressure levels and variables at these pressure levels have a horizontal resolution of 2.5°. The two dimensional surface flux variables provided by the NCEP2 have a horizontal resolution of about 1.875° (T192 grid).

In addition to the above data sets used to force the model, daily TRMM (Tropical Rainfall Measuring Mission, 1998-2011) rainfall with a 0.25° horizontal resolution is used to validate the model simulations. TRMM Rainfall before 2000 has a discontinuity at the northern boundary due to the combination of different satellites and is discarded. These satellite rainfall measurements are available within the latitude belt between 45°S and 45°N. 6 hourly 10 m high-resolution (0.25°) wind speed derived from CCMP (Cross-Calibrated Multi-Platform, Atlas et al. 2011) and weekly sea surface height (SSH, 0.25°) from AVISO (1993-2011, Ducet and Traon 2000) are used to analyze oceanic eddy activity. Finally, meridional wind velocity derived from 6 houlry ERA-Interim data from ECMWF (European Centre for Medium-Range Weather Forecasts, Berrisford et al. 2009) is used to calculate the Pacific storm track. Observationally

derived daily OAflux dataset (Yu et al. 2008) is used to derive THF index in the KER. A detailed description of the OAflux dataset has been given in Chapter II.

*3.2.2 Model Description and Configuration*

The Weather Research and Forecasting (WRF) Model developed by NCAR is designed to serve both weather forecasting and atmospheric research needs and has been used in variety of regional climate studies (Leung et al. 2006). For this study, the computational domain covers the entire North Pacific Ocean from 3.6°N to 66°N, 99°E to 270°E as shown in Figure 17 (the outer domain). The horizontal grid is set at 27km based on a Mercator projection. The atmosphere is divided into 30 vertical levels. The model configuration includes the Lin et al's Scheme for microphysics (Lin et al. 1983), RRTMG and Goddard scheme for longwave and shortwave radiation (Chou and Suarez 1994; Mlawer et al. 1997), a Noah land surface scheme, YSU scheme for planetary boundary layer (Hong et al. 2006), a horizontal, first-order closure Smagorinsky scheme for calculating eddy coefficient. The cumulus parameterization is the Kain-Fritsch (KF)

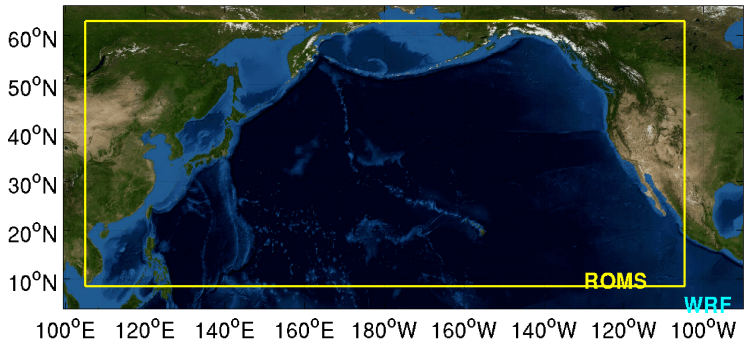


Figure 17. Model domain: the outer frame outlines the WRF computational region (27km an 9km) and the inner frame outlines the ROMS computational region (9km).

scheme (Kain 2004). Snow cover effect is not included in the model configuration. The 6 hourly low-boundary SST forcing from January 1, 2007 to March 31, 2008 was interpolated from the high-resolution (0.09°) MW-IR daily SST. The initial and lateral boundary conditions for the same period were derived from the 6 hourly NCEP2 reanalysis data.

*3.2.3 Experiment Design*

As previous studies indicate that intense air-sea interactions in midlatitudes occur at frontal- and meso-scales, we design two ensembles of WRF experiments specifically to test the effect of SST variability associated with meso-scale oceanic eddies on the atmosphere. The two ensembles of runs only differ in SST forcing field, one of which is forced with the high-resolution observed SST, while the other is forced with a smoothed SST with meso-scale eddies removed. A snapshot of the observed and smoothed SST forcing used in two simulations is shown in Figure 18. In the control simulation (CTRL), the SST forcing applied as the low boundary forcing in WRF was directly interpolated from the satellite-derived MW-IR SST (Figure 18, top left). An ensemble of 5 runs was conducted with the same SST forcing and lateral boundary conditions, but altered initial conditions to take into consideration of the effect of atmospheric internal variability. The initial condition of the five ensemble number was taken from the NCEP2 reanalysis at the same day but in different years, i.e. October 1, 2006, 2007, 2008, 2009, 2010, respectively. All five simulations were integrated for 6 months during the boreal winter season from October 1, 2007 to March 31, 2008 (ONDJFM).

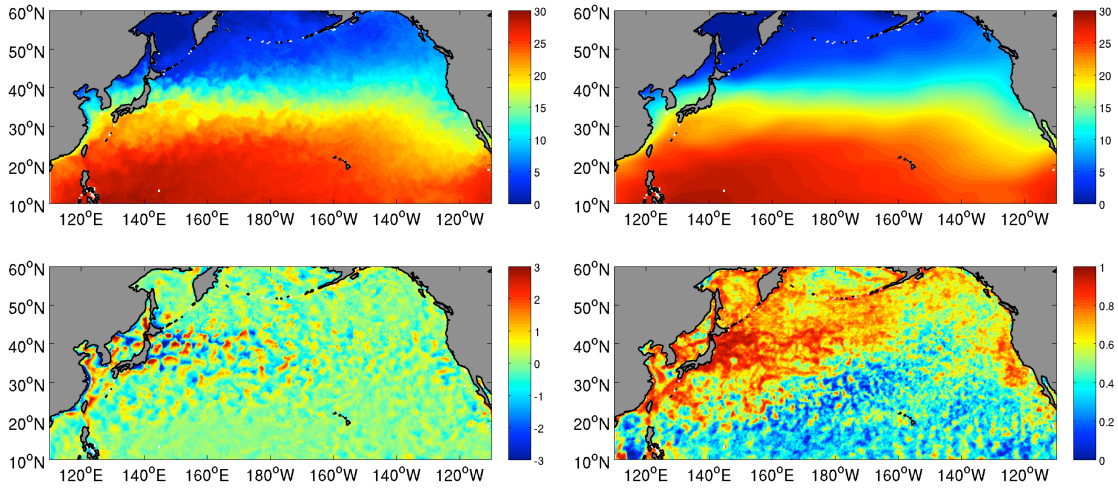


Figure 18. SST (shaded, °C) on 01/01/2008 derived from MW-IR satellite data and prescribed in the CTRL (top left) and MEFS (top right) in 27km WRF simulations. In MEFS, spatial Loess filter with a half-width of 15°x5° was applied. Bottom left, SST difference between CTRL and MEFS. Bottom right, contribution (percentage) to the observed MW-IR SST variability from the meso-scale SST variability in 2007/8 NDJFM.

To isolate meso-scale SST variability, we applied a spatial high-pass filter to the MW-IR SST. Following many previous studies (Chelton et al. 2004, Maloney and Chelton 2006; Bryan et al. 2010), we used a Loess filter of a half-width of 15° in longitude and 5° in latitude (same as in Chelton et al. 2004) and then used the low-pass filtered SST as the low boundary forcing to WRF (Figure 18, top right). As shown in Figure 18 (bottom left), the most energetic meso-scale eddies removed from the MW-IR SST are confined along the KER where we expect to see the most intense air-sea coupling. To estimate the contribution from the meso-scale SST variability to the observed MW-IR SST variability, we regressed the MW-IR SST onto the meso-scale SST. The result shows that in the KER, more than 80% of the MW-IR SST variance can

be explained by the meso-scale SST variability (Figure 18, bottom right). It means that removing the meso-scale SST variability causes a significant reduction of SST forcing variance in the KER. More importantly, it is at this meso-scales that we expect to see a significant influence of the SST on the overlying atmosphere. We refer the ensemble of five runs forced with the filtered SST as Mesoscale-Eddy-Filtered Simulation (MEFS). In MEFS, all settings are identical to CTRL except the SST forcing.

### 3.3 Model Validation

The performance of WRF to simulate the winter mean atmospheric circulation and midlatitude storm tracks is validated against observations and reanalysis data during the winter of 2007/8. Considering the spin up time of the model simulation, validation analyses were performed using the last 5 months (NDJFM) of the WRF simulation with October 1, 2007 initial condition. Figure 19 shows a comparison between the winter

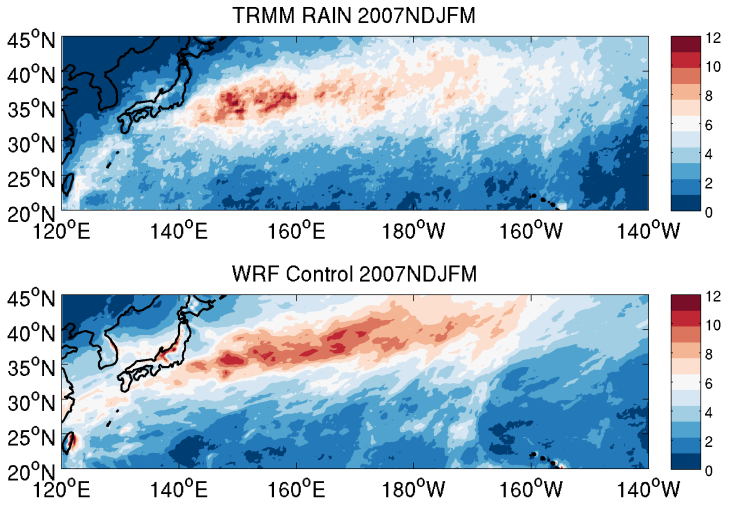


Figure 19. 2007/8 winter season (NDJFM) mean rainfall (mm/d) derived from TRMM (top) and simulated in 27km WRF CTRL (bottom).

season (NDJFM) mean rainfall in CTRL and TRMM rainfall during the same period. In the observation, a high rainfall band collocates with the KER in the North Pacific (Figure 19, top) and is associated with a strong surface convergence along the fronts (Minobe et al. 2008). On the other hand, high oceanic eddy activity is also located in the same region (Figure 18, bottom left), raising the possibility that some of high rainfall events in the region may be caused by the strong meso-scale oceanic eddies. The model well reproduced the overall pattern and the position of the high rainfall band except that the rainfall rate is overestimated by the model simulation (Figure 19, bottom). In particular, the high rainfall in the KER is well reproduced. However, the simulated high rainfall band tends to extend too much eastward along the downstream of the KE, giving rise to an overestimate of the rainfall in the eastern basin. The overestimation of the simulated rainfall in the downstream of the KE is about 2-4 mm/day on average (25-50% of the observed mean rainfall) and is likely to be attributed to the KF convection scheme used in the model.

A comparison between simulated and ECMWF low and upper level storm tracks is illustrated in Figure 20. The storm track is represented using the standard deviation of 2-8-day band-pass filtered meridional wind component (<v'v'>). The maximum of 850hpa storm track extends northeastward from 160°E to 140°W, downstream and north of the KER (Figure 20, top left). The strong baroclinic instability induced by the sharp temperature gradient along the Kuroshio front is responsible for the generation of the storm track and upon its generation the storm track tends to follow a southwest-northeast path (Chang et al. 2002; Nakamura et al. 2008). The upper level storm track at 300hpa is

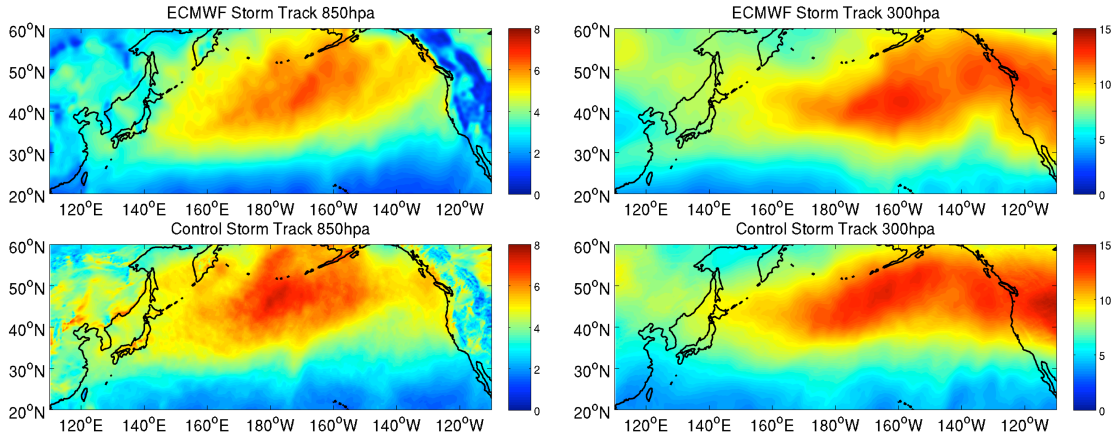


Figure 20. 2007/8 850hpa (left) and 300hpa (right) winter season (NDJFM) storm track derived from ECMWF (top) and simulated in 27km WRF CTRL (bottom). The storm track is calculated by the standard deviation of 2-8-day band-pass filtered meridional wind component <v'v'>.

much stronger and develops further downstream and has maximum in the eastern North Pacific and North American continent (Figure 20, top right). The simulated low and upper level storm tracks at 850hpa and 300hpa in CTRL agree very well with those derived from the ECMWF analysis, displaying similar general distribution and maximum axis. Simulated storm track strength is slightly stronger than that in the reanalysis.

A defining feature of the frontal-scale air-sea interaction along the KER is that meso-scale high (low) wind speed tends to co-locate with warm (cold) meso-scale SST (Chelton et al. 2004). The next assessment of the model performance is to see whether this meso-scale wind-SST relationship can be reproduced by the model simulation. To carry out this assessment, we spatially filter the 10 m satellite-derived CCMP wind speed and MW-IR SST using the Loess filter. Figure 21 (top left) shows 2007/8 winter

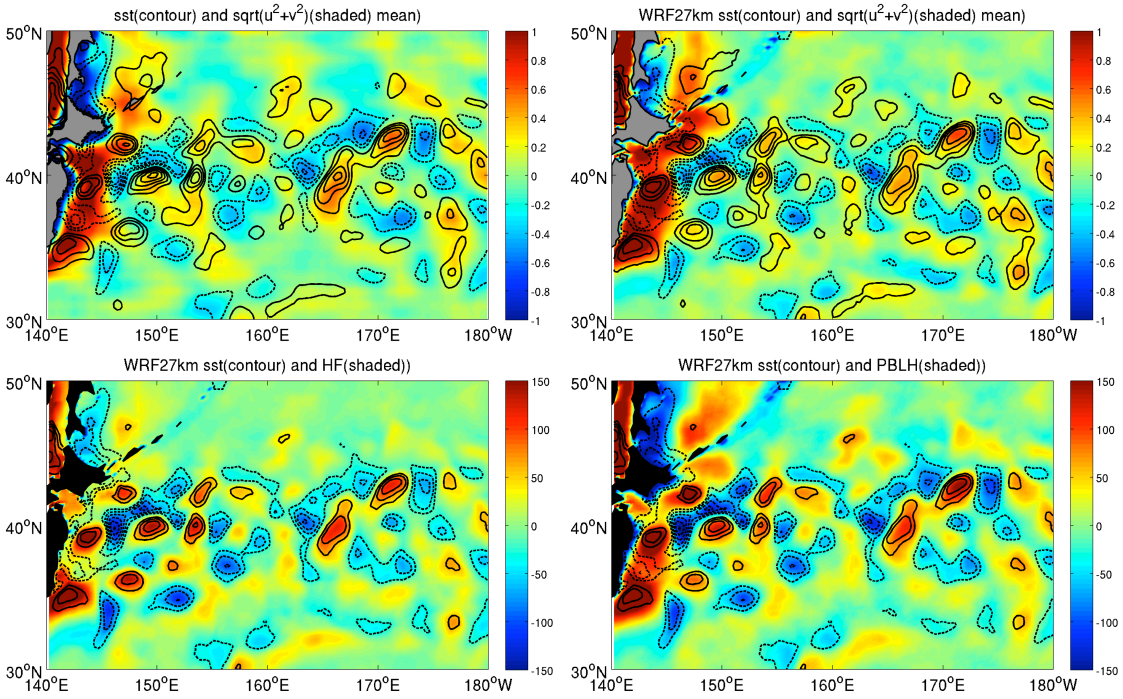


Figure 21. Top left, 2007/8 winter season mean (NDJFM) high-pass filtered SST (contour, °C) and 10m wind speed (color shaded, m/s) derived from MW-IR and CCMP satellite observations. Top right, same as top left, but derived from ensemble mean of 27km WRF CTRL simulations. Bottom left (right), same as top right, but for high-pass filtered THF (PBLH) and SST simulated in 27km WRF CTRL. Positive SST is plotted in solid contours and negative SST in dashed contours.

mean (NDJFM) meso-scale (filtered) SST and surface wind speeds. It is evident that warm (cold) SST anomalies correspond to high (low) surface wind anomalies, consistent with the positive correlation revealed in previous observations (Chelton et al. 2004). Same analysis was then applied to SST and 10 m wind speed derived from the WRF simulation. The results reveal a remarkably consistent picture (Figure 21, top right). In fact, the simulated meso-scale SST-wind pattern is nearly identical to the observed pattern: not only the covariability of meso-scale SST and surface wind is reproduced by

the model, but also the amplitude of high and low wind speed in the model agrees very well with the observation.

Furthermore, similar meso-scale atmospheric responses in the model simulation are observed in surface THF and atmospheric PBLH. Figure 21 (bottom left and right) shows that warm (cold) oceanic SST anomalies coincide with high (low) THF and thick (shallow) PBLH anomalies, consistent with previous work (Sweet et al. 1981; Kwon et al. 1998; O'Neill et al. 2005). These results indicate that warm oceanic eddies tend to enhance air-sea temperature contrast, providing more moisture supply to the atmosphere from the underlying ocean and leading to a strengthened THF. The deepening of PBLH over warm SST anomalies is suggestive of the momentum mixing mechanism where the intensified turbulent processes over warm SST regions cause stronger vertical mixing that enhances the downward momentum transfer from the upper troposphere to the surface, leading to an increase in surface wind speed over warm SST (Wallace et al. 1989; Booth et al. 2010). All these results demonstrate that the WRF simulation successfully captures the air-sea interactions between meso-scale surface winds and SST along the KER and the model is capable of simulating dynamical processes governing meso-scale atmosphere-ocean interactions..

In summary, the stand-alone WRF simulations with 27 km horizontal resolution demonstrate a high fidelity in simulating precipitation and storm tracks along the KER. It also demonstrates a remarkable skill in reproducing observed meso-scale wind-SST relationships over the KER, indicating its capability of capturing frontal-and meso-scale air-sea coupled dynamics in the region. In the next section, we will examine the effect of

meso-scale SST variability on the overlying atmosphere by contrasting CTRL and MERS.

### 3.4 Influences of Oceanic Eddies on the Atmosphere

This section is devoted to the comparison between CTRL and MEFS in an attempt to address the question of how important meso-scale oceanic eddies along the KER are affecting the atmosphere. Analyses of local meos-scale response, including THF, surface winds and PBLH within the atmospheric boundary layer along the KER will be presented first and then remote response of rainfall and storm tracks in the upper troposphere will be analyzed. Finally, some observational evidence will be presented that supports the modeling results.

#### *3.4.1 Local Meos-scale Response*

Figure 22 (a, b, c, d) shows the ensemble average of meso-scale (high-pass filtered) SST variance, surface THF variance, PBLH variance and 10 m wind speed variance in NDJFM, respectively, derived from CTRL. As expected, the largest variability of meso-scale SST occurs in the KER where oceanic eddies are most active and it was shown in the previous section that more than 80% winter season SST variability in the KER can be explained by meso-scale eddy activity (Figure 18, bottom right). At the surface, the meso-scale (high-pass filtered) THF variability is closely related to the meso-scale SST variability and is also strongest in the KER. The variance of meso-scale (high-pass filtered) surface wind and PBLH also have their maximum along the KER, but they extend further eastward and have a broader pattern compared to that of SST and THF. The co-variability of meso-scale SST, THF, 10m wind and PBLH along the KER

indicates the potential influence of meso-scale oceanic eddies and is consistent with previous studies (Chelton et al. 2004; O'Neill et al. 2005; Small et al. 2008).

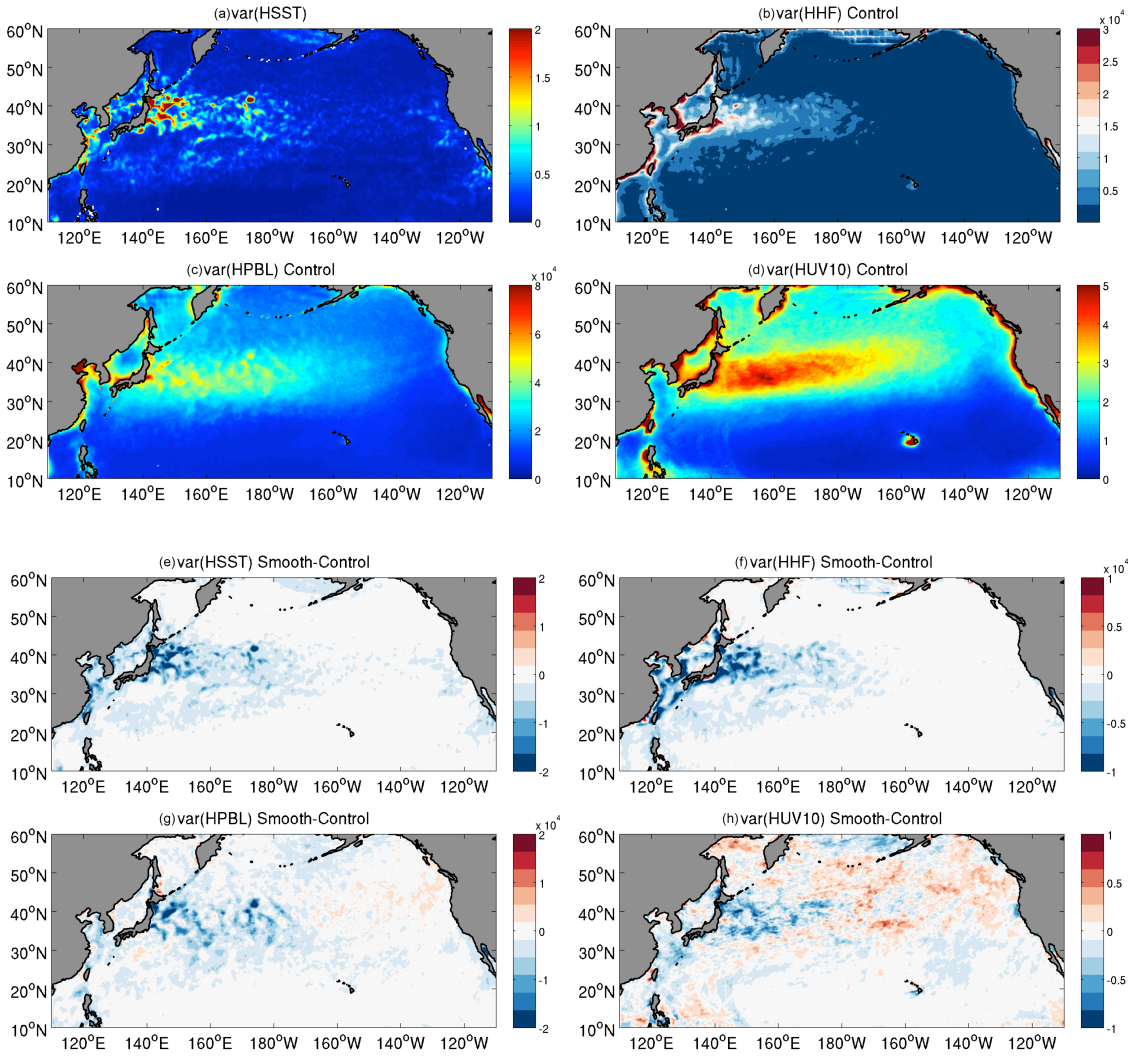


Figure 22. Ensemble mean NDJFM variance of high-pass filtered SST (a), THF (b), PBLH (c) and 10m wind speed (d) simulated in 27km WRF CTRL. Difference of the variance of high-pass filtered SST (e), THF (f), PBLH (g) and10m wind speed (h) between MEFS and CTRL.

The difference of meso-scale variability (SST, THF, PBLH, 10m wind) between MEFS and CTRL is shown in Figure 22 (e, f, g, h). Overall, there is a well-defined decrease of meso-scale variability over the KER in the MEFS, as expected, after removing the oceanic eddies. The decrease of meso-scale THF variance closely resembles that of meso-scale SST and is more than 30% along the Kuroshio and in the KER. The change of surface wind and PBL variance are not as large as that in THF variance, but still significant with a 20%-25% decrease in variance over the KER. Interestingly, there is a modest increase in variance of these fields in the downstream of the KER.

To quantify variance reduction at various spatial scales due to the removing of meso-scale oceanic eddies, two dimensional spectrum analysis is applied to the daily SST, THF, 10 m wind and PBLH in the KER (40°x20° box) in each ensemble member for CTRL and MEFS, respectively. The resultant power spectrum density is then integrated along a given wavenumber and averaged for the entire winter season to obtained a one-dimension energy spectrum (not shown here). The difference of the ensemble mean energy spectrum between MEFS and CTRL is illustrated in Figure 23. The largest resolvable wavelength is 2000 km in the chosen analysis domain. Clearly, the variance reduction decreases as the wavelength increases. The most significant decrease occurs at scales smaller than 1000 km while the energy at large-scales (larger than 1000 km) does not show significant change. The 1000 km meso-scale cutoff is consistent with the Loess filter applied in the analysis (a half wavelength of 5° in latitude). Below 800 km, about 80% of the meso-scale SST variation is removed in

MEFS. The corresponding THF decrease at the same wavelength range is about 30%. The variance reduction in PBLH due to the meso-scale SST change is about 10% below 400 km, while the change in 10 m wind variance is not significant. Note that there is a slightly increase in 10 m wind variance for wavelength >1000km, hinding that large-scale atmospheric variation may be affected by removing meso-scale ocean eddies.

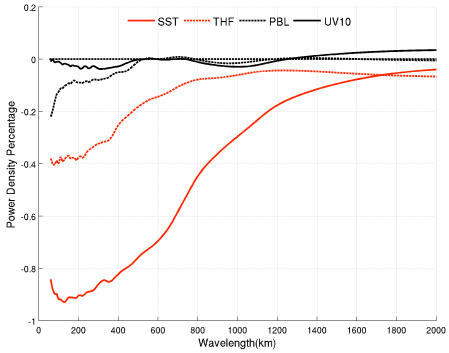


Figure 23. Difference of ensemble mean energy spectrum for SST (solid red), THF (dash red), PBLH (dash black), 10m wind speed (solid black), between MEFS and CTRL in 27km WRF simulations.

In summary, these analyses indicate that removing meso-scale oceanic eddies leads to more than 30% decrease in meso-scale THF variance and 10% decrease in meso-scale PBLH variance.

*3.4.2 Rainfall and Storm track Response*

Besides the decrease in meso-scale variability of surface THF, surface wind and PBLH over the KER, comparison between MERS and CTRL also reveals significant

changes in large-scale atmospheric circulation pattern and deeper response in the upper troposphere.

Figure 24 (top) shows the winter mean rainfall difference between MEFS and CTRL. A two-sided non-parameterization test (Wilcoxon rank sum test, Wilcoxon 1945) was applied and difference significant at 95% confidence level was highlighted. In the following analyses, significant test was performed to all the other variables when calculating the difference between MEFS and CTRL using the same method. Along the

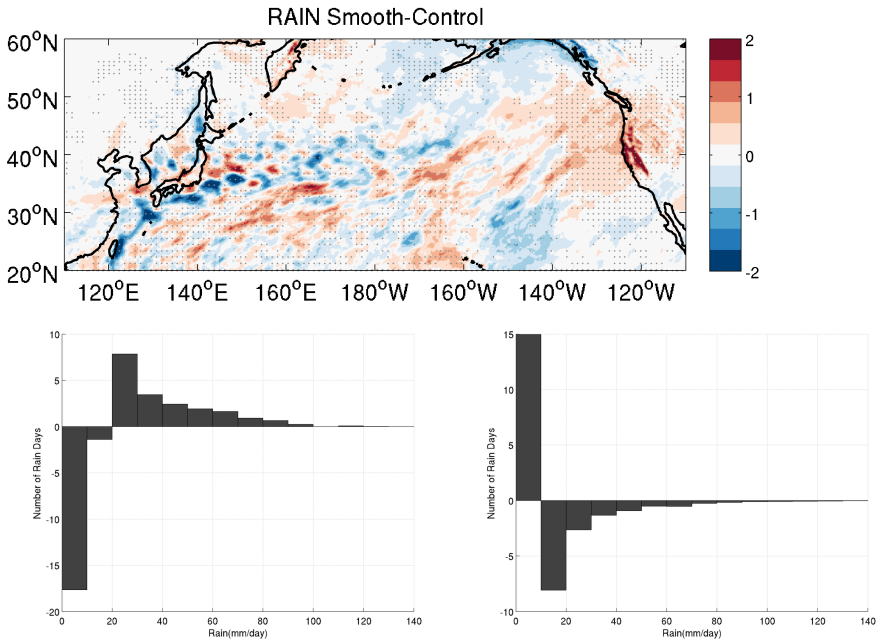


Figure 24. Difference of ensemble average winter season (NDJFM) mean total rainfall (mm/d) between MEFS and CTRL in 27km WRF simulations (top). Rainfall difference significant at 95% confidence level using a two-sided Wilcoxon rank sum test is shaded by gray dots. Difference of rainfall PDF in KER (bottom left) and USWC (bottom right) between CTRL and MEFS. The rainfall PDF is derived by counting the number of rainy days for different rain rate ranges at each grid point and averaged in the chosen regions.

KER, there is a significant decrease in the mean rainfall due to the absence of oceanic eddies. The decreased rainfall mainly occurs along the upper branch of the Kuroshio, consistent with SST decrease in the MEFS. The decrease in winter-mean rainfall caused by the absence of oceanic eddies amounts to about 20-25% compared to the total winter mean rainfall in the model (Figure 19, bottom). Another striking difference is the rainfall increase over the eastern North Pacific basin, particularly along the U. S. west coast (USWC). The increase appears to be intensified by orographic effect along the coast. A further separation of simulated rainfall into convective rain and large-scale rain demonstrates that the decrease of rainfall in the KER is mainly due to the change of convective rainfall, while the rainfall increase along USWC is due to large-scale non-convective rainfall (Figure 25). Convection can be triggered when underlying SST is relative warm and sufficient moisture is provided, and thus is strongest along the KER in the midlatitude of North Pacific. The rainfall decrease in the KER is likely caused by the fact that the removal of meso-scale warm oceanic eddies tends to increase the stability, inhabit the development of convection and reduce latent heat release. Large-scale rainfall usually occurs along cold fronts accompanying synoptic weather patterns. The rainfall is not restricted in the KER and can have broad and downstream structure far away. The increase of rainfall along USWC is thus more likely to be related with increases in synoptic storm activities. The change of oceanic meso-scale eddy activity in the KER somehow changes the downstream storm tracks, leading to an increase of rainfall in the eastern North Pacific. More analysis and discussion on this issue will be given later.

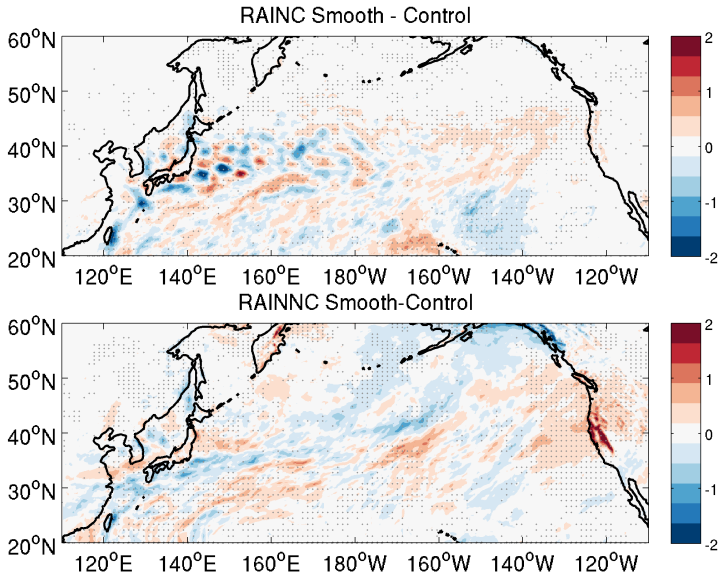


Figure 25. Difference of ensemble average winter season (NDJFM) mean convective (top) and non-convective (bottom) rainfall (mm/d) between MEFS and CTRL in 27km WRF simulations. Again, rainfall difference significant at 95% confidence level using a two-sided Wilcoxon rank sum test is shaded by gray dots. The sum of convective rainfall and non-convective rainfall equals the total rainfall.

To further examine changes in rainfall probability density function (PDF) distribution, we chose a 5°x5° box in the KER (USWC) where the most significant decrease (increase) of rainfall is observed. The numbers of rainfall days were counted for different rain rate ranges at each grid point for all CTRL and MEFS runs. The rainfall PDF is then obtained by averaging the counted rainy days for each of the chosen regions. Figure 24 (bottom left) shows the difference of PDF between CTRL and MEFS in the KER. In CTRL when meso-scale oceanic eddies are present, there are more high rainfall (>20mm/day) days and less low rainfall (<20mm/day) days compared to MEFS. In other words, the rainfall PDF tends to shift toward higher rainfall rate in CTRL than in MEFS. In contrast, rainfall PDF along the USWC changes in the opposite direction (bottom

right). The presence of oceanic eddies in CTRL causes an increase in low rainfall (<10mm/day) days and decrease in high rainfall (>10mm/day) days compared to MEFS, resulting a shift of rainfall PDF towards lower rainfall rate. These rainfall PDF shifts were found in each ensemble member of the two experiments, and thus the results are robust statistically. To conclude, the model simulations show that the presence of ocean eddies produces more intense rainfall events in the KER, while producing less intense rainfall events along the USWC.

The KER is known as an important region for midlatitude cyclogenesis in the North Pacific, rising the possibility that meos-scale oceanic eddies in this region may have an influence on genesis and development of storm systems. To explore this possibility, we examined and compared the response of low-level storm tracks in the KER in CTRL and MEFS. To do so, we first selected storm days using the area-averaged THF threshold (HF80) as described in Chapter II. Lag composite was then performed for 2-8 day band-pass filtered v wind at 850 hpa from lag -3 day to lag 3 day with lag 0 centered on the storm days. The composites are normalized using the maximum storm intensity on lag 0 day to clarify growth and decay characteristics of the composite storms. Figure 26 depicts the normalized lag composites of v' from -2 to +2 day in CTRL (left column) and MEFS (right column), respectively. In both experiments, the composite storms, originated from the continent, gradually grow and reach their peaks near lag 0 day when they passing the KER. After passing the KER, storms gradually decay. However, there are important differences between storm growth and decay characteristics between the

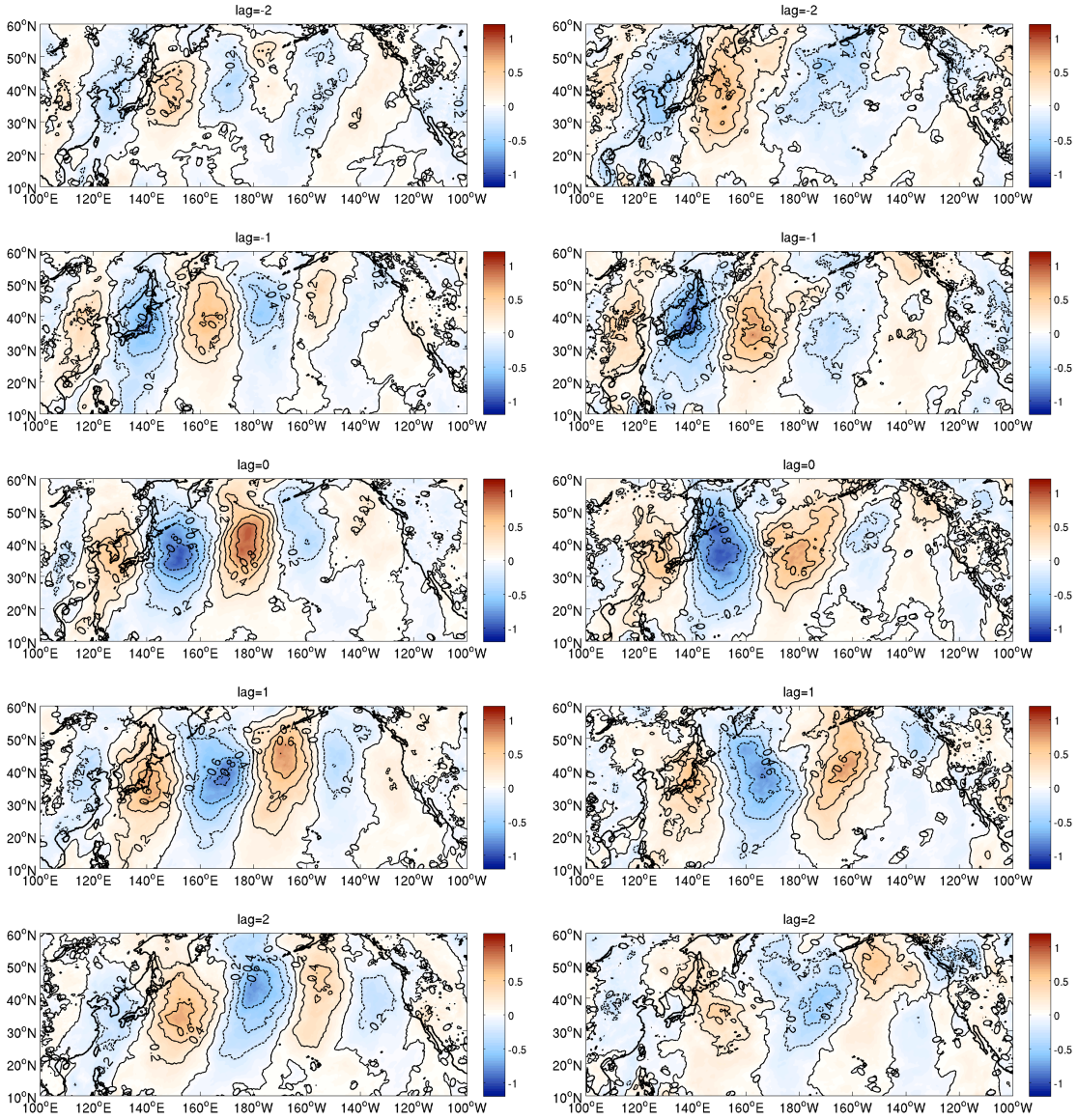


Figure 26. Normalized lag composite (contour and shaded) of 2-8 day band-pass filtered 850hpa meridonal wind (v') on storm days from lag -2 day to lag 2 day for CTRL (left) and MEFS (right) in 27km WRF simulations based on all ensemble members (contour intervals are 0.2). Storm days are picked out by HF80 threshold. The composite is normalized by the storm intensity on lag 0 day.

two experiments. In CTRL, the storms grow more rapidly and decay more gradually, giving rise to a more asymmetric profile in the time evolution of storm amplitude as

shown in Figure 27 (solid). In contrast, the storms in MEFS grow more gradually, but decay more rapidly, giving rise to a relatively symmetric appearance in storm amplitude evolution (Figure 27, dashed). The time evolution of composite storm amplitude shown in Figure 27 is derived by area-averaged v' near the lowest v' value in each composite from lag -3 day to lag 3 composite. At lag -3 day, the amplitude of storms in CTRL is much weaker than that in the MEFS, indicating that the storms in CTRL are less developed at the initial state compared to those in MEFS. At lag 0 day, storms reach their peaks, having normalized amplitude of unity in both experiments. At lag 3 day, the amplitude of composite storms in CTRL is considerably stronger than that in the MEFS, indicating a much slower decay rate of the storms in CTRL. The comparison of storm evolution is highly suggestive that the presence of meso-scale oceanic eddies supports a stronger storm genesis in the KER.

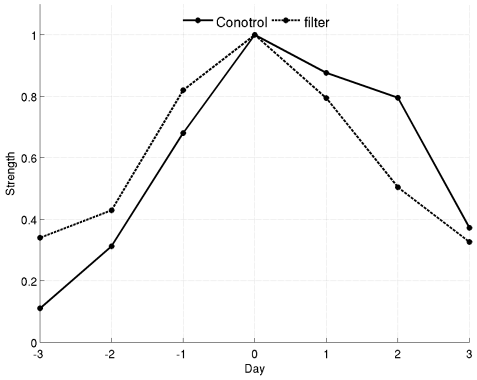


Figure 27. Normalized storm intensity from lag -3 day to lag 3 day in CTRL (solid) and MEFS (dash) in 27km WRF simulations. The storm intensity is derived from the area-averaged v' in a 5°x5° box near the lowest v' value in each storm-day composite as shown in Figure 26.

Another noticeable difference between composite storms in the two experiments is in their spatial scales. Taking lag 1 day composite as an example, there are four clearly identifiable wave ridges and troughs between 130°E to 140°W in CTRL, while there are only three in MEFS, suggesting that storms in CTRL tend to have shorter spatial scales than those in MEFS. There is also an indication of different propagation direction of the composite storms between the two experiments. In CTRL, the storms seem to prefer a northeastward propagation, while in MEFS the storms seems to propagate along a slightly southeastward propagation, although these distinctions are somewhat ambiguous at positive lags. The difference in storm propagation path is related to downstream storm track change, which will be discussed in the next section. We also applied same analysis to 2-8 day band-passed v' at 300 hpa (figures not shown here) and obtained similar results. All these analyses indicate that meso-scale oceanic eddies are able to support stronger storm growth and shorten its spatial scales in the KER.

The effect of meso-scale oceanic eddies on storm growth rate and spatial structure in the KER is consistent with moist baroclinic instability theory. The fact that there is a marked decrease in precipitation along the Kuroshio when meso-scale oceanic eddies are suppressed in MEFS, points to a modification in diabatic heating through latent heat release. According to moist baroclinic instability theory, the presence of latent heat release can reduce the static stability, enhance vertical mixing and generate a new source of PV (Ahmadi-Givi 2002). The diabatically generated PV through latent heat release can enhance the positive feedback between the low and upper level PV, leading to stronger storm growth rate (Emanuel et al. 1987; Davis and Emanuel 1991; Davis et al.

1993). The mutual enhancement between surface storm tracks and upper level storm tracks further allows a deeper influence on the intensification of upper level storm track (Hoskins et al. 1985). The modeling studies also suggest that with moisture effects the most unstable wave tends to have a shorter zonal scale than without moisture effects (Ahmadi-Givi 2002), which is also consistent with the storm composites shown in Figure 26.

To test this theory, a comparison of atmosphere moisture content between the two experiments was made. First, composite of integrated water vapor mixing ratio (Qv) on storm days (again based on the HF80 threshold criteria) was derived for CTRL and MEFS, respectively. Then, difference was taken between MEFS Qv composite and CTRL Qv composite. Figure 28 (left) shows that the removal of meso-scale oceanic eddies causes a 15% decrease of Qv along the KER and an increase along the USWC, consistent with the rainfall change (Figure 24). A further examination of the vertical profile of zonally averaged Qv between 140°E and 180°E shows a clear decrease of Qv in mid-to-lower troposphere in the KER when meso-scale oceanic eddies are suppressed in MEFS (Figure 28, right). The largest decrease is at the surface centered near 40°N, overlying on a rich oceanic eddy area (Figure 18, bottom left). The marked decrease of Qv along the Kuroshio suggests that the influence of oceanic eddies on atmospheric moisture may be nonlinear. While the removal of warm oceanic eddies causes decrease of moisture supply into the atmosphere, the removal of cold oceanic eddies does not lead to an equal increase of moisture, suggesting that cold eddies may be less efficient to influence moisture content in the atmosphere. We performed similar comparison of

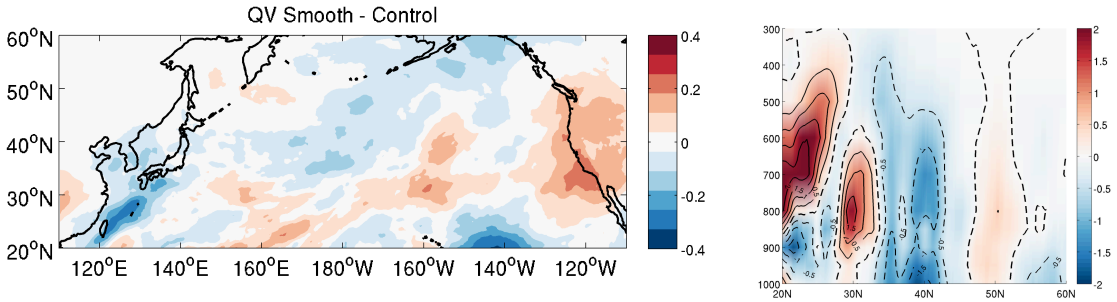


Figure 28. Difference of integrated water vapor mixing ratio Qv ($10^{-2}$ kg/kg) on storm days (again based on the HF80 threshold criteria) between CTRL and MEFS in 27km WRF simulations (left). Right, same as left bur for vertical profile of zonally averaged Qv (contour and shaded, $10^{-4}$ kg/kg) between 140°E and 180°E. Positive values are plotted in solid contours and negative values in dashed contours.

vertical velocity (w) in the two experiments and found a weaker w along the Kuroshio (not shown), consistent with the decease of Qv in MEFS. All these results seem to support the prediction of moist baroclinic instability theory (Emanuel et al. 1987; Craig and Cho 1988). Therefore, we hypothesize that the present of meso-scale oceanic eddies makes atmosphere more unstable, allowing more moisture being pumped into the atmosphere, and more latent heat release. This in turn enhances baroclinic growth of the storm system and produces more intense rainfall events over the KER. The positive feedback between rainfall and storm growth gives rise to intensified storm tracks at both lower and upper level, which are likely generated more precipitation and further accelerate the storm growth rate.

To conclude, a comparison between CTRL and MEFS shows that suppressing SST variability associated with meso-scale ocean eddies along the Kuroshio can result in a statistically significant impact on weather patterns in the North Pacific, including a 20%

reduction (increase) in winter-mean rainfall along the KER (USWC), a reduced storm genesis, an increase in storm zonal scale and a southward shift of storm tracks, as well as a drier troposphere over the KER. The altered storm genesis is likely to be related to moisture effects on baroclinic instability. It is proposed that meso-scale oceanic eddies tend to decrease the static stability in the lower atmosphere and enhances latent heat release, which in turn intensifies baroclinic instability through diabatic heating and supports stronger storm genesis. The mutual enhancement between lower and upper level storm tracks further results in an intensification of upper level storm tracks, which may feedback positively onto rainfall intensity.

*3.4.3 Observational Evidence from Satellite Measurements and Reanalysis*

The striking changes in rainfall pattern and storm genesis in the WRF simulations inspired us to seek further evidences from the observations. To resolve ocean eddies, we first turn to the AVISO SSH dataset that provides an estimate of interannual variability of oceanic eddy activities. First, the Loess filter was applied to winter season (NDJFM) weekly SSH to isolate meso-scale oceanic eddies from large-scale ocean circulation changes. An SSH index was then derived by averaging the winter season meso-scale (high-pass filtered) SSH standard deviation over an area between 135°E-155°E and 30°N-40°N (Figure 29, left). This area coincides maximum meso-scale SST variability as shown in Figure 22. Figure 29 shows the SSH index that agrees well with previous KE path index by Qiu and Chen ( 2005) to represent stable and unstable states of Kuroshio. EOF analysis was then performed to meso-scale (high-pass filtered) SSH anomalies from 1993 to 2010 in the North Pacific. The leading EOF that explains 11.5%

of the total variance and the corresponding PC time series are shown in Figure 29. The first EOF of SSH anomalies picks out the strong oceanic eddy variation in the KER identical to the region in WRF model where meso-scale eddies are filtered. Qiu and Chen (2005) show that the change of meso-scale oceanic eddies is closely related to the variability of Kuroshio path. High (low) eddy activity is expected when the Kuroshio is in unstable (stable) state. Using the SSH index as a measure of eddy activity, we divided the rainfall and storm track data into two groups: one corresponds to active eddy years (AEY) and the other corresponds to inactive eddy years (IEY). We then contrast the rainfall and storm track between AEY and IEY.

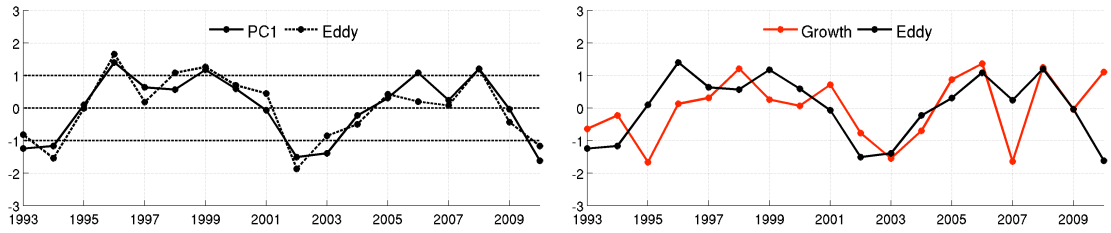


Figure 29. Left: Normalized meso-scale oceanic eddy index (1993-2010) derived from area-averaged winter season (NDJFM) standard deviation of high-pass filtered SSH (dashed, the area chosen is [30°N 40°N], [135°E 155°E]), and time series corresponding to the first EOF (PC1, solid) of winter season standard deviation of high-pass filtered SSH in the North Pacific, based on AVISO satellite data. Right: AVISO oceanic eddy index (PC1, black) and ECMWF storm growth index (red) from 1993 to 2010.

To obtain high-resolution rainfall observations, we used the relative short record of TRMM data (2000-2010) and selected three AEY (2002, 2003, 2010) and three IEY (2000, 2006, 2008) based on the SSH index (Figure 29). Figure 30 (top) shows the

difference of winter season mean rainfall between AEY composite and IEY composite. The resultant rainfall changes exhibit a decrease (increase) rainfall over the KER (USWC), which is quite consistent with the rainfall changes derived from the WRF simulations (Figure 24). The amplitude of rainfall decrease (increase) is also comparable with the rainfall change simulated by the model (Figure 24). To further examine the rainfall changes, we performed a rainfall PDF analysis in the KER and USWC using TRMM similar to those shown in Figure 24 (bottom) using the simulated rainfall. Figure 30 (bottom) shows a change in rainfall PDF that bears a close resemblance to the model simulation. In the KER, a greater number (15) of high rainfall (>10mm/day) event days

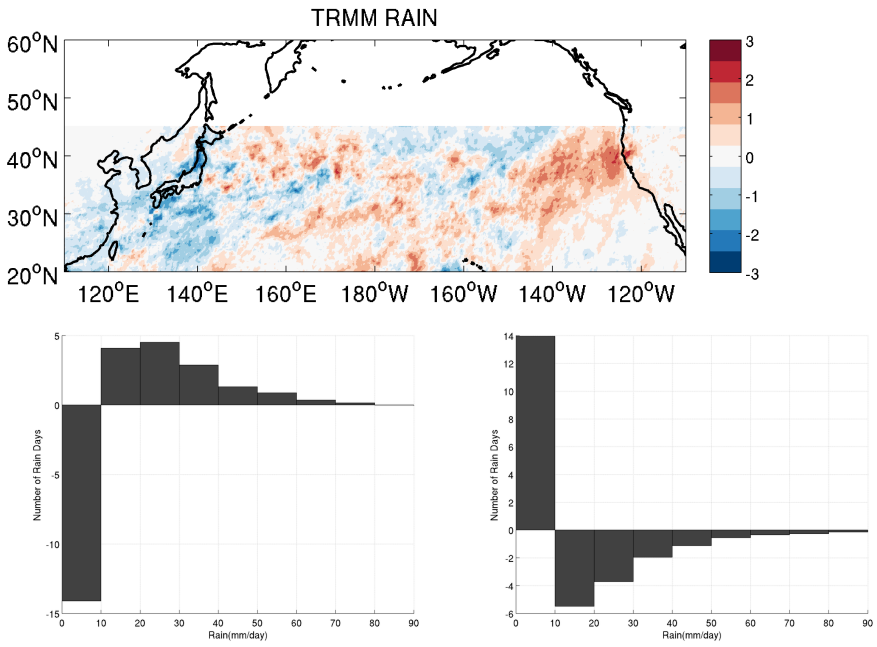


Figure 30. Similar as Figure 24, but for difference of winter season (NDJFM) mean rainfall (top, mm/d), rainfall PDF in KER (bottom left), and rainfall PDF in USWC (bottom right) between IEY and AEY derived from TRMM rainfall. IEY and AEY are chosen based on oceanic eddy index (PC1) derived from AVISO shown in Figure 29.

are observed in AEY than in IEY. On the contrary, a greater number (14) of low rainfall (<10mm/day) event days are observed in the USWC. This finding supports the modeling result that the presence of meso-scale oceanic eddies in CTRL tends to shift rainfall PDF toward high (low) rain rate over the KER (USWC).

The model simulations also show that meso-scale oceanic eddies are favorable for stronger storm growth possibly through the enhanced moist barcolinic instability. To validate this modeling result, ECMWF reanalysis data (1993-2010) was used to diagnose storm genesis over the KER. In order to define a storm growth index (Figure 29, right), we performed the following analysis: First, daily THF index was constructed in each NDJFM using observationally derived OAflux dataset. Second, similar lag composites as shown in Figure 26 were applied to 2-8 day band-pass filtered v' at 850 hpa on the storm days defined by the OAflux THF index. Third, the storm growth rate in each year was obtained by taking the difference between averaged storm intensity over the positive lag days (lag=1,2,3) and over the negative lag days (lag=-3,-2,-1). Figure 29 (right) shows that the storm growth index (red) and the ocean eddy activity index defined by the PC1 time series of the SSH standard deviation derived from AVISO (Figure 29, left). The two indexes are significantly correlated with r=0.47, supporting the model results that strong ocean eddies activity leads to strong storm growth in the KER.

To further compare time evolution of storms during the AEY (1996, 1999, 2006, 2008) and IEY (1993, 2002, 2003, 2010), lag composites of 2-8 day band-pass filtered v' at 850 hpa were made from lag -3 day to lag 3 day for AEY and IEY, respectively. Figure 31 and 32 show comparison between AEY and IEY storm evolutions and time

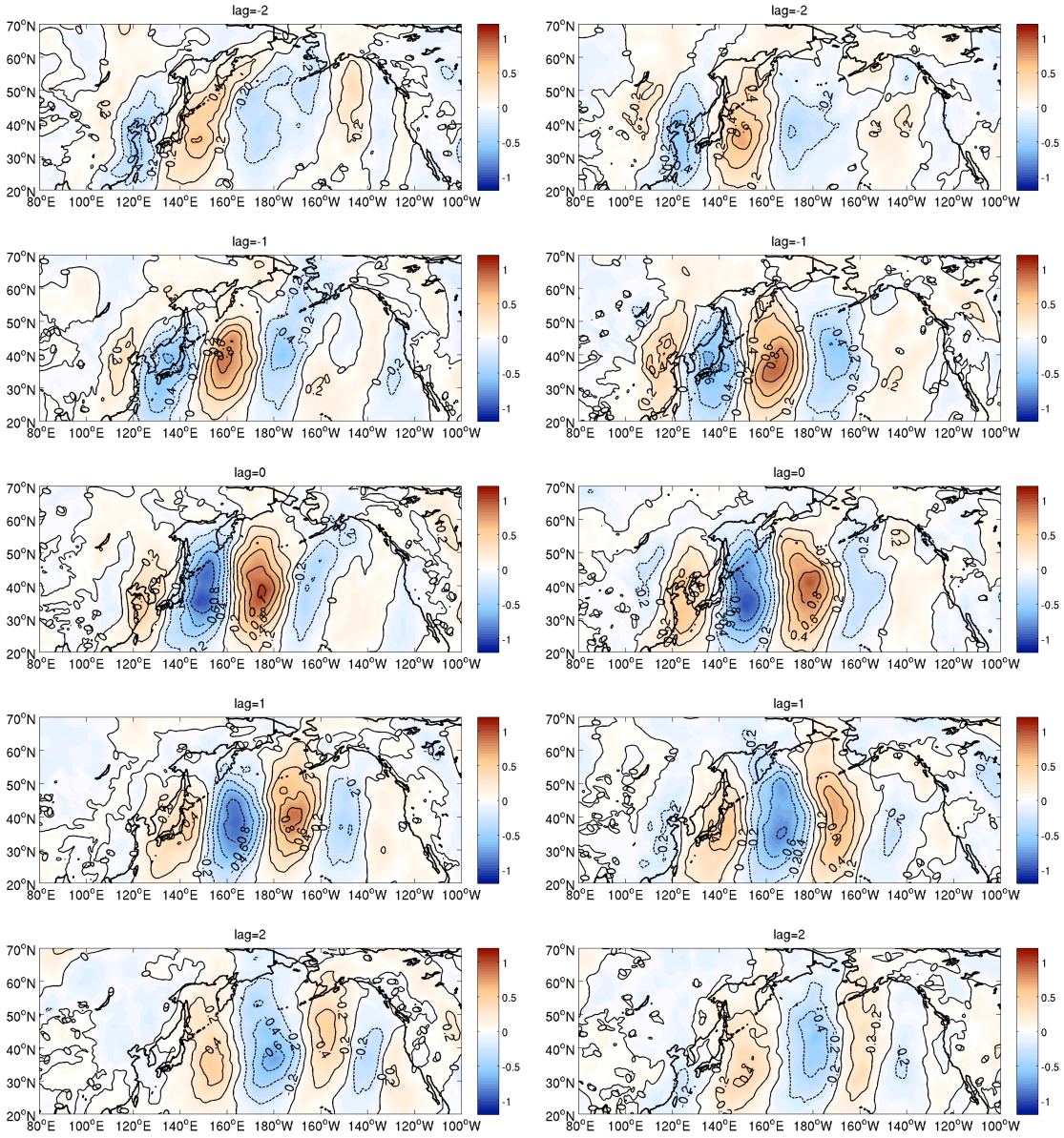


Figure 31. Similar to Figure 26, but for normalized lag composite in AEY (left) and IEY (right) derived from ECMWF reanalysis. AEY and IEY are again picked out based on AVISO oceanic eddy index (PC1) and storm days are picked out based on OAflux dataset.

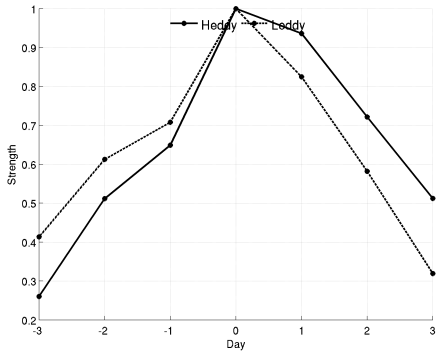


Figure 32. Similar to Figure 27, but for storm growth in AEY (solid) and IEY (dashed) derived from ECMWF reanalysis.

evolution of storm amplitude as previously shown in Figure 26 and 27 for the model simulations. We observe similar storm evolutions in the ECMW data to those in the WRF simulations. In particular, the storms during EAY decay more slowly than those during IAY as shown by both Figure 31 and 32. There is also an indication that the storms during AEY tend to have smaller spatial scale than those during IEY, although the differences in storm growth characteristics and spatial scales are less obvious than those in the WRF simulations. All these results are consistent with the model simulations.

To summarize, based on the limited available observations, we are able to present some persuasive evidence that provides strong support for the model results. Using the satellite-derived AVISO SSH data to measure meso-scale oceanic eddy activity in the KER, TRMM rainfall observations show a shift of rainfall PDF toward high (low) rain rate over the KER (USWC) during the active eddy years, consistent with the WRF simulations. The ECMWF reanalysis data show a tendency for stronger storm genesis

along the KER during the active eddy years, which is also consistent with the modeling results. However, the observational evidence for the oceanic eddy effect is generally less profound than that in the model simulations. This may be due to several factors: First, in the model simulations, nearly all the meso-scale SST variability was suppressed by the Loess filter, whereas in the observational analysis the eddy activity always exists even during the inactive eddy years. Second, in the model simulations, lateral boundary conditions that dictate synoptic variability were kept the same in all the model runs, whereas in the observational analysis synoptic systems that enter the Pacific basin vary from one year to the next, resulting in lower signal-to-noise in observational analyses. Finally, the sample size for the observational analysis is quite small due to the short record of the observational data and the quality of satellite-derived rainfall data may also contribute the weaker observational signal.

**3.5 Remote Influence of Oceanic Eddies**

The observational and modeling results presented in the previous section show that meso-scale oceanic eddies in the KER affect not only local rainfall and storm genesis, but also rainfall along the USWC, suggesting a remote influence of oceanic eddies. In this section, we will focus on examining dynamical processes that may be responsible for the remote influence of oceanic eddies.

It is well established that midlatitude atmospheric circulations are primarily driven by transient eddies. Derived from the momentum equation, E-vector has been introduced to understand the eddy-mean flow interaction in midlatitude atmospheric circulations and the divergence of E-vector governs the feedback of transient eddies onto the mean

flow (Hoskins et al. 1983). At an upper tropospheric level, the E-vector can be approximately expressed as (e.g., Hoskins et al. 1983):

$$E = (\overline{v'^2 - u'^2}, \overline{-u'v'})$$

Here, prime represents velocity induced by high frequency transient eddies. In the following analysis, u' and v' are represented by 2-8 day band-pass filtered u and v wind. The overbar represents a time average. The horizontal divergence of the E-vector indicates an acceleration of mean flow caused by transient eddies and the convergence of E-vector suggests a deceleration of mean flow at a given level.

Figure 33 shows the ensemble mean of $\nabla \cdot E$ in NDJFM at 300hpa in CTRL (top left) and MEFS (middle left). In the North Pacifc, the occurrence of cyclones and anticyclones generates a divergence of the E-vector downstream of the KER, extending northeastward from 150°E all the way to the eastern boundary of the Pacific Ocean (Figure 33, top left). The divergence of the E-vector overlies with the midlatitude jet stream and acts to accelerate the westerlies. The maximum divergence locates slightly downstream of the KE, following the explosive growth of storm tracks. In the western and central North Pacific, the divergence is stronger in CTRL than in MEFS (Figure 33, top left), consistent with the stronger local growth of storm tracks in the KER in CTRL than in MEFS. Further downstream in the eastern North Pacific, the divergence tends to extend a more southeastward in the MEFS compared to CTRL (Figure 33, middle left), consistent with the southeastward propagation of the storm track discussed in Section 3. The difference of $\nabla \cdot E$ between CTRL and MES is closely related with the different development of storm tracks. Figure 33 (right panel) shows the winter season mean eddy

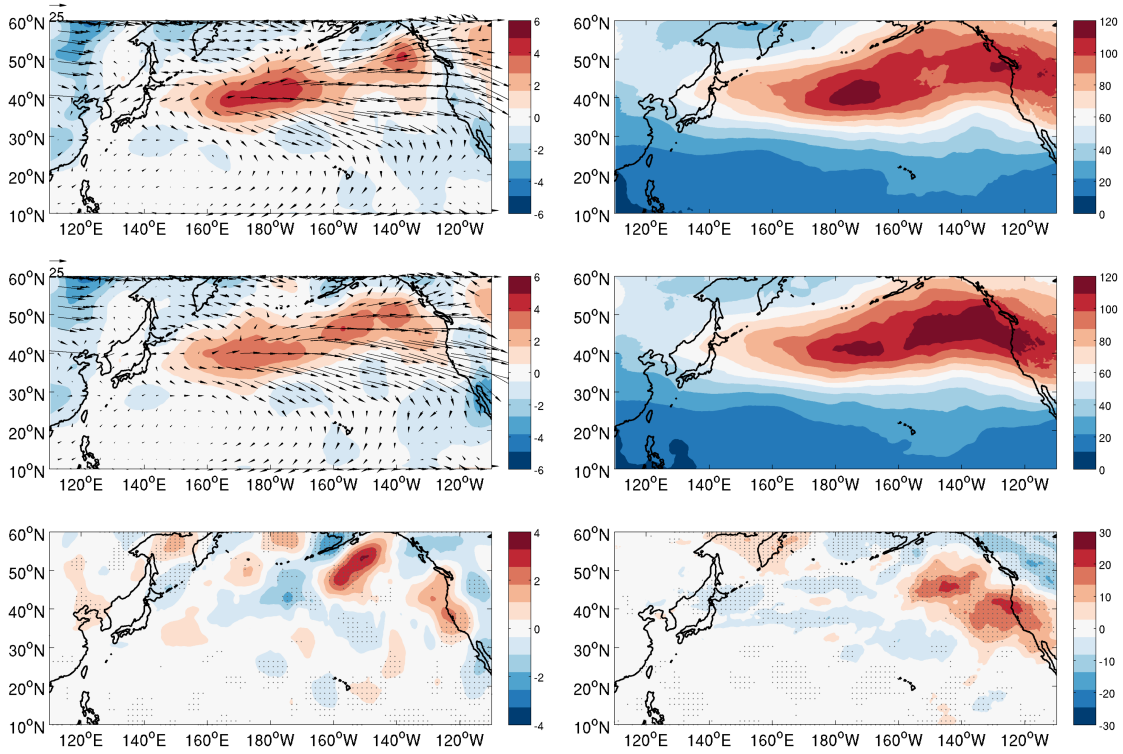


Figure 33. Winter season (NDJFM) mean E-vector ($m^2/s^2$, vector) and ($10^{-5}m/s^2$, shaded) in NDJFM at 300 hpa in CTRL (top left), MEFS (middle left) and the difference between MEFS and CTRL (bottom left) derived from all ensemble members in 27km WRF simulations. Right, similar to the left panel, but for EKE ($m^2/s^2$, shaded). Difference significant at 95% confidence level using a two-sided Wilcoxon rank sum test is shaded by gray dots.

kinetic energy (EKE) at 300hpa in CTRL and MEFS. In the CTRL, enhanced storm intensity caused by oceanic eddies in the KER region transfers more momentum to the mean flow and tends to accelerate the jet stream in the western and central North Pacific (Figure 33, top right). The removal of meso-scale oceanic eddies in the MEFS sustains an enhanced downstream development as well as a southward shift of storm tracks (Figure 33, middle right), leading to an increase in E-vector divergence in the eastern North Pacific and further modifying the mean flow there.

The difference of E-vector divergence between CTRL and MEFS suggests a potential modification on the mean flow due to different transient eddy activities. The winter season mean U wind at 300hpa (U300) simulated in the CTRL and the difference of U300 between MEFS and CTRL are shown in Figure 34 (top left and right). The jet stream peaks along the KER and decreases toward the east. Since the jet stream at 300hpa becomes relatively weak in the eastern North Pacific, a moderate change of transient eddies may cause significant change in the mean flow. As shown in Figure 34 (top right), consistent with the southeastward shift of $\nabla \cdot E$, the jet stream in the eastern North Pacific is significantly enhanced (about 25%) and displaced southward in the MEFS. The modification on low level jet (U wind at 850hpa, U850, Figure 34, bottom

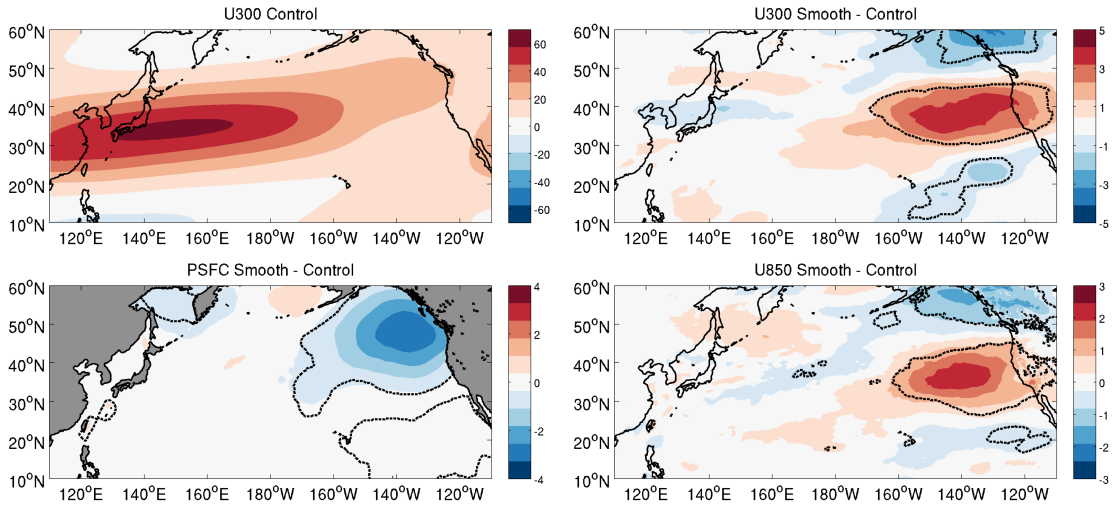


Figure 34. Winter season (NDJFM) mean zonal wind component U (m/s, shaded) at 300hpa in CTRL (U300, top left) and the difference between MEFS and CTRL derived from all ensemble members in 27km WRF simulations (top right). Bottom, similar to top right, but for surface pressure (mb, bottom left) and U850 (m/s, bottom right). Difference significant at 95% confidence level is outlined by black dashed line.

right) is also analyzed and the result shows a similar increase in the region and a southward shift of low-level westerlies, suggesting an equivalent barotropic mean flow response to changes in transient eddies. A negative surface pressure anomaly is found in the eastern North Pacific, accompanied with the change in the mean flow (Figure 34, bottom left). The upper level storm tracks exhibit a southward shift in the eastern North Pacific near the USWC in the MEFS compared to CTRL as shown in Figure 33 (right panel). The southward displacement of storm tracks is consistent with the southward propagation indicated in Figure 26 and is also consistent with the southward shift of $\nabla \cdot E$ (Figure 33, left panel). A further comparison between the southward shift of the storm tracks and reveals slightly displacement of the two locations. This may be caused by the fact that the storm propagation is further modified by change of the mean flow. The southward shift of the jet stream tends to guide the storms to propagate equatorward and thus displace the storm tracks further southward.

The southward shift of the jet stream and storm tracks in MEFS can be seen more clearly from the vertical section plot shown in Figure 35. There is an increase of U throughout the vertical section between 30°N-40°N and decrease of U between 50°N-60°N (Figure 35, left). The response peaks in the upper troposphere and decreases towards the surface, consistent with an equivalent barotropic response. The southward shift of storm tracks is shown to be confined in the upper troposphere (Figure 35, right).

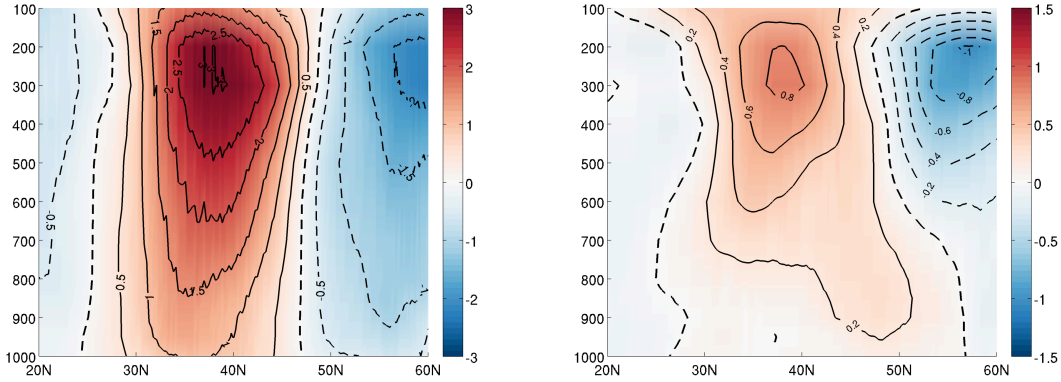


Figure 35. Vertical profile for difference of zonal averaged winter season mean U (contour and shaded, left) and storm track <v'v'> (contour and shaded, right) in the eastern North Pacific between MEFS and CTRL derived from all ensemble members in 27km WRF simulations. The zonal average is taken from 160°W to 110°W.

Therefore, we argue that the rainfall increase along the USWC in the MEFS can be attributed to the southward shift of storm tracks in the eastern North Pacific. The increased water vapor mixing ratio (Figure 28, left) locates in the same region where the storm tracks are displaces southward. It is conceivable that the intensified storm activity in the eastern North Pacific enhances high rainfall events, and thus produces higher winter mean rainfall in the USWC. This argument is also consistent with the finding that the rainfall change over the USWC is largely attributed to changes in the non-convective rain.

In summary, the WRF simulations suggest that meso-scale oceanic eddies in the KER can exert remote influences on rainfall and storm tracks in the eastern North Pacific. The underlying dynamic linkage between the eddy-rich region along the KER and far eastern North Pacific is through eddy-mean flow interactions. We conjecture that

meso-scale oceanic eddies support stronger storm genesis via moist baroclinic instability, which in turn affect transient eddy forcing downstream of the KER, and thus jet stream strength and position. In the absence of ocean eddies, the weakened storm genesis leads to a southward shift of the jet stream and storm tracks, causing an increase in high rainfall events and more winter mean precipitation along the USWC.

### 3.6 Summary

In this chapter, using a stand-alone 27 km WRF model, two ensembles of simulations (CTRL and MEFS) were conducted in boreal winter season (ONDJFM) in the North Pacific to study the possible local and remote influence of meso-scale oceanic eddies in the KER on the atmosphere. The simulations show that WRF is able to reproduce many observed features in the North Pacific sector, including high rainfall band along the Kuroshio and low- and upper-level storm tracks, when forced with observed high-resolution SST and lateral boundary conditions. The model further captured the observed meso-scale SST and surface wind relationship, indicative of the meso-scale air-sea coupling in the KER. Therefore, it is concluded that WRF provides a viable tool to study potential effects of meso-scale oceanic eddies on the atmosphere.

Comparisons between CTRL forced by the observed high-resolution SST and MEFS forced by the low-pass filtered SST reveal that 1) more than 80% of winter season SST variation in the KER can be explained by meso-scale oceanic eddies; 2) removal of meso-scale oceanic eddies in MEFS leads to a significant decrease of meso-scale atmospheric energy within the boundary layer, including a more than 30% reduction in meso-scale THF variance and 10% decrease in meso-scale PBLH variance,

along the KER. Therefore, it is concluded that meso-scale oceanic eddies along the KER can have a significant local impact on the overlying atmosphere.

In addition to the local impact, the model simulations also reveal a significant deeper troposphere response downstream of the eddy-rich region along the KE. In particular, the removal of the meso-scale oceanic eddies in MEFS causes a significant change in large-scale weather patterns over the North Pacific sector, which includes 1) a 20% decrease (increase) in winter mean precipition along the KER (USWC) and a shift in rainfall PDF towards low (high) rainfall rate in the KER (USWC); 2) a reduction in storm growth rate in the KER and an increase in storm wavelength as well as a southward shift in the jet stream and storm tracks in the eastern North Pacific.

Some of these simulated local and remote influences of meso-scale oceanic eddies have been validated using high-resolution satellite derived observations and reanalysis dataset. Using an oceanic eddy index constructed using AVISO SSH, composite analyses of TRMM rainfall observation reveal a reduction (increase) in winter mean precipitation and a shift of rainfall PDF towards low (high) rain over the KER (USWC) during inactive eddy years, which is consistent with the model simulations. Aanlyses of ECMWF data further indicate that during the inactive eddy years, storm genesis tends to be weaker than that during the active eddy years, which is also consistent with the modeling results.

Based on the modeling and observational results, we propose the following mechanism linking meso-scale oceanic eddy activity along the Kuroshio to North Pacific atmospheric circulations and weather patterns. Meso-scale oceanic eddies affect surface

winds and surface latent and sensible heat fluxes, which in turn affects the stability of the lower atmosphere and latent heat release. The diabatic heating modulated by meso-scale oceanic eddies can exert a significant influence on baroclinic instability along the KER through a positive feedback between diabatically induced low-level PV and upper-level PV, which in turn modifies storm genesis, affecting storm strength and spatial characteristics. The modified storms then affect the downstream jet stream through changes in transient eddy forcing and eddy-mean flow interaction. Finally, the change in jet stream strength and position modify storm tracks in the eastern North Pacific sector, resulting changes in winter season rainfall along the USWC. The following chapter, we will further examine the proposed mechanism using a high-resolution (9 km) coupled regional climate model simulations.

# CHAPTER IV

# FRONTAL-SCALE AIR-SEA INTERACTIONS ALONG THE KER SIMULATED BY A HIGH RESOLUTION CRCM

## 4.1 Introduction

The previous chapter along with recent studies using high-resolution satellite observations clearly demonstrates the potential for strong air-sea interactions along the WBC regimes, such as the KE. The positive correlation between meso-scale SST and surface winds indicates the ocean is forcing the atmosphere (Chelton et al. 2004; O'Neill et al. 2012). On the other hand, it has been well established that the atmosphere forces the ocean on various time and space scales. The meso-scale winds induced by meso-scale SSTs can influence the ocean by changing the oceanic eddies or Ekman pumping (Chelton et al. 2004; Small et al. 2008). As high-resolution observations are presently limited, coupled atmosphere-ocean models are viable tools to gain understanding of the meso-scale air-sea coupling dynamics.

WBCs, such as Kuroshio, are strong and narrow ocean current systems typically with a width of a hundred of kilometers or less. These currents flow in such a strength that they often are hydro-dynamically unstable, spawning meso-scale eddies of 50-100 km in diameter along their path. It has been demonstrated by many previous modeling studies that coarse-resolution ocean models are incapable of reproducing realistic WBCs and associated meso-scale eddies (Kagimoto and Yamagata 1997; Large and Danabasoglu 2006; Thompson and Cheng 2008;). The simulated WBCs in this class of

models typically overshoot along the coasts, producing systematic errors in separation latitudes of the currents from the coast. The simulated currents in coarse resolution ocean models are also much too weak and too broad, as well as leaning too close to the coast compared to observations. Only when horizontal resolution is reduced to 1/10° or finer, ocean models can begin to resolve the essential frontal dynamics governed WBC regimes and simulate realistically positions and structure of WBCs, as well as the associated meso-scale eddy activity (Guo et al. 2003; Kwon et al. 2010). This class of ocean models is referred to as eddy-resolving models.

As demonstrated in Chapter III, meso-scale oceanic eddies can potentially exert a strong influence on atmospheric circulation and weather patterns, owing to strong coupling between the atmosphere and ocean along these intense currents. To understand this frontal- and meso-scale air-sea coupling, it is essential that ocean models are capable of resolving narrow structures of WBCs and associated meso-scale eddies activity. In the context of this study, it means that the resolution of the ocean model needs to be finer than 1/10° in order to simulate realistic Kuroshio variability and meso-scale eddies in the KER, because spatial scale of oceanic eddies in the midlatitude is typically less than 100km (Stammer, 1997). At present, few global climate models are capable of running at eddy-resolving resolutions, because of prohibitively high computational costs. Regional ocean modeling approach offers an attractive alternative by reducing model domain in the region of interests. In this chapter, we apply the regional modeling approach to the North Pacific.

As demonstrated in the previous chapter, the most important atmospheric feature in midlatitudes during winter season is storm tracks. However, most of current generation AGCMs with 100 km or coarser horizontal resolution are likely to underestimate the strength of storm tracks (Bauer and Del Genio 2005; Gaffney et al. 2007; Orlansiki 2008; Willison et al. 2013). Bauer and Del Genio (2005) show that AGCMs with 4°x5° and 2°x2.5° horizontal resolutions produce much weaker and less cyclones compared with NCEP-NCAR and ERA-40 reanalysis. The deficiency of AGCM to simulate midlatitude storm tracks was further demonstrated by Gaffney et al. (2007) who computed the trajectories of surface winter storms simulated by a 2.8°x2.8° horizontal resolution coupled model and found a significant decrease of storm intensity in the cyclone entrance region along the east coast of the US. A higher resolution (1°x1°) GFDL (Geophysical Fluid Dynamics Laboratory) model presents a similar problem, generating weaker and southward shift storm tracks compared with reanalysis data (Orlanski 2008). The weak storm tracks in the coarse resolution AGCM simulations may attribute to the fact that coarse resolution models fail to properly resolve frontal cyclogenesis dynamics in WBC regimes (Bauer and Del Genio 2005; Wilson et al. 2013). Surface heat fluxes and precipitation simulations can also be influenced by the horizontal model resolution (Rouault et al. 2003; Hamilton et al. 1995; Kobayashi and Sugi 2004). Enhanced surface heat fluxes and rainfall were simulated as model resolution is increased. A review of how AGCM resolution can have an impact on simulations of tropospheric circulations can be found by Hamilton (2008). Orlanski (2008) suggested that winter cyclones can be simulated with a realistic intensity and

position only when model horizontal resolution increases to a 1/4° or finer. In this chapter, we will simulate the North Pacific storm track using a 9 km regional atmospheric model.

Satellite derived observational analyses indicate that at frontal- and meso-scales SST variability and surface-wind variability are positively correlated in many frontal regimes over the global ocean. Simulating this positive correlation is crucial for capturing meos-scale air-sea coupling in the WBC regimes and thus storm track variability. An analysis of the fourth generation of IPCC (Intergovernmental Panel on Climate Change) coupled model simulations indicate that most of the IPCC models either failed to reproduce the positive correlation between meso-scale SST and surface-wind variability or produced very weak positive correlation (Maloney and Chelton 2006), hinting that these models may underestimate storm track variability. Using a non-eddy-resolving and an eddy-resolving Ocean General Circulation Model (OGCM) coupled to an AGCM at different resolutions, Bryan et al. (2010) examined the positive correlation between meso-scale SST and surface winds in major frontal with different combinations of OGCM and AGCM resolutions and found that the positive correlation can only be reproduced when the ocean model resolves meso-scale eddies. However, Bryan et al. (2010) did not examine how the simulation of storm tracks is affected by varying resolutions of the OGCM and AGCM. In this chapter, we will examine the effect of resolving oceanic eddies on both the near surface atmospheric response and upper-level atmospheric response.

An issue that has not been adequately addressed by previous studies is how the ocean-eddy induced atmospheric response will feed back onto the ocean circulation. The positive correlation between meso-scale SST and surface-winds suggests that there should be at least a local feedback of the atmosphere onto the meso-scale SST. Xie (2004) and O'Neill et al. (2005) argue that this feedback is negative, because warm SSTs tend to drive high wind speed and enhance latent and sensible heat release from the ocean to the atmosphere, which in turn cools the SST. In other words, the atmosphere generally has a damping effect on the meso-scale SST variability. Vecchi et al. (2004) found a 60-day decaying time scale for meso-scale SST variability due to heat flux in the Arabian Sea. However, how the surface wind and heat flux response to meso-scale SST can feedback onto the oceanic front and the associated circulation is not well understood.

As shown by Chelton et al. (2004), the acceleration of wind speed over warm eddies and deceleration over cold eddies can result in frontal scale wind stress curl and wind stress divergence in eddy-rich regions. The frontal scale wind stress curl and wind stress divergence can also be generated when winds are along and across strong SST gradients, respectively. These meso-scale wind stress features can produce local Ekman pumping/suction, which may influence recirculation gyres in WBC regions. The influence of this frontal scale wind stress on the ocean circulation may not be negligible (Chelton et al. 2006, 2007; Xie 2004). Chelton et al. (2004) estimated that neglecting these frontal scale wind stresses may result in about 20% reduction in poleward water volume transport by WBCs. Furthermore, it is possible that the meso-scale wind stress

forcing may modify oceanic eddy fields (Muller and Frankignoul 1981; White and Annis 2003; Spall 2007), but this possibility has not been adequately explored.

The heat flux and surface wind response to meso-scale oceanic eddies can modify upper ocean mixing by affecting upper ocean stratification and wind stirring, resulting changes in ocean mixed layer depth (MLD). An enhanced surface turbulent heat flux and wind speed over warm oceanic eddies tend to strengthen vertical mixing and deepen ocean MLD. In the KER and GSR, this deepening of MLD may result in the Subtropical Mode Water (STMW) formation. The STMW forms along the northern boundary of North Pacific and North Atlantic subtropical gyre when surface cooling causes enhanced vertical mixing and deepened MLD (Hanawa and Talley 2001; Kelly et al. 2010). Qiu et al. (2007) argue that mesoscale eddies may influence the STMW in two ways: "first, enhanced eddy activity hinders the formation of deep mixed layer by modifying the upper ocean stratification; second, it provides a direct source of high potential vorticity (PV) water to mix with the surrounding low-PV STMW". If these arguments are proven true, it may suggest a positive feedback of meso-scale atmospheric response to SST onto the generation of STMW. Understanding these issues is fundamentally important because STMW variability has been argued to play a critical role in extratropical decadal climate variability (Qiu and Chen 2006; Kelly et al. 2010).

The overall objective of the study described in this chapter is to improve our understanding of frontal- and meso-scale air-sea interactions along the KER using a high-resolution Coupled Regional Climate Model (CRCM) capable of explicitly resolving meso-scale oceanic eddies and frontal cyclogenesis. First, we will introduce

the CRCM by describing its physics and coupling methodology in Section 2. We will then examine in Section 3 the atmospheric response to meso-scale oceanic eddies using higher resolution WRF (9 km) forced by simulated SST (9 km) that explicitly resolves meso-scale oceanic eddies and compare the results to those simulated by 27 km WRF as discussed in Chapter III. In Section 4, we will focus on examining possible feedbacks of ocean-eddy induced atmospheric response onto the ocean by conducting high-resolution CRCM simulations. Finally, in section 5, we draw major conclusions of the study and discuss their implications.

## 4.2 Model Description and Experiment Design

### *4.2.1 CRCM*

CRCM used in this study is developed at Texas A&M University. It includes a regional atmospheric model, WRF, developed by NCAR and a regional ocean model, Regional Ocean Modeling Systems (ROMS), developed by Rutgers University and UCLA. The atmosphere WRF model has been described in 3.2.2 and a brief description of ROMS will be given as follows.

ROMS is a free-surface, hydrostatic, primitive equation ocean model that uses stretched, terrain-following coordinates in the vertical and orthogonal curvilinear coordinates in the horizontal. The model is based on the Arakawa C grid and a vertical S-coordinate that allows high resolutions in regions where ocean stratification bears large changes, such as thermocline. The horizontal coordinate used in study is a Cartesian coordinate. The reason that we choose this model as the ocean component is

that it is designed to explicitly deal with regional oceanic circulations, such as Kuroshio in the KER, which is the focus of this study.

The CRCM is configured with ROMS and WRF both at 9 km horizontal resolution. The model domain covers the entire North Pacific (Chapter III, Figure 17) with the WRF domain slightly larger than the ROMS domain. The WRF domain covers a region from 3.6°N to 66°N in latitude and from 99°E to 270°E in longitude (the outer domain), while the ROMS domain covers a region from 8.5°N to 62.8N latitude and from 105°E to 255°E longitude (the inner domain). Figure 17 of Chapter III shows both model domains. A Mercator projection with a uniform grid is used for both WRF and ROMS. In fact, the ROMS grids are extracted from the WRF grid to make the ocean and atmosphere grids match in order to avoid mismatch between land- and ocean-surface heat fluxes. All settings and parameterization schemes used in the 9 km WRF are the same as those describes in 3.2.2. For ROMS, there are 50 S-coordinate levels with a minimum depth of 10 m. The model ocean depth is compressed to 5500 m based on assumption that below that depth, ocean currents are negligibly weak and the spatial structure is uniform. Physics parameterization schemes adopted in the ROMS include a KPP (K-profile parameterization, Large et al. 1994) vertical turbulent mixing closure scheme, a bi-harmonic horizontal Smagorinsky mixing for the momentum (Smagorinsky 1963) and a Laplacian horizontal mixing for tracer diffusion. Bottom friction uses a fourth-order quadratic scheme.

Before coupling to WRF, ROMS was spun up for 6 years (1997-2002). The spin-up run was initialized with the Simple Ocean Data Assimilation (SODA) data in January 1,

1997 and forced with observationally derived atmospheric surface variables from the Co-ordinated Ocean-Ice Reference Experiments (CORE II)'s dataset based on surface heat flux bulk-formula described in Fairall et al. (1996) At the southern open boundary, the model is forced with 5-day mean flow conditions derived from SODA. Additionally, sea surface salinity and SST derived from SODA are also applied at the model's sea surface to correct errors in net sea-surface fresh water and heat fluxes with a restoring time scale of 20 days.

WRF and ROMS are coupled every hourly. At each coupled step, ROMS provides SST for WRF in the overlapped domain to change the low boundary condition in the atmosphere, while WRF provides atmospheric surface variables, including net shortwave radiation, net heat flux, precipitation, evaporation, zonal and meridional wind stresses for ROMS to calculate net surface fluxes to force the ocean.

*4.2.2 Experiment Design*

Three sets of experiments are designed to study the meso-scale air-sea coupling in the KER. The first experiment is a fully coupled CRCM run (CTRL). CTRL was initialized on October 1, 2002 from ROMS' spin-up simulation from 1997 to 2002. Once coupled, the low boundary forcing of WRF is provided by ROMS at every coupled step (hourly). The ROMS spin-up run was extensively analyzed and the simulated structure of the Kuroshio and the recirculation gyre in the KER was compared to the existing hydrographic observations. The simulated meso-scale oceanic eddy variability along the KER was validated against the satellite derived AVISO SSH. The model-data comparison show that the 9 km ROMS simulates well the observed Kuroshio path and

the oceanic eddy activity along the KER. The results of the ROMS simulation will be reported in a separate study and will not be shown here. The CTRL serves as a reference for the other two experiments designed to dissect the frontal- and meso-scale air-sea interaction dynamics.

The second experiment is an ensemble of two uncoupled 9 km WRF simulations forced by low-pass filtered 9 km SST derived from CTRL. Different from the MEFS described in the previous chapter, the SST used here is the hourly SST taken directly from the CRCM coupler at each coupled step in CTRL. As such, if the identical initial condition to that of CTRL is used for the uncoupled WRF run, WRF will reproduce exactly the atmospheric variability in CTRL (this has been verified). This will assure that any change in the atmosphere in the uncoupled WRF runs is a result from the change of low boundary SST forcing. To be consistent with the previous MEFS, a Loess filter with a half-width of 15° in longitude and 5° in latitude was applied to the 9 km simulated hourly SST to remove meso-scale oceanic eddies. The two runs differ in WRF initial condition with one being identical to that of CTRL and other being taken from a different date (October 1, 1999). Hereafter, we refer this experiment as to uncoupled meso-scale eddy filtered simulation (UNCPL-MEFS). The CTRL and UNCPL-MEFS are designed to further validate the results presented in the previous chapter using a finer resolution and a more consistent SST field.

The third experiment is designed to examine potential feedbacks of the ocean-eddy induced atmospheric response onto the ocean circulation. To do so, we applied the same Loess filter as in UNCPL-MEFS to the simulated SST while the model is running in a

fully coupled mode. That is, at each coupled step, ROMS simulated SST is filtered first and then passed onto WRF, so that WRF only "sees" the large-scale SST. ROMS in turn is forced by the atmospheric surface fluxes that contain no responses to meso-scale oceanic eddies. We refer this experiment as coupled meso-scale eddy filtered simulation (CPL-MEFS). All these three sets of experiments are integrated from October 1, 2002 to March 31, 2003.

**4.3 High-resolution Model Simulation of Ocean-eddy Effects on the Atmosphere**

As discussed in the previous chapter, at large-scales the atmosphere predominately forces the ocean in midlatitudes, while at meso-scales the ocean influences the atmosphere. The different characteristics of the large-scale versus meso-scale midlatitude air-sea interactions can be verified using the high-resolution CRCM simulation. To do so, we first separated the simulated daily SST and THF into large-scale and meso-scale components using the Loess-filter, upon removing the seasonal cycle. Figure 36 compares time series of the large-scale and meso-scale SST and THF anomalies derived from CTRL averaged over a 1°x1° area within the KE. At large-scales, there is a well-defined high-frequency fluctuation of THF associated with synoptic storms and THF is anti-correlated with SST (Figure 36, top left), meaning that a positive THF anomaly (above-normal heat release from the ocean into the atmosphere) corresponds to a negative SST anomaly (cooling at the sea-surface). The lag-correlation between the time series (Figure 36, bottom left) shows a clear asymmetry about the lag 0 day with a maximum negative correlation (~-0.42) occurring when THF leads SST by 1 day and insignificant correlations when SST leads. This is indicative of atmosphere-

forcing-ocean, as shown in previous studies (e.g., Barsugali and Battisti 1998). In contrast, at meso-scales THF and SST exhibit a clear co-variability at a lower frequency (Figure 36, top right), suggesting that the temporal variability of the surface heat fluxes at these spatial scales is dictated by the slowly varying oceanic field. The lag-correlation between the two time series shows a near perfect symmetry about lag 0 day with a maximum positive correlation of close to 0.9 at lag 0 day, indicating that at these spatial scales warm SST anomalies lead to more heat release from the ocean to the atmosphere. These results collaborate strongly with the previous modeling and observational findings that at meso-scales, the ocean is forcing the atmosphere in the KER, while at large-scales the atmosphere is forcing the ocean.

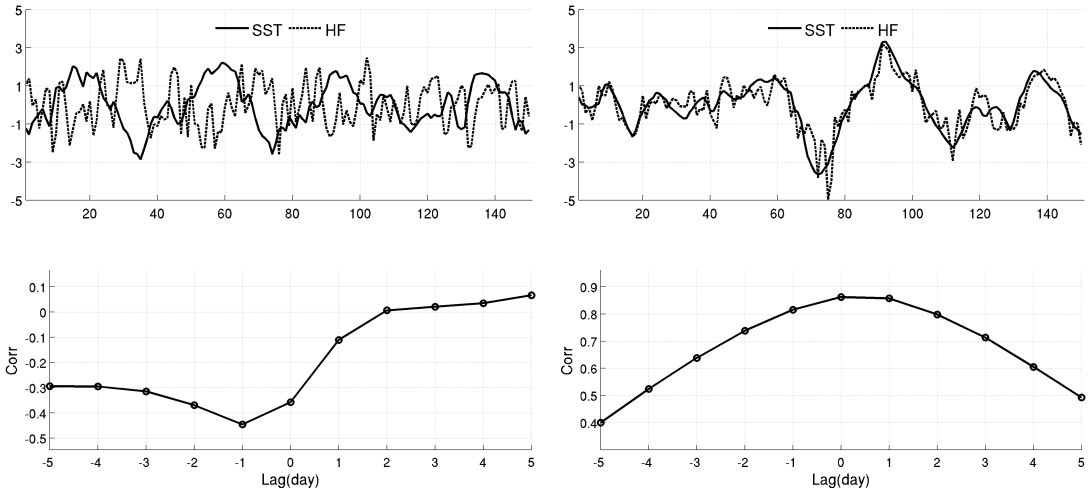


Figure 36. Area-averaged daily low-pass (top left) and high-pass (top right) filtered SST (°C, solid) and THF ($W/m^2$, dashed) anomalies in 2002/3 NDJFM simulated in 9km CRCM CTRL. The area chosen a 1°x1° box near the KE. Lag correlation between low-pass (bottom left) and high-pass (bottom right) filtered SST and THF anomalies with seasonal cycle removed from lag -5 day to lag 5 day. Negative lags correspond to atmosphere leading, positive lags correspond to ocean leading.

In Chapter III, using ensembles of uncoupled 27 km WRF simulations, we have shown that removal of meso-scale oceanic eddies can result in a local meos-scale atmospheric boundary layer response that includes a decrease in THF, surface wind and PBLH variance in the KER. Additionally, a deeper tropospheric response including a decrease (increase) of winter season mean rainfall along the KER (USWC) and a reduction in storm growth rate is also found. Finally, a remote response in the storm track and jet stream position in the eastern North Pacific is identified. In the following, we will assess similar atmospheric responses in UNCPL-MEFS using the 9 km WRF.

Figure 37 illustrates the difference of winter mean (NDJFM) meso-scale variability in SST, THF, PBLH and10m wind between UNCPL-MEFS and CTRL. As expected, the removal of meso-scale SST using the Loess filter results in a significant reduction of the winter mean SST variance. In response to the reduction in meso-scale SST variability, there are significant decreases in meso-scale THF (~ 80%), PBLH (~60%) and surface wind (~50%) variation in the KER (Figure 37). In comparison to the results of the 27 km WRF simulations discussed in Chapter III, the reduction in the UNCPL-MEFS is generally stronger, possibly due to the fact that the enhanced model resolutions simulate stronger meso-scale variability in the KER. When comparing the 9 km UNCPL-MEFS and 27 km MEFS results, one must bear in mind that the two experiments were conducted in different years (2002/3 for UNCPL-MEFS and 2007/8 for MEFS), therefore, some of the differences discussed above may also be attributed to different atmospheric and oceanic conditions between these two time periods.

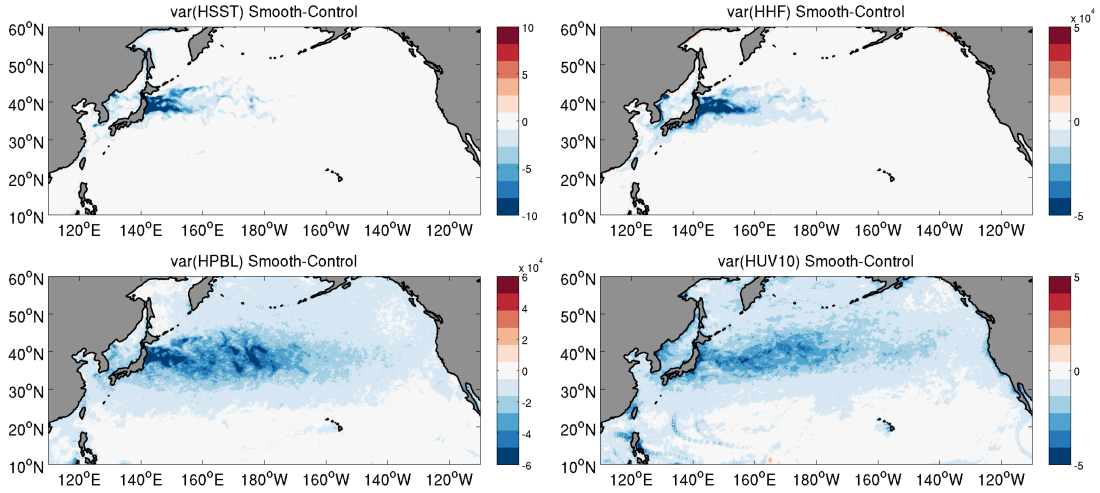


Figure 37. Similar to Figure 22 (e, f, g ,h), but for difference of NDJFM variance of high-pass filtered SST (top left), THF (top right), PBLH (bottom left) and 10m wind speed (bottom right) between UNCPL-MEFS and CTRL. Simulations are conducted using a 9km CRCM.

As in MEFS, UNCPL-MEFS, also reveals a striking change of winter season mean rainfall (Figure 38), including a significant decrease of rainfall along the KER and increase of rainfall along the USWC. Compared to MEFS, the rainfall decrease in UNCPL-MEFS occurs more to the downstream of KER with a higher amplitude. A separation of rainfall into convective rainfall and large-scale rainfall demonstrates that the rainfall decrease in the KER is dominated by convective rainfall. The rainfall increase over the eastern North Pacific has a similar spatial structure to that in MEFS, except with a larger amplitude. The increase in rainfall along the USWC is more influenced by the large-scale rainfall than the convective rainfall (Figure 38).

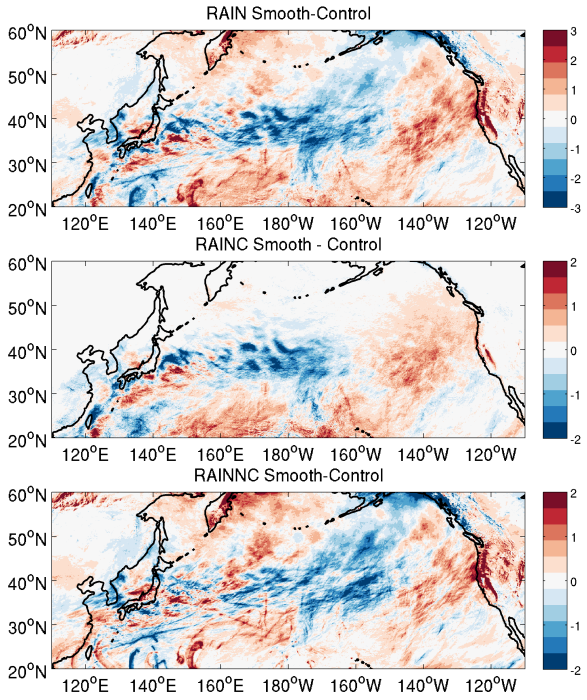


Figure 38. Difference of winter season (NDJFM) mean total rainfall (mm/d, top), convective rainfall (middle) and non-convective rainfall (bottom) between UNCPL-MEFS and CTRL. Simulations are conducted using a 9km CRCM.

The effect of meso-scale oceanic eddies on storm genesis in the KER is also investigated by performing lag composite analysis of 2-8 day band-pass filtered v' on storm days (Figure 39). A comparison of the lag composites of the filtered v' at 850hpa between CTRL (left) and UNCPL-MEFS (right) shows that storms in CTRL have much stronger growth and reach their peak at lag 1 day after passing through the KER, whereas the storms in UNCPL-MEFS reach their peak at lag 0 day and experience a weak decrease in strength at lag 1 day. This stronger growth in the storm track downstream of the KER in the high-resolution 9 km model simulations compared to the

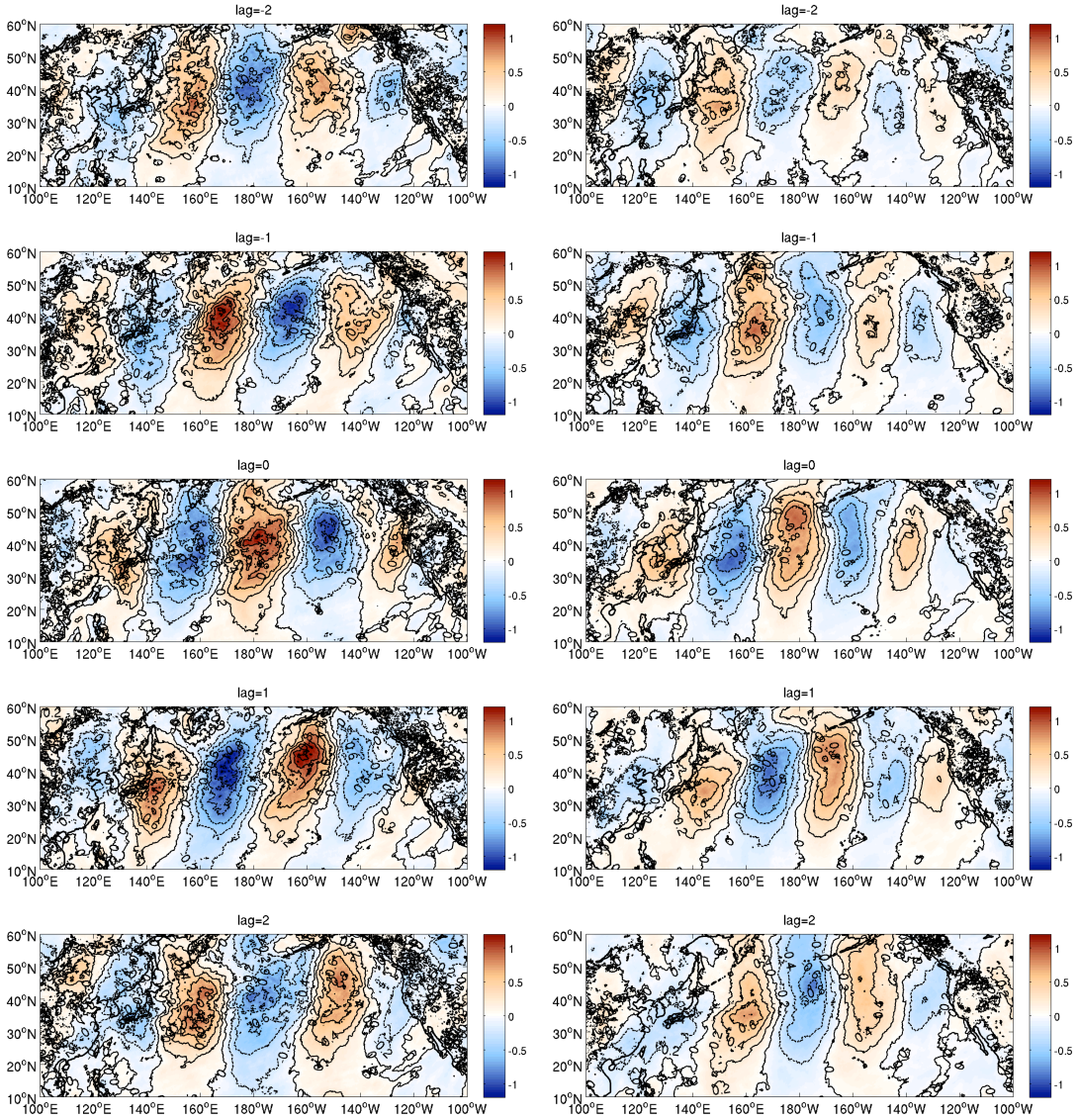


Figure 39. Similar to Figure 26, but for normalized lag composite (contour and shaded) of 2-8 day band-pass filtered 850hpa meridonal wind (v') on storm days from lag -2 day to lag 2 day for CTRL (left) and UNCPL-MEFS (right). Simulations are conducted using a 9km CRCM.

low-resolution 27 km model simulations may offer an explanation to the stronger precipitation response downstream of the KER in the high-resolution model simulations than in the low-resolution model simulations shown in Figure 39. One feature that is

inconsistent with the 27 km WRF simulations is that there are no obvious changes in the spatial scale of storms in CTRL and UNCPL-MEFS. This finding does not support the moist baroclinic instability theory. A possible explanation to this discrepancy between model and theory may be that the diabatic heating in the high-resolution model simulations is so strong that the storm genesis can no longer be explained by the linear moist baroclinic instability theory (see Ahmadi-Givi 2002 for a more detailed discussion).

The remote influences of oceanic eddies on the North Pacific jet stream and storm track are examined by contrasting the simulated zonal velocity U and 2-8 day band-pass filtered v' variance, <v'v'>, between CTRL and UNCPL-MEFS. In the western and central North Pacific along the KER, the weakened storm track over the KER due to the suppression of oceanic eddies in UNCPL-MEFS (Figure 40, bottom left and right) causes a significant deceleration of the midlatitude jet stream at 850hpa and 300hpa (Figure 40, middle left and right). North of the KER in the western and central North Pacific, there is an acceleration of the jet stream. The dipole pattern of the jet stream change suggests that in the UNCPL-MEFS, the jet stream is shifted poleward over the KER. Downstream in the eastern North Pacific, there is an increase of the jet stream in the south and a decrease in the north, indicative of a southward shift of the jet stream in the eastern North Pacific when meso-scale oceanic eddies in the KER is suppressed. As a result, in the high-resolution UNCPL-MEFS, the jet stream tends to bend northward in western and central North Pacific and move southward in the eastern basin, forming more of an arc than a straight path compared to CTRL. This different appearance of the

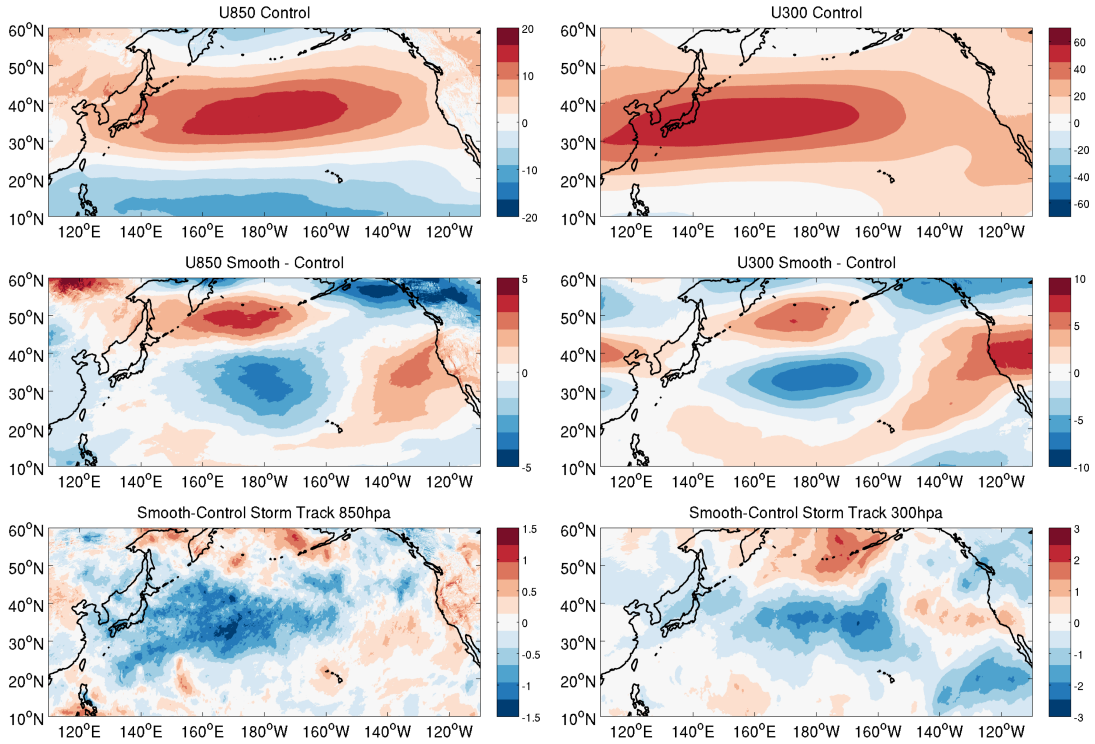


Figure 40. Winter season (NDJFM) mean horizontal wind component U (m/s) at 850hpa (top left) and 300hpa (top right). Difference of winter season mean U (middle) and winter season storm track <v'v'> at 850hpa (left) and 300hpa (right) between UNCPL-MEFS and CTRL. Simulations are conducted using a 9km CRCM.

jet stream in the western and central North Pacific may again be attributed to the stronger response of storm genesis to oceanic eddies in the high-resolution model simulations noted above. However, a more careful analysis is needed to further understand the differences between the 27 km and 9 km WRF simulations.

In summary, the suppression of meso-scale oceanic eddies in the 9 km WRF simulations results in an atmospheric response that shares many common features to the atmospheric response simulated by the 27 km WRF in a similar setting as discussed in Chapter III. In particular, an increase (a decrease) in rainfall along the KER (USWC)

was found in both experiments. A reduction of storm growth rate over the KER and a southward shift in storm tracks in the eastern North Pacific were also simulated in both model experiements. The consistency between the low and high resolution model simulations demonstrates the robustness of the conclusion drawn in Chapter III that meso-scale oceanic eddies can exert a significant influence on atmospheric circulation and weather patterns over the North Pacific sector. However, the comparison between the low and high resolution model simulations also reveals some important differences in the simulated atmospheric response. In particular, the high-resolution simulations produce a much stronger response in rainfall, storm genesis, storm track and jet stream just downstream of the KER over the western and central North Pacific compared to the low-resolution simulations. Although the cause of this difference needs further investigation, we speculate that the stronger diabatic heating response to meso-scale oceanic eddies simulated by the high-resolution model may be primarily responsible for the difference.

**4.4 Feedbacks of Ocean-eddy Induced Atmospheric Response onto the Ocean**

In this section, we devote to the question of how ocean-eddy induced atmospheric response can potentially feedback onto the ocean. To investigate this issue, we will analyze the CPL-MEFS and compare the results to those of CTRL. The analysis presented should be considered as preliminary.

We begin with the analysis of SST. Figure 41 (left) shows the winter season (NDJFM) mean SST difference between CPL-MEFS and CTRL. It is evident that there is a significant warming (~3°-4°C) of sea-surface just north of the Kuroshio front in

CPL-MEFS compared to CTRL. In the CPL-MEFS, the atmosphere does not "feel" the meso-scale SST induced by oceanic eddies. As such, it does not contain the meso-scale atmospheric response in surface THF and surface winds as in CTRL, which acts to damp the meso-scale SST by enhancing (reducing) latent and sensible heat release over warm (cold) ocean eddies. The absence of the negative feedback between the meso-scale SST and surface THF thus causes the meso-scale SST anomalies to persist longer in CPL-MEFS than in CTRL. This can contribute to the SST difference between CPL-MEFS and CTRL.

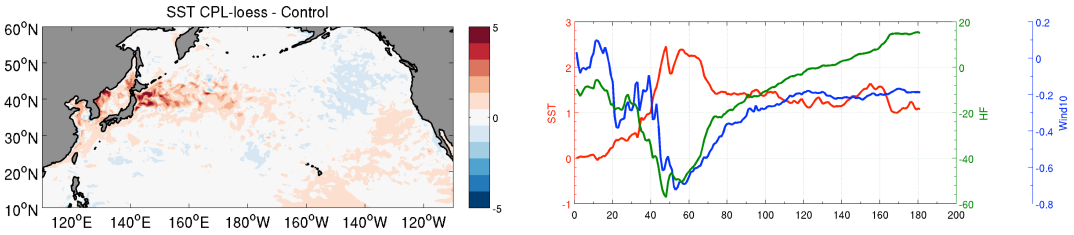


Figure 41. Difference of winter season (NDJFM) mean SST (°C, left) between CPL-MEFS and CTRL in 9km CRCM simulations. Time evolution of SST (°C, red), integrated HF ($W/m^2$. green), integrated 10m wind speed (m/s, blue) anomalies between CPL-MEFS and CTRL from 10/01/2002 to 03/31/2003.

Along the Kuroshio Front, warm and cold oceanic eddies are generated and subsequently propagate meridionally, both poleward and equatorward. When warm eddies propagate poleward, they carry warm water into the cold region north of the Kuroshio, causing warming in the region. Therefore, the warm eddy statistics in the region can play an important role in determining the mean SST. The fact that the eddies

are less damped in CPL-MEFS than in CTRL due to the lack of the negative feedback between meso-scale SST and surface THF in CPL-MEFS can enhance the warm-eddy effect on SST, causing warming north of the Kuroshio Front. This effect is illustrated in Figure 41 (right), which shows the time evolution of SST, surface winds and THF differences between CPL-MEFS and CTRL averaged over a region (40°N-45°N, 140°E-160°E). It is evident that the surface warming in CPL-MEFS corresponds to lower surface winds and lower surface THF. It is also worth noting that the reduction in THF in CPL-MEFS exists at very early stage of the simulation when no surface warming is present, suggesting that the change in THF causes the change in SST.

The enhanced eddy activity north of the Kuroshio Front is validated by comparing the standard deviations of the high-pass filtered SST in CPL-MEFS and CTRL (Figure 42, left). It is evident that north of the Kuroshio Front the meso-scale SST variance in CPL-MEFS is considerably higher than in CTRL. Interestingly, the increase in meso-scale SSH variance in CPL-MEFS compared to CTRL is less significant than that in the SST (Figure 42, middle), suggesting that some of these meso-scale SST variability may be trapped near the surface and do not produce a significant SSH response.

An issue with this eddy-driven SST mechanism is that one expects to see a similar effect of the cold eddies south of the Kuroshio Front, which should produce a surface cooling. However, there is little evidence for enhanced surface cooling south of the Kuroshio Front in Figure 41 (left). One possible explanation is that the atmospheric fluxes have a less impact on cold eddies than warm eddies. Further studies are clearly needed to understand this issue.

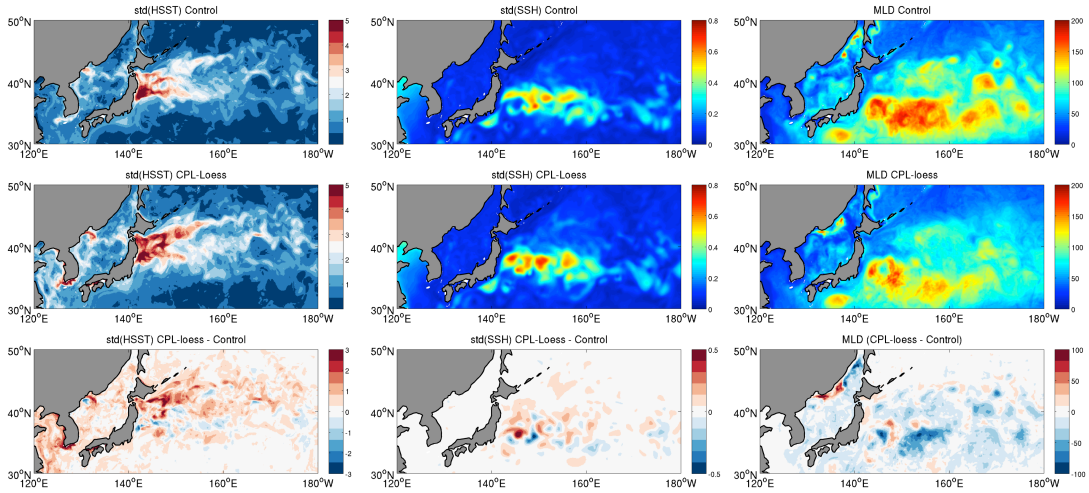


Figure 42. Standard deviation of winter season (NDJFM) high-pass filtered SST (°C, left) and SSH (m, middle), winter season mean MLD (m, right) in CTRL (top), CPL-MEFS (middle) and the difference between CPL-MEFS and CTRL (bottom) in 9km CRCM simulations.

The suppression of the meso-scale oceanic eddy effect on the atmosphere in CPL-MEFS not only affects the SST, but also results in a significant response in oceanic mixed layer. Figure 42 (right) illustrates the winter season mean MLD in CTRL and CPL-MEFS. There is a remarkable decrease (as much as 50%) of the MLD in CPL-MEFS compared to CTRL (Figure 42, right panel, bottom). In the winter season, over the warm side of the KE, large air-sea temperature and moisture difference leads to intensive sensible and latent heat release, which enhances vertical turbulent mixing and produces a thick MLD south of KE (Figure 42, right panel, top). In the CPL-MEFS, the weakened meos-scale atmospheric heat fluxes reduce vertical mixing, resulting in a thinner MLD. Additionally, the decrease of meso-scale surface wind variability is also likely to contribute to the weakened vertical mixing, leading to a shallower mixed layer.

Finally, we examine the question of whether the ocean-eddy induced atmospheric response can feedback onto the Kuroshio and its frontal structure. Figure 43 shows a zonally averaged temperature and zonal velocity cross-section across the KE between 140°E and 180°E. The strong Kuroshio current is well simulated in CTRL and is accompanied by a strong meridional temperature gradient near 37°N-40°N, extending throughout the upper 500 m (Figure 43, top). In CPL-MEFS the simulated temperature gradient is significantly weakened, consistent with a weakened Kuroshio (Figure 43, middle). The difference between the two simulations reveals a clear dipole temperature pattern with warmer (colder) temperature north (south) of the Kuroshio Front in CPL-MEFS than in CTRL (Figure 43, bottom left). The zonal velocity difference between CPL-MEFS and CTRL shows a clear weakening near the core of the Kuroshio current and broadening in its meridional structure (Figure 43, bottom right) when the effect of oceanic eddies on the atmosphere is removed. These results unambiguously show that the ocean-eddy induced atmospheric response can feedback onto the Kuroshio and its frontal structure.

We propose the following mechanism to explain the above result. The poleward (equatorward) propagation of warm (cold) ocean eddies generated along the Kuroshio front tend to diffuse the strong temperature gradient of the Kuroshio front. When the effect of ocean eddies on the atmosphere is removed in CPL-MEFS, the eddies become less damped and their life span is increased. As a result, the eddy-induced diffusion effect on the Kuroshio temperature front is enhanced, causing a weakening in the cross-front temperature gradient, which in turn causes a decrease in Kuroshio strength.

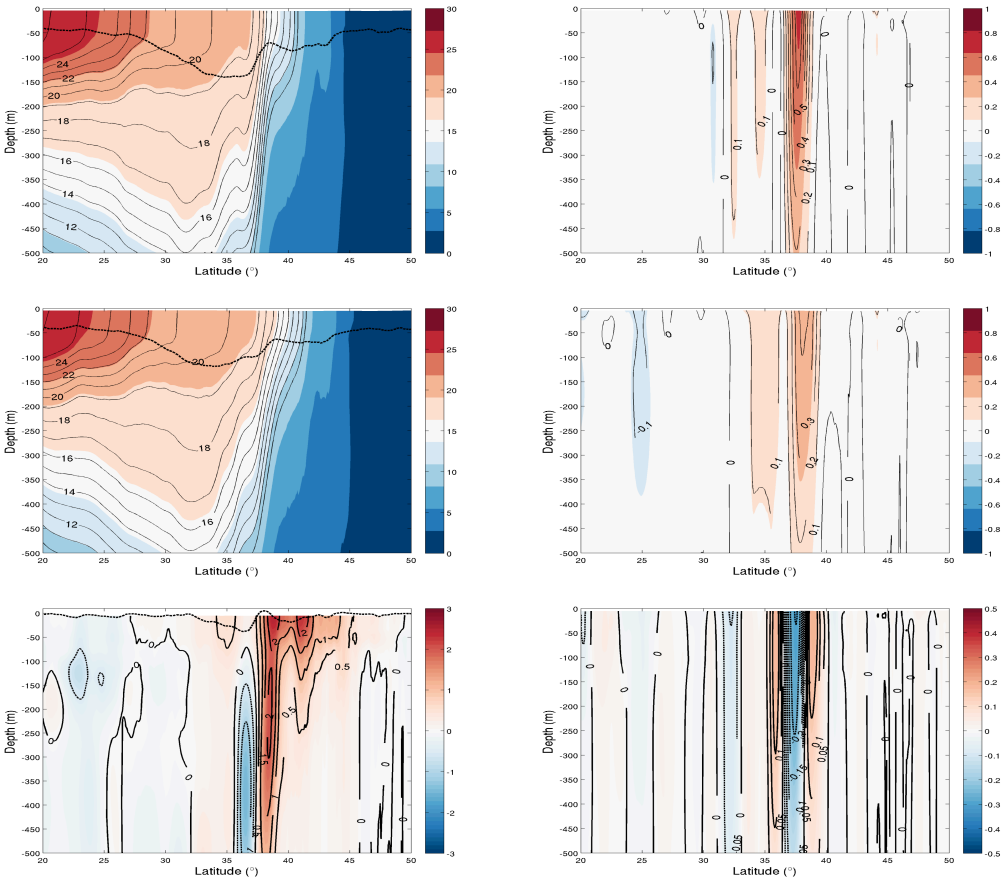


Figure 43. Vertical profile of zonal averaged winter season mean temperature (°C, contour and shaded, left) overlaid by MLD (m, thick dashed line) and zonal velocity U (contour and shaded, m/s) in the KER in CTRL (top), CPL-MEFS (middle) and the difference between CPL-MEFS and CTRL (bottom) in 9km CRCM simulations. The zonal average is taken from 140°E to 180°E. For the difference figures, positive values are plotted in solid contours and negative values in dashed contours.

In summary, based on the comparison between CTRL and CPL-MEFS, we demonstrate that the ocean-eddy induced meso-scale atmosphere response can feedback onto the ocean circulations along the KER, causing changes in SST, life span of meso-scale oceanic eddies, MLD, as well as Kuroshio strength and its cross-front temperature gradient. We propose an ocean-eddy induced diffusion mechanism to explain changes in

Kuroshio strength and its cross-front temperature gradient. If this mechanism holds true, it suggests that the coupling between ocean-eddy induced meso-scale SST variability and the atmosphere is crucial in maintaining the sharp temperature gradient along the KER, which in turns has an anchoring effect on the North Pacific storm track.

**4.5 Summary**

In this chapter, meso-scale air-sea interactions during winter season (NDJFM) in the KER are investigated using a high-resolution (9 km) CRCM. Three sets of numerical experiments, CTRL, UNCPL-MEFS and CPL-MEFS, are carried out to understand various aspects of the frontal-scale air-sea interaction. A comparison between CTRL and UNCPL-MEFS sheds light onto local and remote influences of meso-scale oceanic eddies on the atmosphere. The results support the model outcomes in the Chapter III that meso-scale oceanic eddies can have a significant influence on not only local atmospheric boundary response, but also storm track and jet stream positions that produce a significant impact on rainfall patterns along the USWC. A result that differs from the previous low-resolution (27 km) WRF simulations is the much stronger precipitation and storm genesis response to meso-scale oceanic eddies in the western and central North Pacific in the high-resolution WRF simulation. We conjecture that this difference may be attributed to the stronger diabatic heating response to oceanic eddies in the high-resolution WRF.

The feedback of ocean-eddy induced atmospheric response onto the ocean is investigated by comparing CTRL to CPL-MEFS. In the CPL-MEFS, the suppression of ocean-eddy effect on the atmosphere results in a significant surface warming north of the

Kuroshio Front. We attribute this surface warming to the lack of damping effect of the atmosphere on warm ocean eddies. We further show that the ocean-eddy induced atmospheric response can feedback onto Kuroshio strength and its cross-front temperature gradient. Removing the ocean-eddy induced atmospheric response in CPL-MEFS results in a weaker Kuroshio and a weaker cross-front temperature gradient. We propose that the weakened Kuroshio strength and its cross-front temperature gradient can be explained by the lack of atmospheric damping effects on ocean eddies, which leads to a stronger eddy-induced diffusion effect on the Kuroshio front. The validity of this hypothesis needs to be further examined.

# CHAPTER V

# CONCLUSIONS AND FUTURE WORK

Frontal-scale air-sea interactions during boreal winter season in the KER in the North Pacific sector are investigated in this dissertation from three perspectives. First, extreme flux events associated with CAOs in boreal winter (NDJFM) in the KER are analyzed and compared to those in the GSR using different reanalysis data sets. The relationship between the extreme heat flux events and modes of climate variability in the North Pacific and North Atlantic and the potential influence from the underlying ocean are explored. Second, using a stand-alone WRF model with 27 km horizontal resolution, two ensembles of simulations forced by a high-resolution observed SST (CTRL) and a low-pass filtered SST (MEFS), respectively, were conducted for winter season (ONDJFM) in the North Pacific to quantify and understand the local and remote influence of meso-scale oceanic eddies on the atmosphere. Third, using a high-resolution eddy resolving CRCM at 9 km horizontal resolution, three sets of boreal winter season simulations were performed using different treatment in the modeled SST field (CTRL, UNCPL-MEFS and CPL-MEFS) to examine the effect of model resolutions on the atmospheric response to meso-scale oceanic eddies and to shed light on the feedback of ocean-eddy induced atmospheric response onto the ocean. The main conclusions of this dissertation research are summarized as follows.

## 5.1 Conclusions

Extreme flux events in the KER and GSR, which typically last fewer than 3 days,

are closely related to winter season synoptic-scale atmospheric storms and contribute significantly to the total variance of THF in the boreal winter season. Composite analysis shows that event days are characterized by "cold storms" with strong northerlies that bring cold and dry air from the Eurasian/North American continent to the warm WBC regions. Non-event days are characterized by "warm storms" with the opposite pattern that brings warm and moist air from the subtropics to the KER and GSR. A tangible relationship between the extreme flux events in the KER/GSR and the PDO/EAP in the North Pacific/Atlantic are identified. The positive PDO/EAP phase can be reconstructed by the integrated SLP anomalies accompanying extreme flux events during storm life cycles, pointing to the importance of the synoptic storms in determining the mode of climate variability in the North Pacific/Atlantic. Storms associated with the extreme flux events tend to propagate southeastward in both the North Pacific and Atlantic sectors, consistent with a southward shift of the storm tracks during positive PDO/EAP phase. A potential positive SST influence on the occurrence of extreme flux events is implicated in the North Pacific, but is lacking in the North Atlantic.

The WRF (27km) model correctly reproduces the intensity and position of rainfall and storm tracks as well as the positive correlation between meso-scale SST and surface wind, giving us confidence to use it to study the local and remote influence of meso-scale oceanic eddies on the atmosphere. Comparisons between CTRL forced by the observed high-resolution SST and MEFS forced by the low-pass filtered SST reveal that more than 80% of SST variance due to meso-scale oceanic eddies is removed in the KER in MEFS, resulting in a significant decrease of meso-scale atmospheric energy

within the boundary layer locally along the KER, including 30% decrease of THF and 10% decrease of PBLH. The removal of the meso-scale oceanic eddies in MEFS also cause a deep troposphere response along and downstream of the KER, including 1) a significant decrease (increase) of winter season mean rainfall along the KER (USWC); 2) a reduction of storm growth rate in the KER and an increase in storm wavelength; 3) a southward shift of midlatitude jet streams and storm tracks downstream in the eastern North Pacific. The change of rainfall and storm growth rate in response to meso-scale oceanic eddies is verified in observations and reanalysis dataset. A mechanism relating to moist baroclinic instability is proposed to explain the effect of meso-scale oceanic eddies in the KER on the atmosphere. Specifically, it is argued that meso-scale oceanic eddies can modify the baroclinic instability by changing static stability and latent heat release in the atmosphere, which affects the storm genesis in the KER. The storm track change modifies the downstream jet stream through eddy-mean flow interaction. The downstream jet stream change is likely to further feed back positively onto storm track development in the eastern North Pacific.

Similar to the analysis of the high-resolution observed SST, applying the same Loess filter to the simulated SST by the 9 km high-resolution CRCM revealed that more than 80% of the simulated winter season SST variability is explained by meso-scale oceanic eddies. Filtering this meso-scale SST variability in UNCPL-MEFS leads to a more significant decrease in meso-scale energy within the atmosphere boundary layer in the KER, including a 60% (20%) decrease in THF (PBL) variance, than in the 27 km WRF simulations. Similar but more enhanced deep troposphere response is observed in

the 9 km WRF simulations than in the 27 km WRF simulation, confirming the findings described in Chapter III. Comparisons between CTRL and CPL-MEFS suggest that at meso-scales the ocean-eddy forced atmospheric response can have a significant feedback onto the SST, mixed layer and the Kuroshio. Suppression of meso-scale SST influences on the atmosphere at each coupled time step in CPL-MEFS results in a significant surface warming in the KER due to the weakened surface wind variability and surface THF as well as the reduced MLD. It was further found that the removal of. meso-scale SST influences on the atmosphere can lead to a reduced strength in the Kuroshio and the associated thermal front. Therefore, it is argued that frontal- and meso-scale air-sea interactions along the KE are critically important for the maintenance of the Kuroshio front and thus its anchoring effect on the North Pacific storm track.

**5.2 Future Work**

The tangible relationship between the extreme flux events over the KER and GSR and the PDO in the North Pacific and the EAP in the North Atlantic, respectively, suggests a potential connection between extreme flux events in the KER/GSR and blocking activity in the North Pacific/Atlantic, as the PDO and EAP, as well as the southward shift of storm tracks, are shown to be linked to Pacific and Atlantic-Euro blocking activities (e.g., Croci-Maspoli et al., 2007). Future studies are needed to quantify the connection between extreme flux events in the KER/GSR and blocking activity in the North Pacific/Atlantic.

No solid connections between SST and extreme flux events along the WBCs are found, especially in the GSR. This may be partially due to the coarse resolution of

datasets used in the analyses that cannot adequately resolve the frontal structures. Future studies that consider the effect of meso-scale oceanic eddies and SST gradients across the fronts on the atmosphere need to further address the underlying dynamics governing interactions between SST and THF in the WBC regions.

Based on he WRF simulations discussed in Chapter III and IV, we conjectured that moist baroclinic instability may be the underlying mechanism responsible for the effect of meso-scale ocean eddies on the local and remote atmospheric response. This conjecture needs to be validated by performing more detailed analyses on the effect of diabatic heating on cyclogenesis in the framework of PV dynamics. In particular, it will be useful to track and compared individual winter cyclone development in the high-resolution model simulations with and without meso-scale oceanic eddy influence to understand the role of diabatic heating in the formation and intensification of winter cyclones and their tracks. Such analyses will shed further light on the role of moist baroclinic instability as a linking mechanism between meso-scale oceanic eddies and storm genesis along the KER and GSR.

Finally, many questions remain to be addressed concerning how ocean-eddy forced atmospheric response can feedback onto the ocean. The comparison between CRCM CTRL and CPL-MEFS shows a prominent surface warming in the KER and we attributed this warming to the lack of negative feedback between warm eddies and surface heat fluxes in CPL-MEFS. However, similar mechanism does not seem to operate for cold eddies. Future studies are needed to understand the asymmetry between atmospheric feedback on warm and cold oceanic eddies. Furthermore, more modeling

analyses are needed to further understand the local atmospheric feedback on the Kuroshio. In particular, the hypothesis that frontal- and meso-scale air-sea interactions along the KE are critically important for the maintenance of the Kuroshio front needs to be further tested.

# REFERENCES

Ahmadi-Givi, F., 2002: A review of the role of latent heat release in extratropical cyclones within potential vorticity framework. Journal of the Earth and Space Physics, 28, 7-20.

Alexander, M., 1992(a): Midlatitude atmosphere-ocean interaction during E1 Nifio. I. The North Pacific Ocean. Journal of Climate, 5, 944-958.

Alexander, M., 1992(b): Midlatitude atmosphere-ocean interaction during E1 Nifio. II. The Northern Hemisphere atmosphere. Journal of Climate, 5, 959-972.

Alexander, M., and Coauthors, 2006: Extratropical atmosphere-ocean variability in CCSM3. Journal of Climate, 19, 2492-2521.

Alexander, M., and J. D. Scott, 1997: Surface flux variability over the North Pacific and North Atlantic Oceans. Journal of Climate, 10, 2963-2978.

Alexander, M., I. Blade, M. Newman, J. R. Lanzante, N.-C. Lau, and J. D. Scott, 2002: The atmospheric bridge: The influence of ENSO teleconnections on air-sea interaction over the global oceans. Journal of Climate, 15, 2205-2231.

Atlas, R., R. N. Hoffman, J. Ardizzone, S. M. Leidner, J. C. Jusem, D. K. Smith, and D. Gombos, 2011: A cross-calibrated, multiplatform ocean surface wind velocity product for meteorological and oceanographic applications. Bulletin of the American Meteorological Society, 92, 157-174.

Balasubramanian, G., and M. K. Yau, 1994: The effects of convection on a simulated marine cyclone. Journal of the Atmospheric Sciences, 51, 2397-2417.

Barnett, T. P., 1981: On the nature and causes of large-scale thermal variability in the central North Pacific Ocean. Journal of Physical Oceanography, 11, 887-904.

Barnston, A. G., and R. E. Livezey, 1987: Classification, seasonality and persistence of low frequency atmospheric circulation patterns. Monthly Weather Review, 115, 1083-

1126.

Barsugli, J. J., and D. S. Battisti, 1998: The basic effects of atmosphere-ocean thermal coupling on midlatitude variability. Journal of the Atmospheric Sciences, 55(4), 477-493.

Bauer, M., and A. Del Genio, 2005: Composite analysis of winter cyclones in a GCM: influence on climatological humidity. Journal of Climate, 19, 1652-1672.

Benedict, J. J., S. Lee, and S. B. Feldstein, 2004: Synoptic view of the North Atlantic Oscillation. Journal of the Atmospheric Sciences, 61, 121-144.

Berrisford, P., D. Dee, K. Fielding, M. Fuentes, P. Kallberg, S. Kobayashi and S. Uppala, 2009: The ERA-Interim archive. ERA Report Series, 1.

Bjerknes, J., 1964: Atlantic air-sea interaction. Advances in Geophysics, 10, 1-82.

Bond, N. A., and M. F. Cronin, 2008: Regional weather patterns during anomalous air-sea fluxes at the Kuroshio Extension Observatory (KEO). Journal of Climate, 21, 1680-1697.

Booth, J. F., L. A. Thompson, J. Patoux, K. A. Kelly, and S. Dickinson, 2010: The signature of the midlatitude tropospheric storm tracks in the surface winds. Journal of Climate, 23, 1160-1174.

Brayshaw, D. J., B. J. Hoskins, and M. Blackburn, 2008: The storm track response to idealized SST perturbations in an aquaplanet GCM. Journal of the Atmospheric Sciences, 65, 2842-2860.

Bretherton, C., C. Smith, and J. Wallace, 1992: An intercomparison of methods to find coupled patterns in climate data. Journal of Climate, 5, 541-560.

Bryan, F. O., R. Tomas, J. M. Dennis, D. B. Chelton, N. G. Loeb, and J. L. McClean, 2010: Frontal-scale air-sea interaction in high-resolution coupled climate models. Journal of Climate, 23, 6277-6291.

Cayan, D. R., 1992: Latent and sensible heat-flux anomalies over the northern oceans: The connection to monthly atmospheric circulation. Journal of Climate, 5, 354-369.

Cayan, D. R., and D. H. Peterson, 1989: The influence of North Pacific atmospheric circulation on streamflow in the west. Geophysical Monograph, 55, 3-23.

Chang, E. K. M., S. Lee, and K. L. Swanson, 2002: Storm track dynamics. Journal of Climate, 15, 2163-2183.

Chang, E. K. M., 2007: Assessing the increasing trend in Northern Hemisphere winter storm track activity using surface ship observations and a statistical storm track model. Journal of Climate, 20, 5607-5628.

Chang, E. K. M., 2009: Are band-pass variance statistics useful measures of storm track activity? Re-examining storm track variability associated with the NAO using multiple storm track measures. Climate Dynamics, 33, 277-296.

Chang, E. K. M. and Y. Fu, 2002: Interdecadal variations in Northern Hemi-sphere winter storm track intensity. Journal of Climate, 15, 642-658.

Charney, J. G., 1947: The dynamics of the long waves in a baroclinic westerly current. Journal of Meteorology, 4, 135-165.

Chelton, D. B., and Coauthors, 2001: Observations of coupling between surface wind stress and sea surface temperature in the eastern tropical Pacific. Journal of Climate, 14, 1479-1498.

Chelton, D. B., M. G. Schlax, M. H. Freilich, R. F. Milliff, 2004: Satellite measurements reveal persistent small-scale features in ocean winds. Science, 303, 978-983.

Chelton, D. B., M. G. Schlax, and R. M. Samelson, 2007: Summertime coupling between sea surface temperature and wind stress in the California Current System. Journal of Physical Oceanography, 37, 495-517.

Chelton, D. B., M. H. Freilich, J. M. Sienkiewicz, and J. M. Von Ahn, 2006: On the use of QuikSCAT scatterometer measurements of surface winds for marine weather predictions. Monthly Weather Review, 134, 2055-2071.

Chelton, D. B. and S.-P. Xie, 2010: Coupled ocean-atmosphere interactionat oceanic mesoscales. Oceanography, 23(4), 52-69.

Chhak, K. C., E. Di Lorenzo, N. Schneider, and P. F. Cummins, 2009: Forcing of low-frequency ocean variability in the Northeast Pacific. Journal of Climate, 22(5), 1255-1276.

Chou, M.-D., and M. J. Suarez, 1994: An efficient thermal infrared radiation parameterization for use in general circulation models. NASA Technical Memorandum, 104606, 3, 84.

Colucci, J., and J. C. Davenport, 1987: Rapid surface anticyclogenesis: Synoptic climatology and attendant large scale circulation changes. Monthly Weather Review, 115, 822-836.

Compo, G. P., and Coauthors, 2011: The Twentieth Century Reanalysis Project. Quarterly Journal of the Royal Meteorological Society, 137, 1-28.

Craig, G. C., and H. R. Cho, 1988: Cumulus heating and CISK in the extratropical atmosphere. Part I: Polar lows and comma clouds. Journal of the Atmospheric Sciences, 45, 2622-2640.

Croci-Maspoli, M., C. Schwierz, and H. Davies, 2007: Atmospheric blocking: Space-time links to the NAO and PNA. Climate Dynamics, 29, 713-725.

Cronin, M. F., S. P. Xie, H. Hashizume, 2003: Barometric pressure variations associated with Eastern Pacific Tropical Instability Waves. Journal of Climate, 16, 3050-3057.

Davis, C. A., D. G. E. D. Grell, and M. A. Shapiro, 1996: The balanced dynamical nature of a rapidly intensifying oceanic cyclone. Monthly Weather Review, 124, 3-26.

Davis, C. A., and K. A. Emanuel, 1991: Potential vorticity diagnostics of cyclogenesis. Monthly Weather Review, 119, 1929-1953.

Davis, C. A., M. T. Stoelinga, and Y.-H. Kuo, 1993: The integrated effect of condensation in numerical simulations of extratropical cyclogenesis. Monthly Weather Review, 121, 2309-2330.

Davis, R. E., 1976: Predictability of sea surface temperature and sea level pressure anomalies over the North Pacific Ocean. Journal of Physical Oceanography, 6, 249-266.

Davis, R. E., 1978: Predictability of sea level pressure anomalies over the North Pacific Ocean. Journal of Physical Oceanography, 8, 233-246.

Deser, C., and M. L. Blackmon, 1993: Surface climate variations over the North Atlantic Ocean during winter: 1900-1989. Journal of Climate, 6, 1743-1753.

Deser, C., and M. S. Timlin, 1997: Atmosphere-ocean interaction on weekly timescales in the North Atlantic and Pacific. Journal of Climate, 10, 393-408.

Di Lorenzo, E., and Coauthors, 2008: North Pacific Gyre Oscillation links ocean climate and ecosystem change. Geophysical Research Letters, 35, L08607, doi:10.1029/2007GL032838.

Dong, B., R. T. Sutton, T. Woollings, and K. Hodges, 2013: Variability of the North Atlantic summer storm track: mechanisms and impacts on European climate. Environmental Research Letters, 8, 034037, doi:10.1088/1748-9326/8/3/034037.

Ducet N., PY. Le Traon, G. Reverdin, 2000: Global high-resolution mapping of ocean circulation from TOPEX/Poseidon and ERS-1 and-2. Journal of Geophysical Research-Oceans, 105, 19477-19498.

Eady, E. T., 1949: Long waves and cyclone waves. Tellus, 1, 33-52.

Emanuel, K. A., M. Fantini, and A. J. Thorpe, 1987: Baroclinic instability in an

environment of small stability to slantwise moist convection. Part I: Two-dimensional models. Journal of the Atmospheric Sciences, 44, 1559-1573.

Fairall, C., E. Bradley, D. Rogers, J. Edson, and G. Young, 1996: Bulk parameterization of air-sea fluxes for tropical ocean-global atmosphere coupled-ocean atmosphere response experiment. Journal of Geophysical Research, 101(C2), 3747-3764.

Fairall, C. W., E. F. Bradley, J. E. Hare, A. A. Grachev, and J. B. Edson, 2003: Bulk parameterization of air-sea fluxes: Updates and verification for the COARE algorithm. Journal of Climate, 16, 571-591.

Feldstein, S. B., 2000: The timescale, power spectra and climate noise properties of teleconnections patterns. Journal of Climate, 13, 4430-4440.

Feldstein, S. B., 2003: The dynamics of NAO teleconnection pattern growth and decay. Quarterly Journal of the Royal Meteorological Society, 129, 901-924.

Fehlmann, R., and H. C. Davies, 1999: Role of salient PV-elements in an event of frontal-wave cyclogenesis. Quarterly Journal of the Royal Meteorological Society, 125, 1801-1824.

Frankignoul, C., 1985: Sea surface temperature anomalies, planetary waves and air–sea feedback in the middle latitudes. Reviews of Geophysics, 23, 357-390.

Frankignoul, C. and K. Hasselmann, 1977: Stochastic climate models. Part II, Application to sea-surface temperature anomalies and thermocline variability. Tellus, 29, 289-305.

Frankignoul, C., A. Czaja, and B. L'Heveder, 1998: Air-sea feedback in the North Atlantic and surface boundary conditions for ocean models. Journal of Climate, 11, 2310-2324.

Frankignoul, C., and N. Sennechael, 2007: Observed influence of North Pacific SST anomalies on the atmospheric circulation. Journal of Climate, 20, 592-606.

Frankignoul, C., N. Sennechael, Y.-O. Kwon, and M. A. Alexander, 2011: Influence of the meridional shifts of the Kuroshio and the Oyashio Extensions on the atmospheric circulation. Journal of Climate, 24, 762-777.

Frenger, I., N. Gruber, R. Knutti, and M. Munnich, 2013: Imprint of Southern Ocean eddies on winds, clouds and rainfall. Nature Geoscience, 6, 608-612.

Gaffney, S., A. Robertson, P. Smyth, S. Camargo, and M. Ghil, 2007: Probabilistic clustering of extratropical cyclones using regression mixture models. Climate Dynamics, 29, 423-440.

Geng, Q., and M. Sugi, 2003: Possible change of extratropical cyclone activity due to enhanced greenhouse gases and sulfate aerosols study with a high-resolution AGCM. Journal of Climate, 16, 2262-2274.

Guo, X., H. Hukuda, Y. Miyazawa, and T. Yamagata, 2003: A triply nested ocean model for simulating the Kuroshio roles of horizontal resolution on JEBAR. Journal of Physical Oceanography, 33, 146-167.

Hakkinen, S., P. B. Rhines, and D. L. Worthen, 2011: Atmospheric blocking and Atlantic multidecadal ocean variability. Science, 334, 655-659.

Hamilton, K., R. J. Wilson, J. D. Mahlman and L. J. Umscheid, 1995: Climatology of the SKYHI troposphere-stratosphere-mesosphere General Circulation Model. Journal of the Atmospheric Sciences, 52, 5-43.

Hamilton, K., 2008: Numerical resolution and modeling of the global atmospheric circulation: A review of our current understanding and outstanding issues. High resolution numerical modeling of the atmosphere and ocean, Spinger, 7-27.

Hanawa, K., and L. D. Talley, 2001: Mode waters. Ocean Circulation and Climate, International Geophysics Series, 77, 373-386.

Harnik N., and E. K. M. Chang, 2003: Storm track variations as seen in radiosonde observations and reanalysis data. Journal of Climate, 16, 480-495.

Hasselmann, K., 1976: Stochastic climate models. Part I, theory. Tellus, 28, 473-485.

Hatzaki, M., H. A. Flocas, C. Oikonomou, and C. Giannakopoulos, 2010: Future changes in the relationship of precipitation intensity in Eastern Mediterranean with large scale circulation. Advances in Geoscience, 23, 31-36.

Hong, S.-Y., and H.-L. Pan, 1996: Nonlocal boundary layer vertical diffusion in a medium-range forecast model. Monthly Weather Review, 124, 2322-2339.

Hoskins, B. J., I. N. James, and G. H. White, 1983: The shape, propagation and mean-flow interaction of large-scale weather. Journal of the Atmospheric Sciences, 40, 1595-1612.

Hoskins, B. J., and K. I. Hodges, 2002: New perspectives on the Northern Hemisphere winter storm tracks. Journal of the Atmospheric Sciences, 59, 1041-1061.

Hoskins, B. J., M. E. McIntyre, and A. W. Robertson, 1985: On the use and significance of isentropic potential vorticity maps. Quarterly Journal of the Royal Meteorological Society, 111, 877-946.

Hoskins, B. J., and P. J. Valdes, 1990: On the existence of storm tracks. Journal of the Atmospheric Sciences, 47, 1854-1864.

Hurrell, J. W., Y. Kushnir, M. Visbeck, and G. Ottersen, 2003: An overview of the North Atlantic Oscillation. The North Atlantic Oscillation, Climatic Significance and Environmental Impact. AGU Geophysical Monograph, 134, 1-35.

Hurrell, J. W., and H. van Loon, 1997: Decadal variations in climate associated with the North Atlantic oscillation. Climatic Change, 36, 301-326.

Hurrell, J. W., and C. Deser, 2009: North Atlantic climate variability: The role of the North Atlantic Oscillation. Journal of Marine Systems, 78, 28-41.

Joyce, T. M, C. Deser, and M. A. Spall, 2000: The relation between decadal variability

of Subtropical Mode Water and the North Atlantic Oscillation. Journal of Climate, 13, 2550-2569.

Joyce, T. M., Y.-O. Kwon, and L. Yu, 2009: On the relationship between synoptic wintertime atmospheric variability and path shifts in the Gulf Stream and the Kuroshio Extension. Journal of Climate, 22, 3177-3192.

Kagimoto, T. and T. Yamagata, 1997: Seasonal transport variations of the Kuroshio: An OGCM simulation. Journal of Physical Oceanography, 27(3), 403-418.

Kalnay, E., and Coauthors, 1996: The NCEP/NCAR 40-Year Reanalysis Project. Bulletin of the American Meteorological Society, 77, 437-471.

Kanamitsu, M., W. Ebisuzaki, J. Woollen, S.-K. Yang, J. J. Hnilo, M. Fiorino, and G. L. Potter, 2002: NCEP-DOE AMIP-II Reanalysis (R-2). Bulletin of the American Meteorological Society, 83, 1631-1643.

Kelly, K. A., R. J. Small, R. M. Samelson, B. Qiu, T. Joyce, Y.-O. Kwon, and M. F. Cronin, 2010: Western boundary currents and frontal air-sea interaction: Gulf Stream and Kuroshio Extension. Journal of Climate, 23, 5644-5667.

Kelly, K. A., and S. Dong, 2004: The relationship of western boundary current heat transport and storage to mid-latitude ocean atmosphere interaction. Earth Climate: The Ocean-Atmosphere Interaction. AGU Geophysical Monograph, 147, 347–363.

Kobayashi, C. and M. Sugi, 2004: Impact of horizontal resolution on the simulation of the Asian summer monsoon and tropical cyclones in the JMA global model. Climate Dynamics, 23, 165-176.

Kushnir, Y., W. A. Robinson, I. Bladé, N. M. Hall, S. Peng, and R. Sutton, 2002: Atmospheric GCM response to extratropical SST anomalies: Synthesis and evaluation. Journal of Climate, 15, 2233-2255.

Kwon, B.-H. and Coauthors, 1998: Structure of the marine atmospheric boundary layer over an oceanic thermal front: SEMAPHORE experiment. Journal of Geophysical

Research, 103, 25159-25180.

Kwon, Y.-O, M., A. Alexander, N. A. Bond, C. Frankignoul, H. Nakamura, B. Qiu, and L. A. Thompson, 2010: Role of the Gulf Stream and Kuroshio-Oyashio systems in large-scale atmosphere-ocean interaction: A review. Journal of Climate, 23, 3249-3281.

Kwon, Y.-O, M. and T. Joyce, 2013: Northern Hemisphere Winter Atmospheric Transient Eddy Heat Fluxes and the Gulf Stream and Kuroshio-Oyashio Extension Variability. Journal of Climate, 26, 9839–9859.

Lambert, S. J., 1995: The effect of enhanced greenhouse warming on winter cyclone frequencies and strengths. Journal of Climate, 8, 1447-1452.

Lamberts, S. J., G. Lapeyre, and V. Zeitlin, 2012: Moist versus dry baroclinic instability in a simplified two-layer atmospheric with condensation and latent heat release. J. Atmos. Sci., 69, 1405-1426.

Lapeyre, G., and I. M. Held, 2004: The role of moisture in the dynamics and energetics of turbulent baroclinic eddies. Journal of the Atmospheric Sciences, 61, 1693-1710.

Large, W. G., and G. Danabasoglu, 2006: Attribution and impacts of upper-ocean biases in CCSM3. Journal of Climate, 19, 2325-2346.

Large, W. G., J. C. Mcwilliams, and S. C. Doney, 1994: Oceanic vertical mixing: A review and a model with a nonlocal boundary-layer parameterization. Reviews of Geophysics, 32, 363-403.

Latif, M., 1998: Dynamics of interdecadal variability in coupled ocean−atmosphere models. Journal of Climate, 11, 602-624.

Latif, M., and T. P. Barnett, 1994: Causes of decadal climate variability over the North Pacific and North America sector. Science, 266, 634-637.

Latif, M., and T. P. Barnett, 1996: Decadal climate variability over the North Pacific and

North America: Dynamics and predictability. Journal of Climate, 9, 2407-2423.

Lee, S. S., J. Y. Lee, B. Wang, KJ. Ha, KY. Heo, FF. Jin, D. M. Straus and J. Shukla, 2011: Interdecadal changes in the storm track activity over the North Pacific and North Atlantic. Climate Dynamics, 39, 313-327.

Leung, L. R., Y.-H. Kuo, and J. Tribbia, 2006: Research Needs and Directions of Regional Climate Modeling Using WRF and CCSM. Bulletin of the American Meteorological Society, 87, 1747-1751.

Lin, Y.-L., R. D. Farley, and H. D. Orville, 1983: Bulk parameterization of the snow field in a cloud model. Journal of Climate and Applied Meteorology, 22, 1065-1092.

Lindzen, R. S., and B. Farrell, 1980: A simple approximate result for the maximum growth rate of baroclinic instabilities. Journal of the Atmospheric Sciences, 37, 1648-1654.

Lindzen, R. S., and S. Nigam, 1987: On the role of sea surface temperature gradients in forcing low level winds and convergence in the tropics. Journal of the Atmospheric Sciences, 44, 2418-2436.

Linkin, M. E., and S. Nigam, 2008: The North Pacific Oscillation-West Pacific Teleconnection Pattern: Mature-Phase Structure and Winter Impacts. Journal of Climate, 21, 1979–1997.

Lorenz, D. J., and E. T. DeWeaver, 2007: Tropopause height and zonal wind response to global warming in the IPCC scenario integrations. Journal of Geophysical Research, 112, D10119, doi:10.1029/2006JD008087.

Maidens, A., A. Arribas, A. A. Scaife, C. MacLachlan, D. Peterson, and J. Knight, 2013： The influence of surface forcings on prediction of the North Atlantic Oscillation regime of winter 2010-11. Monthly Weather Review, 141, 3801-3813.

Mahoney, K. M., and G. M. Lackmann, 2007: The effect of upstream convection on downstream precipitation. Weather Forecasting, 22, 255-277.

Maloney, E. D., and D. B. Chelton, 2006: An assessment of the sea surface temperature influence on surface wind stress in numerical weather prediction and climate models. Journal of Climate, 19, 2743-2762.

Mantua, N. J., S. R. Hare, Y. Zhang, J. M. Wallace, R. Francis, 1997: A Pacific interdecadal climate oscillation with impacts on salmon production. Bulletin of the American Meteorological Society, 78(6), 1069-1079.

Marshall, J., Y. Kushnir, D. Battisti, P. Chang, A. Czaja, R. Dickson, J. Hurrell, M. McCartney, R. Saravanan, and M .Visbeck, 2001: North Atlantic climate variability, phenomena, impacts and mechanisms. International Journal of Climatology, 21, 1863-1898.

McCabe, G. J., M. P. Clark, and M. C. Serreze, 2001: Trends in Northern Hemisphere surface cyclone frequency and intensity. Journal of Climate, 14, 2763-2768.

Miller, A. J., D. R. Cayan, T. P. Barnett, N. E. Graham, and J. M. Oberhuber, 1994: The 1976-77 climate shift of the Pacific Ocean. Oceanography, 7, 21-26.

Miller, A. J., F. Chai, S. Chiba, J. R. Moisan, and D. J. Neilson, 2004: Decadal-scale climate and ecosystem interactions in the North Pacific Ocean. Journal of Oceanography, 60(1), 163-188.

Miller, A. J., and N. Schneider, 2000: Interdecadal climate regime dynamics in the North Pacific Ocean: Theories, observations and ecosystem impacts. Progress in Oceanography, 47, 355-379.

Minobe, S., A. Kuwano-Yoshida, N. Komori, S. P. Xie, and R. J. Small, 2008: Influence of the Gulf Stream on the troposphere. Nature, 452, 206-209.

Minobe, S., N. Schneider, C. Deser, Z. Liu, N. Mantua, H. Nakamura, and M. Nonaka, 2004: Pacific Decadal Variability: A Review. In First International CLIVAR Conference, Baltimore, MD, USA.

Mlawer, E. J., S. J. Taubman, P. D. Brown, M. J. Iacono, and S. A. Clough, 1997:

Radiative transfer for inhomogeneous atmospheres: RRTM, a validated correlated-k model for the longwave. Journal of Geophysical Research, 102(D14), 16663-16682.

Montgomery, M. T., and B. F. Farrell, 1991: Moist surface frontogenesis associated with interior potential vorticity anomalies in a semigeostrophic model. Journal of the Atmospheric Sciences, 48, 343-368.

Muller, P., and C. Frankignoul, 1981: Direct atmospheric forcing ofgeostrophic eddies. Journal of Physical Oceanography, 11, 287-308.

Nakamura, H., 1996: Year-to-year and interdecadal variability in the activity of intraseasonal fluctuations in the Northern Hemisphere wintertime circulation. Theoretical and Applied Climatology, 55, 19-32.

Nakamura, H., G. Lin, and T. Yamagata, 1997: Decadal climate variability in the North Pacific during recent decades. Bulletin of the American Meteorological Society, 78, 2215-2225.

Nakamura, H., and A. S. Kazmin, 2003: Decadal change in the North Pacific oceanic frontal zones as revealed in ship and satellite observation. Journal of Geophysical Research, 108, 3078, doi:10.1029/1999JC000085.

Nakamura, H., T. Izumi, and T. Sampe, 2002: Interannual and decadal modulation recently observed in the North Pacific storm track activity and east Asian winter monsoon. Journal of Climate, 15, 1855-1874.

Nakamura, H., T. Sampe, Y. Tanimoto, and A. Shimpo, 2004: Observed associations among storm tracks, jet streams, and midlatitude oceanic fronts. Earth Climate: The Ocean-Atmosphere Interaction. AGU Geophysical Monograph, 147, 329-345.

Nakamura, H., T. Sampe, A. Goto, W. Ohfuchi, and S.-P. Xie, 2008: On the importance of midlatitude oceanic frontal zones for the mean state and dominant variability in the tropospheric circulation. Geophysical Research Letters, 35, L15709, doi:10.1029/2008GL034010.

Nakamura, M., and S. Yamane, 2009: Dominant anomaly patterns in the near-surface baroclinicity and accompanying anomalies in the atmosphere and the oceans. Part I: North Atlantic basin. Journal of Climate, 22, 880-904.

Nakamura, M., and S. Yamane, 2010: Dominant anomaly patterns in the near-surface baroclinicity and accompanying anomalies in the atmosphere and the oceans. Part II: North Pacific basin. Journal of Climate, 23, 6445-6467.

Namias, J., 1959: Recent seasonal interaction between North Pacific waters and the overlying atmospheric circulation. Geophysical Research Letters, 64, 631-646.

Namias, J., 1972: Experiments in objectively predicting some atmospheric and oceanic variables for the winter of 1971-72. Journal of Applied Meteorology, 11, 1164-1174.

Newman, M., G. Compo, and M. Alexander, 2003: ENSO-forced variability of the Pacific decadal oscillation. Journal of Climate, 16(23), 3853-3857.

Nonaka, M., and S.-P. Xie, 2003: Co-variations of sea surface temperature and wind over the Kuroshio and its extension: Evidence for oceanto-atmospheric feedback. Journal of Climate, 16, 1404-1413.

O'Gorman, P. A, 2010: Understanding the varied response of the extratropical storm tracks to climate change. Proceedings of the National Academy of Sciences, 1071, 19176-19180.

Okumura, Y., S.-P. Xie, A . Numaguti, and Y. Tanimoto, 2001: Tropical Atlantic air-sea interaction and its influence on the NAO. Geophysical Research Letters. 28, 1507-1510.

O'Neill, L. W., D. B. Chelton, and S. K. Esbensen, 2012: Covariability of Surface Wind and Stress Responses to Sea Surface Temperature Fronts. Journal of Climate, 25, 5916-5942.

O'Neill, L.W., D. B. Chelton, S. K. Esbensen, and F. J. Wentz, 2005: High-resolution satellite measurements of the atmospheric boundary layer response to SST variations along the Agulhas Return Current. Journal of Climate, 18, 2706-2723.

O'Reilly, C. H., and A. Czaja, 2014: The response of the Pacific storm track and atmospheric circulation to Kuroshio Extension variability. Quarterly Journal of the Royal Meteorological Society, doi:10.1002/qj.2334.

Orlanski, I., 2008: The rationale for why climate models should adequately resolve the mesoscale. High Resolution Numerical Modeling of the Atmosphere and Ocean, Springer, 29-44.

Park, K.-A., P. C. Cornillon, and D. L. Codiga, 2006: Modification of surface winds near ocean fronts: Effects of Gulf Stream rings on scatterometer (QuikSCAT, NSCAT) wind observations. Geophysical Research Letters, 111, C03021, doi:10.1029/2005JC003016.

Parker, D. J., and A. J. Thorpe, 1995: Conditional convective heating in a baroclinic atmosphere: A model of convective frontogenesis. Journal of the Atmospheric Sciences, 52, 1699-1711.

Petterssen, S. and S. J. Smebye, 1971: On the development of extratropical cyclones. Quarterly Journal of the Royal Meteorological Society, 97, 457-482.

Pinto, J. G, M. Reyers, and U. Ulbrich, 2011: The variable link between PNA and NAO in observations and in multi-century CGCM simula-tions. Climate Dynamics, 36, 337-354.

Phillips, N. A., 1954: Energy transformations and meridional circulations associated with simple baroclinic waves in a twolevel, quasi-geostrophic model. Tellus, 6, 273-286.

Qiu B., S. Shen and P. Hacker, 2004: Synoptic-scale air-sea flux forcing in the western North Pacific: Observations and their im-pact on SST and the mixed layer. Journal of Physical Oceanography, 34, 2148-2159.

Qiu B., and S. Chen, 2005: Variability of the Kuroshio Extension Jet, recirculation gyre, and mesoscale eddies on decadal time scales. Journal of Physical Oceanography, 35, 2090-2103.

Qiu B., and S. Chen, 2006: Decadal variability in the formation of the North Pacific

subtropical mode water: Oceanic versus atmospheric control. Journal of Physical Oceanography, 36, 1365-1380.

Qiu B., and S. Chen, and P. Hacker, 2007: Effect of mesoscale eddies on subtropical mode water variability from the Kuroshio Extension System Study (KESS). Journal of Physical Oceanography, 37, 982-1000.

Robertson, A. W., 1996: Interdecadal variability over the North Pacific in a multi-century climate simulation. Climate Dynamics., 12, 227-241.

Rodwell, M. J., D. P. Rowell, and C. K. Folland, 1999: Oceanic forcing of the wintertime North Atlantic Oscillation and European climate. Nature, 398, 320-323.

Rogers, J. C., 1981: The North Pacific oscillation. Journal of Climate, 1, 39-57.

Rogers, J. C., 1990: Patterns of low-frequency monthly sea level pressure variability (1899–1986) and associated wave cyclone frequencies. Journal of Climate, 3, 1364-1379.

Rogers, J. C., 1997: North Atlantic storm track variability and its association with the North Atlantic Oscillation and climate variability of northern Europe. Journal of Climate, 10, 1635-1647.

Riviere, G., 2011: A dynamical interpretation of the poleward shift of the jet streams in global warming scenarios. Journal of the Atmospheric Sciences, 68, 1253-1272.

Riviere, G., and I. Orlanski, 2007: Characteristics of the Atlantic storm-track eddy activity and its relation with the North Atlantic Oscillation. Journal of the Atmospheric Sciences, 64,241-266.

Saha, S., and Coauthors, 2010: The NCEP Climate Forecast System Reanalysis. Bulletin of the American Meteorological Society, 91, 1015-1057.

Sampe, T., H. Nakamura, A. Goto, and W. Ohfuchi, 2010: Significance of a midlatitude SST frontal zone in the formation of a storm track and an eddy-driven westerly jet.

Journal of Climate, 23, 1793-1814.

Sampe, T., and S.-P. Xie, 2007: Mapping high sea winds from space. Bulletin of the American Meteorological Society, 88, 1965-1978.

Saravanan, R., 1998: Atmospheric low-frequency variability and its relationship to midlatitude SST variability: Studies using the NCAR Climate System Model. Journal of Climate, 11, 1386-1404.

Saravanan, R., G. Danabasoglu, S. C. Doney, and J. C. McWilliams, 2000: Decadal variability and predictability in the midlatitude ocean-atmosphere system. Journal of Climate, 13, 1073-1097.

Scherrer, S. C., M. Croci-Maspoli, C. Schwierz, and C. Appenzeller, 2006: Two-dimensional indices of atmospheric blocking and their statistical relationship with winter climate patterns in the Euro-Atlantic region. International Journal of Climatology, 26, 233-249.

Seager, R., Y. Kushnir, M. Visbeck, N. Naik, J. Miller, G. Krahmann, and H. Cullen, 2000: Causes of Atlantic Ocean climate variability between 1958 and 1998. Journal of Climate, 13, 2845-2862.

Seager, R., Y. Kushnir, N. H. Naik, M. A. Cane, and J. Miller, 2001: Wind-driven shifts in the latitude of the Kuroshio-Oyashio extension and generation of SST anomalies on decadal timescales. Journal of Climate, 14, 4249-4265.

Shaman, J., R. Samelson, and E. Skyllingstad, 2010: Air-Sea Fluxes Over the Gulf Stream Region: Atmospheric Controls and Trends. Journal of Climate, 23, 2651-2670.

Smagorinsky, J., 1963: General circulation experiments with the primitive equations. Monthly Weather Review, 91 (3), 99-164.

Small, R. J. and Coauthors, 2008: Air-sea interaction over ocean fronts and eddies. Dynamics of Atmospheres and Oceans, 45, 274-319.

Small, R. J., S.-P. Xie, and Y. Wang, 2003: Numerical simulation of atmospheric response to Pacific tropical instability waves. Journal of Climate, 16, 3723-3741.

Stammer, D., 1997: Global characteristics of ocean variability estimated from regional TOPEX/POSEIDON altimeter measurements. Journal of Physical Oceanography, 27, 1743-1769.

Snyder, C., and R. S. Lindzen, 1991: Quasigeostrophic wave-CISK in an unbounded baroclinic shear. Journal of the Atmospheric Sciences, 48, 76-86.

Spall, M. A., 2007: Midlatitude wind stress-sea surface temperature coupling in the vicinity of ocean fronts. Journal of Climate, 20, 3785-3801.

Sweet, W. R., R. Fett, J. Kerling, and P. La Violette, 1981: Air-sea interaction effects in the lower troposphere across the north wall of the Gulf Stream. Monthly Weather Review, 109, 1042-1052.

Taguchi, B., H. Nakamura, M. Nonaka, and S.-P. Xie, 2009: Influences of the Kuroshio-Oyashio Extensions on Air-Sea Heat Exchanges and Storm-Track Activity as Revealed in Regional Atmospheric Model Simulations for the 2003/04 Cold Season. Journal of Climate, 22, 6536-6560.

Taguchi, B., H. Nakamura, M. Nonaka, N. Komori, A. Kuwano-Yoshida, K. Takaya, and A. Goto, 2012: Seasonal evolutions of atmospheric response to decadal SST anomalies in the North Pacific subarctic frontal zone: Observations and a coupled model simulation. Journal of Climate, 25, 111-139.

Thompson, D. W., and J. M. Wallace, 1998: The Arctic Oscillation signature in the wintertime geopotential height and temperature fields. Geophysical Research Letters, 25(9), 1297-1300.

Thompson, L., and W. Cheng, 2008: Water masses in the Pacific in CCSM3. Journal of Climate, 21, 4514-4528.

Trenberth, K. E., and J. W. Hurrell, 1994: Decadal atmosphere-ocean varia-tions in the

Pacific. Climate Dynamics, 9, 303-319.

Vallis, G. K., E. P. Gerber, P. J. Kushner, and B. A. Cash, 2004: Amechanism and simple dynamical model of the North Atlantic Oscillation and annular modes. Journal of the Atmospheric Sciences, 61, 264–280.

Van Loon, H., and J. Rogers, 1978: The seesaw in winter temperature between Greenland and northern Europe. Part I: General description. Monthly Weather Review, 106, 296-310.

Vecchi, G. A., S.-P. Xie and A. Fischer, 2004: Ocean-atmosphere covariability in the western Arabian Sea. Journal of Climate, 17, 1213-1224.

Wai, M., and S. A. Stage, 1989: Dynamical analysis of marine atmospheric boundary layer structure near the Gulf Stream oceanic front. Quarterly Journal of the Royal Meteorological Society, 115, 29-44.

Wallace, J. M., T. P. Mitchell, and C. Deser, 1989: The influence of sea surface temperature on surface wind in the eastern equatorial Pacific: Seasonal and interannual variability. Journal of Climate, 2, 1492-1499.

Walsh, J., A. Phillips, D. H. Portis and A. L. Chapaman, 2001: Extreme Cold Outbreaks in the United States and Europe, 1948-99. Journal of Climate, 14, 2642-2658.
Warner, T. T., M. N. Lakhtakia, J. D. Doyle, and R. A. Pearson, 1990: Marine atmospheric boundary layer circulations forced by Gulf Stream sea surface temperature gradients. Monthly Weather Review, 118, 309-323.

Wheeler, D. D., V. L. Harvey, D. E. Atkinson, R. L. Collins, and M. J. Mills, 2011: A climatology of cold air outbreaks over North America: WACCM and ERA-40 comparison and analysis. Journal of Geophysical Research, 16, D12107.

White, W. B., and J. L. Annis, 2003: Coupling of extratropical mesoscale eddies in the ocean to westerly winds in the atmospheric boundary layer. Journal of Physical Oceanography, 33, 1095-1107.

Wilcoxon, F., 1945: Individual comparisons by ranking methods. Biometrics Bulletin, 1(6), 80-83.

Willison, J, W. Robinson, and G. Lackmann, 2013: The importance of resolving mesoscale latent heating in the North Atlantic stormtrack. Journal of the Atmospheric Sciences, 70, 2234-2250.

Woollings, T., 2010: Dynamical influences on European climate: An uncertain future. Philosophical Transactions of the Royal Society, 368A, 3733-3756.

Woollings, T., B. Hoskins, M. Blackburn, and P. Berrisford, 2008: A new Rossby wave-breaking interpretation of the North Atlantic Oscillation. Journal of the Atmospheric Sciences, 65, 609-626.

Woollings, T., J. M. Gregory, J. Pinto, M. Reyers, and D. Brayshaw, 2012: Response of the North Atlantic storm track to climate change shaped by ocean–atmosphere coupling. Nature Geoscience, 5, 313-317.

Xie, S.-P., 2004: Satellite observations of cool ocean–atmosphere interaction. Bulletin of the American Meteorological Society, 85, 195-208.

Xie, S.-P., J. Hafner, Y. Tanimoto, W. T. Liu, H. Tokinaga, and H. Xu, 2002: Bathymetric effect on the winter sea surface temperature and climate of the Yellow and East China Seas. Geophysical Research Letters, 29, 2228, doi:10.1029/2002GL015884.

Xu, H., M. Xu, S. P. Xie, and Y. Wang, 2011: Deep atmospheric response to the spring Kuroshio over the East China Sea. Journal of Climate, 24, 4959-4972.

Yin, J. H., 2005: A consistent poleward shift of the storm tracks in simulations of 21st century climate. Geophysical Research Letters, 32, L18701, doi:10.1029/2005GL023684.

Yu, L., X. Jin, and R. A. Weller, 2008: Multidecadel global flux datasets from the Objectively Analyzed Air-sea Fluxes (OAFlux) Project: Latent and sensible heat fluxes, ocean evaporation, and related surface meteorological variables. Woods Hole Oceanographic Institution, OAFlux Project Technical Report. OA-2008-01, 64 pp.

Zhang, Y., J. M. Wallace, and D. S. Battisti, 1997: ENSO-like interdecadal variability:1900-93. Journal of Climate, 10, 1004-1020.

Zorita, E., and C. Frankignoul, 1997: Modes of North Atlantic decadal variability in the ECHAM1/LSG coupled ocean–atmosphere general circulation model. Journal of Climate, 10, 183-200.